

論文 / 著書情報
Article / Book Information

題目(和文)	パルスレーザー堆積法による準安定構造を持つ鉄基酸化物薄膜の作製
Title(English)	Growth of iron-based oxide thin films with metastable structures by pulsed laser deposition
著者(和文)	濱寄容丞
Author(English)	Yosuke Hamasaki
出典(和文)	学位:博士(工学), 学位授与機関:東京工業大学, 報告番号:甲第10335号, 授与年月日:2016年9月20日, 学位の種別:課程博士, 審査員:伊藤 満,谷山 智康,平松 秀典,東 正樹,舟窪 浩
Citation(English)	Degree:., Conferring organization: Tokyo Institute of Technology, Report number:甲第10335号, Conferred date:2016/9/20, Degree Type:Course doctor, Examiner:,,,,,
学位種別(和文)	博士論文
Type(English)	Doctoral Thesis

DOCTORAL THESIS

Growth of iron-based oxide thin films with
metastable structures by pulsed laser deposition

Yosuke Hamasaki

Department of Materials Science and Engineering

Interdisciplinary Graduate School of Science and Engineering

Tokyo Institute of Technology

September, 2016

List of contents

1. Introduction	1
1.1 Preface	2
1.2 Preparation of metastable phase.....	3
1.3 Iron-based oxides	4
1.4 κ -Al ₂ O ₃ -type structure.....	4
1.4.1 Crystal structure	4
1.4.2 Magnetic Property	5
1.4.3 Ferroelectricity	6
1.5 Motivation and Objective.....	7
2. Phase Control in ScFeO ₃	15
2.1 Introduction	16
2.2 Experiment	17
2.3 Results and Discussion.....	18
2.3.1 Bixbyite-type ScFeO ₃	18
2.3.2 Spinel-type ScFeO ₃	19
2.3.3 YMnO ₃ -type ScFeO ₃	20
2.3.4 Corundum-type ScFeO ₃ on α -Fe ₂ O ₃ /Al ₂ O ₃ (001)	22
2.3.5 Corundum-type ScFeO ₃ on NdCaAlO ₄ (001)	24
2.3.6 κ -Al ₂ O ₃ -type ScFeO ₃	25
2.4 Discussion	25
2.5 Summary	27
3. Al ₂ O ₃ -Fe ₂ O ₃ system	49
3.1 Introduction	50
3.2 Experiment	50
3.3 Results and Discussion.....	51
3.3.1 Growth of AlFeO ₃ film.....	51
3.3.2 Stabilization of κ -Al ₂ O ₃ -type Al _x Fe _{2-x} O ₃ films	54
3.3.3 Investigation of Interface by TEM	56
3.3.4 Ferroelectric property by PFM.....	57
3.3.5 <i>P-E</i> hysteresis loop.....	59

3.4 Summary	60
4. Sc₂O₃-Fe₂O₃ system	83
4.1 Introduction	84
4.2 Experiment	84
4.3 Results and Discussion.....	85
4.3.1 Growth of Sc _x Fe _{2-x} O ₃ film.....	85
4.3.2 Investigation of Interface by TEM	87
4.3.3 Dielectric Property	88
4.3.4 <i>P-E</i> hysteresis loop.....	90
4.3.5 Magnetic property	91
4.4 Summary	92
5. In₂O₃-Fe₂O₃ system	111
5.1 Introduction	112
5.2 Experiment	112
5.3 Results and Discussion.....	113
5.3.1 Growth of In _x Fe _{2-x} O ₃ film.....	113
5.3.2 Dielectric and ferroelectric property	115
5.3.3 Magnetic property	115
5.4 Summary	116
6. Conclusions	125

Chapter 1

Introduction

1.1 Preface

Film technique have contributed in the development of novel functional electronic devices. Especially, epitaxial film growth can manipulate the strain state in thin film through selection of the appropriate substrates, which can engineer the physical properties. This includes enhanced ferroelectric and magnetic order in materials. Moreover, epitaxial film growth can obtained metastable phase to select the appropriate substrates. A lot of materials which can not be obtained by a conventional solid reaction were stabilized in film from. The film technique can be one of dominant tool for exploitation of new functional materials.

In the present study, we attempted to stabilize iron oxide materials, which is unstable in bulk, using a pulsed laser technique. Firstly, I attempted to stabilize five crystal structures at ScFeO_3 composition by selecting the appropriate substrates. Among five crystal structure, four crystal structure have not been reported by other processing. Secondly, I focused on $\kappa\text{-Al}_2\text{O}_3$ -type iron-based materials. The crystal structure and physical properties such as ferroelectricity in films of $\kappa\text{-Al}_2\text{O}_3$ -type iron-based materials were investigated.

1.2 Preparation of metastable structure

Metastable structures in complex oxides are usually available through the control of temperature, volume of the crystal structure and the crystal size. Each parameters can be controlled by kinds of processing. Temperature controls the successive phase transition of BaTiO_3 from cubic at high temperature to a rhombohedral structure through tetragonal and orthorhombic structures.[1] Furthermore, BaTiO_3 can be transformed from a perovskite-type structure to a hexagonal-type structure with a drastic rearrangement of atoms above 1460 °C. Meanwhile, MgSiO_3 transforms from an orthoenstatite structure through a clinoenstatite, $\beta\text{-Mg}_2\text{SiO}_4$ + stishovite, $\gamma\text{-Mg}_2\text{SiO}_4$ + stishovite, ilmenite and perovskite to eventually realize a post-perovskite structure by applying pressure.[2] This leads to a reduction in the cell volume and a change in the coordination number. A relative increase in the surface energy by reducing the size sometimes inverts the hierarchy of the appearance of relevant metastable phases.

Recently, it is reported that metastable structure is stabilized in film form.[3] The epitaxial film growth can obtain metastable phase to select the appropriate substrates. Epitaxial strain could be reduce the formation energy. For example, perovskite-type BiMnO_3 which is stable under high pressure and YMnO_3 -type LuFeO_3 which is stable in nanoparticles.[4], [5] These results imply that selection of substrates serve as controlling any parameters such as temperature and the crystal size. In this study, metastable structures were prepared by pulsed laser deposition (PLD) technique.

1.3 Iron-based oxides

Iron-based oxides have been investigated for magnetic applications.[6] Among iron-based oxides, compounds with polar structure are studied as the candidate for multiferroic materials; both magnetism and ferroelectricity coexist in a single phase simultaneously. Multiferroic materials realize the low power consuming random access memories.[7] Especially, because of excellent ferroelectricity ($T_C = 850\text{ }^\circ\text{C}$ and spontaneous polarization $P_s \sim 100\text{ }\mu\text{C}/\text{cm}^2$) and high magnetic transition temperature (antiferromagnetic; $T_N = 850\text{ }^\circ\text{C}$), perovskite BiFeO_3 have attracted attentions from researchers.[8] YMnO_3 -type and perovskite ReFeO_3 compounds with ferroelectricity and weakferromagnetism are also studied as multiferroic materials.[9] In $\text{A}^{3+}\text{FeO}_3$ compounds, these crystal structures appeared for rare earth A^{3+} cations. In the case of A^{3+} cations with small ionic radii, crystal structures of sesquioxide (A_2O_3) appear.[10] Among crystal structures of sesquioxide, $\kappa\text{-Al}_2\text{O}_3$ -type structure have polar structure and is expected as multiferroic materials.[11] However, study of ferroelectricity in this structure is not sufficient due to the contribution of the leakage currents.

1.4 $\kappa\text{-Al}_2\text{O}_3$ -type structure

1.4.1 Crystal structure

The $\kappa\text{-Al}_2\text{O}_3$ -type structure is one of the crystal structures of sesquioxide. The compounds with $\kappa\text{-Al}_2\text{O}_3$ -type structure are $\varepsilon\text{-Fe}_2\text{O}_3$ [12], $\kappa\text{-Al}_2\text{O}_3$ [13], $\varepsilon\text{-Ga}_2\text{O}_3$ [14] and AlFeO_3 [15]. $\kappa\text{-Al}_2\text{O}_3$ -type structure have the non-centrosymmetric space group of $Pna2_1$. The crystal structure is shown in Figure 1-1. The $\kappa\text{-Al}_2\text{O}_3$ -type structure have four cation sites; one regular tetrahedral site (Fe_A), two distorted octahedral sites (Fe_B and Fe_C) and one regular octahedral site (Fe_D). In this structure, there are two kind of

layer, which are tetrahedral site + distorted octahedral site and regular octahedral site + distorted octahedral site. The κ -Al₂O₃-type structure could be described as a combination of hexagonal close-packed (*ABAB...*) and cubic close-packed (*ABCABC...*) of oxygen ions: the sequence of the stacking along the *c*-axis is explained as *ABAC...ABAC*, where *A*, *B*, and *C* are close-packed oxygen layers.[16]

Among κ -Al₂O₃-type materials, only GaFeO₃ can be synthesized by a conventional solid-reaction technique.[17] κ -Al₂O₃-type AlFeO₃ is stable at high temperature, while corundum-type alumina and hematite coexist below 1300 °C.[15] ϵ -Fe₂O₃ can be synthesized as nanoparticles by combining the reverse micelle and the sol-gel techniques. The particle diameter plays important role in stabilizing ϵ -Fe₂O₃. [18] By using this combination technique, κ -Al₂O₃-type In_xFe_{2-x}O₃ and Rh_xFe_{2-x}O₃ can be synthesized.[19], [20]

1.4.2 Magnetic property

κ -Al₂O₃-type Fe₂O₃ show ferrimagnetism with Neel temperature (T_N) is 510K, which is attributed to the superexchange antiferromagnetic interaction among Fe cations via oxygens.[21] The direction of the magnetic moments at Fe_A and Fe_B sites are antiparallel to those at Fe_C and Fe_D. The magnetization at each sites are $M_A = 2.4\mu_B$, $M_B = 3.9\mu_B$, $M_C = 3.9\mu_B$ and $M_D = 3.7\mu_B$. The total magnetization value $(M_A + M_B - M_C - M_D)/4$ is $0.325\mu_B$ per Fe³⁺. Indeed, κ -Al₂O₃-type Fe₂O₃ have a huge coercivity (20 kOe at room temperature), which is largest among oxides. Because of the huge coercivity, κ -Al₂O₃-type Fe₂O₃ have been studied as the application for high-frequency electromagnetic wave absorbers. The origin of the huge coercivity in κ -Al₂O₃-type Fe₂O₃ is investigated by first principles calculation.[22] The strong Fe3d-O2p hybridization at Fe_C site induces nonzero orbital angular momentum, which causes a

large magnetic anisotropy through spin-orbital interaction. The large magnetic anisotropy induces the huge coercivity. It was also reported that the phase transition from ferrimagnetism to incommensurate magnetism at about 150K in κ -Al₂O₃-type Fe₂O₃. [23] This phase transition temperature is dependent on ionic radii of substituted cation. When Me^{3+} cations are substituted for Fe ions in ε -Fe₂O₃, the behavior of the phase transition is related to the size of ionic radius of Me^{3+} (r_{Me}). When $r_{Fe} < r_{Me}$ ($Me^{3+} = In$), Me^{3+} cations predominantly occupy the octahedral site, the phase transition temperature (T_p) value increases. When the ionic radius of $r_{Fe} > r_{Me}$ ($Me^{3+} = Ga$ and Al), Me^{3+} cations predominantly occupy the tetrahedral site and the T_p value decreases.

1.4.3 Ferroelectricity

Due to its polar structure, the κ -Al₂O₃-type structure is candidate for ferroelectric material. The calculation of the ferroelectricity in GaFeO₃ was performed by D. Stoeffler [24]. The calculated value of P_s is about 25 $\mu\text{C}/\text{cm}^2$, which is comparable with BaTiO₃ ($P_s = 26 \mu\text{C}/\text{cm}^2$). Stoeffler also predicted that polarization is switched through a centrosymmetric structure $Pnna$ i.e. $Pna2_1 \rightarrow Pnna \rightarrow Pna2_1$. The activation energy for polarization switching was reported to be 0.5 eV/f.u, which is quite larger than that for the conventional ferroelectric compound BaTiO₃ (20meV/f.u). Figure 1-2 shows the Stoeffler model for the polarization switching. The tetrahedral site become octahedral coordination into the $Pnna$ structure. Recently, A. Konishi *et.al.* performed the ab initio calculation for ε -Fe₂O₃ and κ -Al₂O. A. Konishi predicted the centrosymmetric structure with $Pbcn$ instead of $Pnna$ (Figure 1-3). The activation energies for polarization switching through $Pbcn$ are 0.08~0.15 eV/f.u.. This values are greatly smaller than that of the Stoeffler model. In the polarization switching through $Pbcn$, polarization switching is induced by the sharing of closed-packed oxygen layers. The detail of this

calculation is written at Appendix. The difference of two polarization switching mechanism is summarized in Figure 1-4. This mechanism of polarization switching largely differs from that of perovskite-type ferroelectricity. In the case of a typical ferroelectric BaTiO₃, Ti cations is displaced from a center of oxygen octahedron, which induces breaking its inversion symmetry. The movement of Ti cations by applying electric field causes polarization switching. The perovskite-type ferroelectric materials need to d⁰ cations (Ti⁴⁺, Nb⁵⁺, W⁶⁺, *etc*) or cations with lone pair (Bi³⁺, Pb²⁺, *etc*). The κ -Al₂O₃-type compounds don't include these specific cations and are composed of Fe³⁺ cations. Therefore, from the viewpoints of element strategy, κ -Al₂O₃-type compounds is interesting.

In bulk κ -Al₂O₃-type compounds, the obtained hysteresis loop showed leaky behavior due to insufficient insulation. Thin film form is suited to apply a large electric field and ferroelectricity of GaFeO₃ and ε -Fe₂O₃ epitaxial film is reported. Gich *et.al.* reported the ferroelectric hysteresis loop of ε -Fe₂O₃ epitaxial film measured by positive-up-negative-down (PUND) technique[25]. The ferroelectric hysteresis loop was also reported in GaFeO₃ films[26]. The observed values of polarization is 0.1-2 $\mu\text{C}/\text{cm}^2$, which is smaller than calculated value. Indeed, among GaFeO₃-type compounds, ferroelectricity of only GaFeO₃ and ε -Fe₂O₃ are reported.

1.5 Motivation and Objective

The objective of this study is the investigation of ferroelectricity in κ -Al₂O₃-type compounds and the exploitation of new functional materials using film technique. In this study, there are two topics;

1. Stabilization of several metastable structure by selection of the appropriate

substrates.

2. Growth and characterization of κ -Al₂O₃-type Me_x Fe_{2-x}O₃ film ($Me = Al, Sc$ and In)

The contents of the present thesis are set out as follows.

In chapter2, ScFeO₃ films with several crystal structure were stabilized on appropriate substrates. The crystal structure were characterized by XRD and HAADF-STEM measurements.

In chapter3, the κ -Al₂O₃-type Al_xFe_{2-x}O₃ film were prepared by PLD technique. The crystal structure and ferroelectricity were investigated.

In chapter4, the κ -Al₂O₃-type Sc_xFe_{2-x}O₃ film were prepared by PLD technique. The crystal structure and physical properties were investigated.

In chapter5, the κ -Al₂O₃-type In_xFe_{2-x}O₃ film were prepared by PLD technique. The crystal structure and physical properties were investigated.

In chapter6, summary of the present thesis and some concluding remarks are given.

Figures

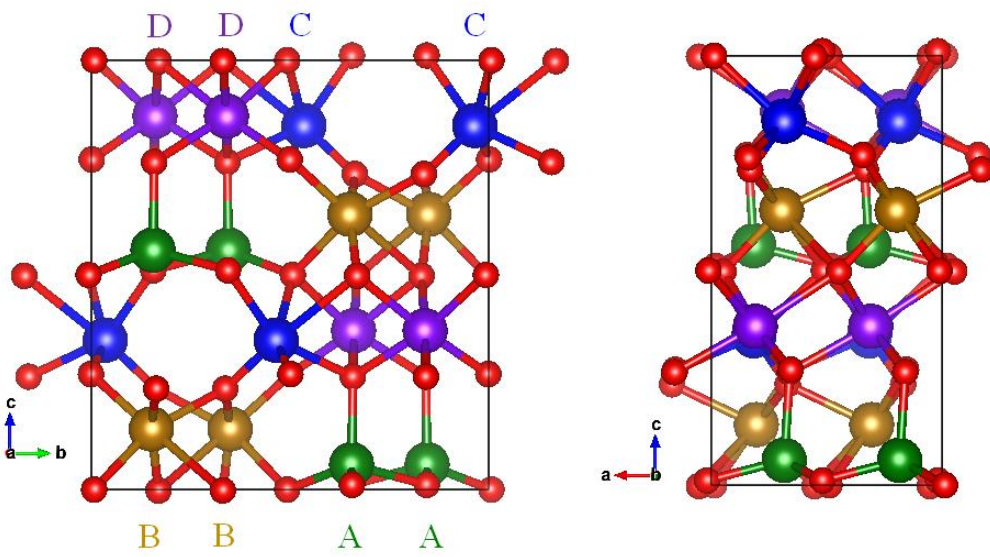


Figure 1-1 Crystal structure of κ -Al₂O₃-type structure.

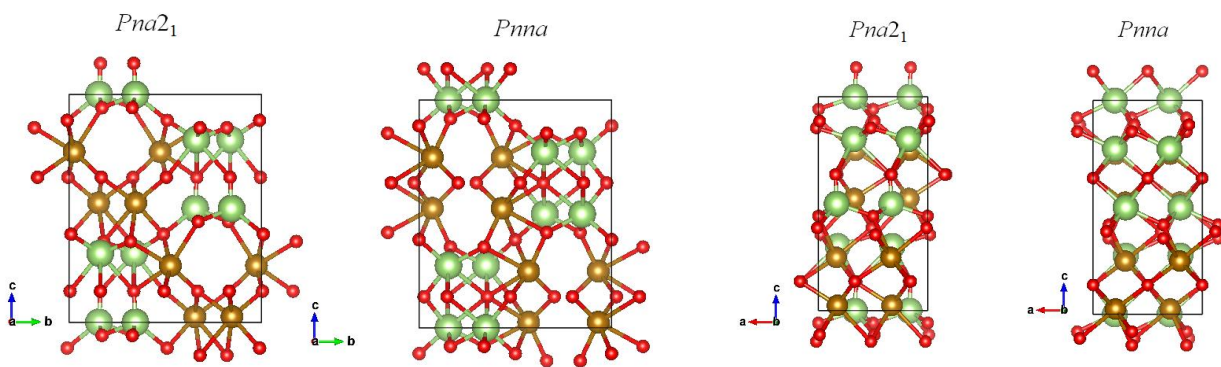


Figure 1-2 Crystal structure of centrosymmetric structure *Pnna*.

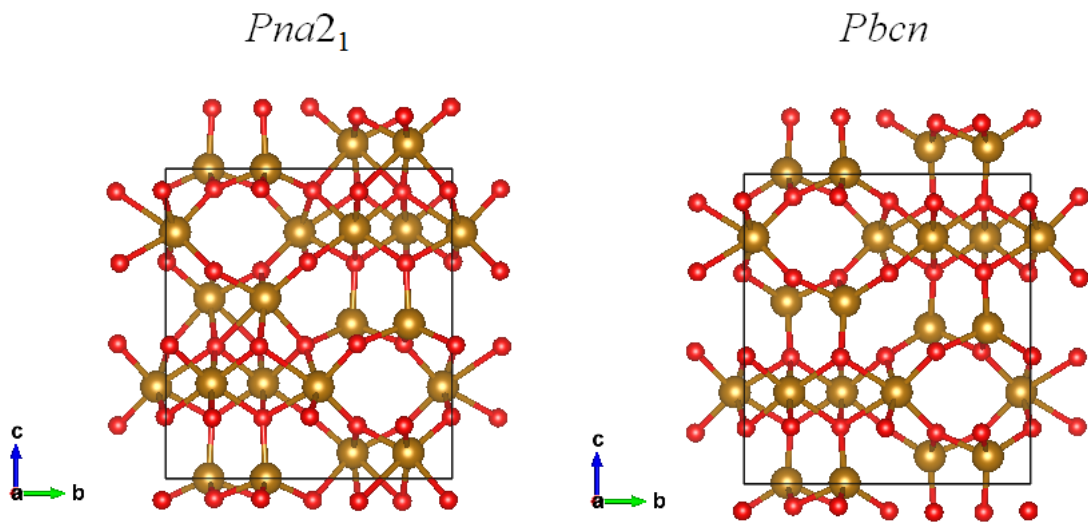


Figure 1-3 Crystal structure of centrosymmetric structure $Pbcn$.

Polarization switching

$$Ea = 0.5 \text{ eV/ f.u.}$$

	$Pna2_1 (+P)$	$Pnna$	$Pna2_1 (-P)$
A	4	6	6
B	6	6	6
C	6	6	6
D	6	6	4

$$Ea = 0.08\sim 0.15 \text{ eV/ f.u.}$$

	$Pna2_1 (+P)$	$Pbcn$	$Pna2_1 (-P)$
A	4	4	6
B	6	4	4
C	6	6	6
D	6	6	6

Figure 1-4 The difference of polarization switching. Number corresponds to coordination number.

References

- [1] H. H. Wieder, “Electrical behavior of barium titanate single crystals at low temperatures,” *Phys. Rev.*, vol. 99, pp. 1161–1165, 1955.
- [2] Y. O. Motohiko Murakami, Kei Hirose, Katsuyuki Kawamura, Nagayoshi Sata, “Post-Perovskite Phase Transition in MgSiO_3 ,” *Science*, vol. 304, pp. 855–858.
- [3] O. Y. Gorbenko, S. V. Samoilenkov, I. E. Graboy, and A. R. Kaul, “Epitaxial Stabilization of Oxides in Thin Films,” *Chem. Mater.*, vol. 14, pp. 4026–4043, 2002.
- [4] A. F. Moreira Dos Santos, A. K. Cheetham, W. Tian, X. Pan, Y. Jia, N. J. Murphy, J. Lettieri, and D. G. Schlom, “Epitaxial growth and properties of metastable BiMnO_3 thin films,” *Appl. Phys. Lett.*, vol. 84, p. 91, 2004.
- [5] W. Wang, J. Zhao, W. Wang, Z. Gai, N. Balke, M. Chi, H. N. Lee, W. Tian, L. Zhu, X. Cheng, D. J. Keavney, J. Yi, T. Z. Ward, P. C. Snijders, H. M. Christen, W. Wu, J. Shen, and X. Xu, “Room-Temperature Multiferroic Hexagonal LuFeO_3 Films,” *Phys. Rev. Lett.*, vol. 110, p. 237601, 2013.
- [6] L. MacHala, J. Tuček, and R. Zbořil, “Polymorphous transformations of nanometric iron(III) oxide: A review,” *Chem. Mater.*, vol. 23, pp. 3255–3272, 2011.
- [7] Y.H. Chu, L. W. Martin, M. B. Holcomb, M. Gajek, S.J. Han, Q. He, N. Balke, C.-H. Yang, D. Lee, W. Hu, Q. Zhan, P.-L. Yang, A. Fraile-Rodríguez, A. Scholl, S. X. Wang, and R. Ramesh, “Electric-field control of local ferromagnetism using a magnetoelectric multiferroic,” *Nat. Mater.*, vol. 7, pp. 478–482, 2008.
- [8] J.-G. Park, M. D. Le, J. Jeong, and S. Lee, “Structure and spin dynamics of

- multiferroic BiFeO₃,” *J. Phys. Condens. Matter*, vol. 26, p. 433202, 2014.
- [9] W. Prellier, M. P. Singh, and P. Murugavel, “The single-phase multiferroic oxides: from bulk to thin film,” *J. Phys. Condens. Matter*, vol. 17, pp. 7753–7753, 2005.
- [10] D. M. Giaquinta and H.C. zur Loye, “Structural Predictions in the ABO₃ Phase Diagram,” *Chem. Mater.*, vol. 6, pp. 365–372, 1994.
- [11] R. Saha, A. Sundaresan, and C. N. R. Rao, “Novel features of multiferroic and magnetoelectric ferrites and chromites exhibiting magnetically driven ferroelectricity,” *Mater. Horiz.*, vol. 1, pp. 20–31, 2014.
- [12] K. Kelm and W. Mader, “Synthesis and structural analysis of ϵ -Fe₂O₃,” *Zeitschrift fur Anorg. und Allg. Chemie*, vol. 631, pp. 2383–2389, 2005.
- [13] B. Ollivier, R. Retoux, P. Lacorre, D. Massiot, and G. Ferey, “Crystal structure of kappa-alumina: An X-ray powder diffraction, TEM and NMR study,” *J. Mater. Chem.*, vol. 7, pp. 1049–1056, 1997.
- [14] R. Roy, V. G. Hill, and E. F. Osborn, “Polymorphism of Ga₂O₃ and the System Ga₂O₃-H₂O,” *J. Amer. Chem. Soc.*, vol. 74, pp. 719–722, 1952.
- [15] R. R. Dayal, J. a. Gard, and F. P. Glasser, “Crystal data on FeAlO₃,” *Acta Crystallogr.*, vol. 18, pp. 574–575, 1965.
- [16] F. Bouree, J. L. Baudour, E. Elbadraoui, J. Musso, C. Laurent, and a. Rousset, “Crystal and magnetic structure of piezoelectric, ferrimagnetic and magnetoelectric aluminium iron oxide FeAlO₃ from neutron powder diffraction,” *Acta Crystallogr. Sect. B Struct. Sci.*, vol. 52, pp. 217–222, 1996.
- [17] H. J. Hook, “Thermal Stability of Gallium Orthoferrite in the System Fe₂O₃-FeO-Ga₂O₃,” *J. Am. Ceram. Soc.*, vol. 48, pp. 470–472, 1965.

- [18] S. Sakurai, A. Namai, K. Hashimoto, and S. Ohkoshi, "First observation of phase transformation of all four Fe₂O₃ phases (gamma --> epsilon --> beta --> alpha-phase).," *J. Am. Chem. Soc.*, vol. 131, pp. 18299–18303, 2009.
- [19] S. Sakurai, S. Kuroki, H. Tokoro, K. Hashimoto, and S. Ohkoshi, "Synthesis, Crystal Structure, and Magnetic Properties of ε-In_xFe_{2-x}O₃ Nanorod-Shaped Magnets," *Adv. Funct. Mater.*, vol. 17, pp. 2278–2282, 2007.
- [20] A. Namai, M. Yoshikiyo, S. Umeda, T. Yoshida, T. Miyazaki, M. Nakajima, K. Yamaguchi, T. Suemoto, and S. Ohkoshi, "The synthesis of rhodium substituted ε-iron oxide exhibiting super high frequency natural resonance," *J. Mater. Chem. C*, vol. 1, p. 5200, 2013.
- [21] J. Tuček, R. Zbořil, A. Namai, and S. Ohkoshi, "ε-Fe₂O₃: An Advanced Nanomaterial Exhibiting Giant Coercive Field, Millimeter-Wave Ferromagnetic Resonance, and Magnetoelectric Coupling," *Chem. Mater.*, vol. 22, pp. 6483–6505, 2010.
- [22] M. Yoshikiyo, K. Yamada, A. Namai, and S. Ohkoshi, "Study of the Electronic Structure and Magnetic Properties of ε-Fe₂O₃ by First-Principles Calculation and Molecular Orbital Calculations," *J. Phys. Chem. C*, vol. 116, pp. 8688–8691, 2012.
- [23] S. Sakurai, J. Jin, K. Hashimoto, and S. Ohkoshi, "Reorientation Phenomenon in a Magnetic Phase of ε-Fe₂O₃ Nanocrystal," *J. Phys. Soc. Japan*, vol. 74, pp. 1946–1949, 2005.
- [24] D. Stoeffler, "First principles study of the electric polarization and of its switching in the multiferroic GaFeO₃ system.," *J. Phys. Condens. Matter*, vol. 24, p.185502, 2012.

- [25] M. Gich, I. Fina, A. Morelli, F. Sánchez, M. Alexe, J. Gàzquez, J. Fontcuberta, and A. Roig, “Multiferroic Iron Oxide Thin Films at Room Temperature,” *Adv. Mater.*, vol. 26, pp. 4645–4652, 2014.
- [26] A. Thomasson, S. Cherifi, C. Lefevre, F. Roulland, B. Gautier, D. Albertini, C. Meny, and N. Viart, “Room temperature multiferroicity in $\text{Ga}_{0.6}\text{Fe}_{1.4}\text{O}_3\text{:Mg}$ thin films,” *J. Appl. Phys.*, vol. 113, p. 214101, 2013.

Chapter 2

Phase control in ScFeO₃

2.1 Introduction

Metastable structures in complex oxides are usually available through the control of temperature, volume of the crystal structure and the crystal size. In order to control each parameters, we needs to use different processing. Recently, film technique is used for stabilization of metastable structure. The epitaxial film growth can obtained metastable phase to select the appropriate substrates. Epitaxial strain could be reduce the formation energy. Therefore, selection of substrates might serve as controlling any parameters such as temperature and the crystal size. In this chapter, various metastable structures were prepared by pulsed laser deposition (PLD) technique.

It is well known that typical structure, which appears in the formula ABO_3 , is perovskite. It is well recognized in the inorganic chemistry field that the combination of A cation with relatively large ionic radius and B cation with smaller ionic radius tend to form a perovskite structure. In ABO_3 compounds, a tolerance factor, $t = (r_A + r_O) / \sqrt{2}(r_B + r_O)$, where r_A , r_B and r_O , respectively, are ionic radius of A, B cations and O anion, is a scale to grasp the yielded structures; $t = 1$ cubic perovskite, $t > 1$ hexagonal perovskite, $t < 1$ orthorhombic or rhombohedral perovskite[1]. In a case of smaller t value in $A^{3+}B^{3+}O_3$, sesquioxide structures appear, whereas ilmenite-type and $LiNbO_3$ -type structures form in $A^{2+}B^{4+}O_3$ and $A^{1+}B^{5+}O_3$ [2], [3]. In the $A^{3+}B^{3+}O_3$ compounds, there are structural cross point between ABO_3 and A_2O_3 structures in the region of small t . Therefore, we focused on iron oxides because simple iron oxides have four structure and many iron-based perovskite were reported. Considering the Hume-Rothery rule which is that if the relative difference between two atomic radii is more than 15%, it is difficult to form

the solid solution, we selected Sc as the counter element ($\text{Fe}^{3+}(\text{VI})$ 0.645 Å, $\text{Sc}^{3+}(\text{VI})$ 0.745 Å). Previously reported $\text{A}^{3+}\text{FeO}_3$ phases are summarized in Figure 2-1(a) using ionic radii of 6-coordinated A^{3+} ions as a parameter. We summarized the crystal structures for $\text{A}^{3+}_2\text{O}_3$ in Figure 2-1(b). From Figure 2-1 (a) and (b), we attempted to stabilize ScFeO_3 films with six structure; corundum, bixbyite, spinel, $\kappa\text{-Al}_2\text{O}_3$, YMnO_3 and LiNbO_3 -type structures (Figure 2-2).

2.2 Experiment

$\text{Sc}_x\text{Fe}_{2-x}\text{O}_3$ films were grown on $\text{SrTiO}_3(111)$ single-crystal substrates by PLD technique. A fourth-harmonic wave of a Nd: YAG laser ($\lambda= 266$ nm) was used. A repetition rate and a fluence of a Nd: YAG laser are 5Hz and 2.4, respectively. The target was prepared by mixing Sc_2O_3 and $\alpha\text{-Fe}_2\text{O}_3$ powder and sintering at 1450°C for 14 hours in air. Chemical composition of targets are ScFeO_3 . The crystal structure of films were investigated by high-resolution X-ray diffraction (XRD) using a Rigaku Smart-Lab diffractometer. X-ray was monochromatized using a Ge(220) 2-bounce crystal and Cu $K\alpha$ radiation ($\lambda=1.5406$ Å) was used. The Reciprocal space mapping (RSM) was measured to estimate to lattice constants. High temperature XRD (HTXRD) was measured using a Rigaku Smart-Lab diffractometer with an Anton Paar hot stage. The detail of $\text{Sc}_x\text{Fe}_{2-x}\text{O}_3$ films were characterized by HAADF-STEM. HAADF-STEM image was carried out on the JEOL ARM-200F operated at 200kV. Sample for TEM was prepared by a focused ion beam (FIB) method.

2.3 Result and Discussion

2.3.1. Bixbyite-type structure ScFeO_3

Bixbyite-type structure with space group (S.G.) $Ia-3$ is known as the C -type rare-earth sesquioxide structure. Bixbyite-type structure is described as a superstructure of fluorite-type structure with doubled lattice parameter. In order to stabilize bixbyite-type structure, ScFeO_3 film was deposited on YSZ(001) substrate at 800°C under $P_{\text{O}_2} = 100$ mTorr. The Laser fluence of 2.4 J cm^{-2} is used. XRD 2θ - θ pattern of ScFeO_3 film on YSZ(001) is shown in Figure 2-3. Four peaks were observed. These peaks corresponds to $002l$ reflections of bixbyite-type structure. Especially, two peaks at 18.46° and 57.54° indicate that ScFeO_3 film on YSZ has a doubled lattice parameter of YSZ with fluorite-type structure. In order to characterize crystal structure of thin films, 2D RSM for the ScFeO_3 film on YSZ(001) was recorded by PILATUS. Figure 2-4 shows the 2D RSM around $h02$ ($h=2n$) reflections. The reflections of the film, located near diffractions of substrates, is observed, which correspond to $l04$ ($h = 4n$) reflections. We also carried out 2D RSM around YSZ 111 reflection (Figure 2-5). 112 and 332 reflections of bixbyite-type ScFeO_3 were observed. Therefore, XRD results revealed that bixbyite-type ScFeO_3 was epitaxially grown on YSZ(001) substrate. In order to characterize the detail of ScFeO_3 film, the high-angle annular dark-field scanning transmission electron microscopy (HAADF-STEM) was performed. Figure 2-6 show the cross-sectional HAADF-STEM image. The flat surface of film is observed. HAADF-STEM image for ScFeO_3 film viewed along the YSZ[001] direction agrees with the atomic arrangement of bixbyite-type structure (Figure 2-7(a)). There are vertical lines of bright spots in Figure 2-4. Horizontal lines were also observed in bixbyite-type ScFeO_3 film (Figure 2-7(b)). These vertical and horizontal lines indicates the presence of the 90° domain structure and the

width of domains are about 100 nm. This 90° domain structures are reported in a epitaxial In₂O₃ film deposited on a YSZ(001) substrate[4]. This is caused by the loss of twofold rotation operations along [110] directions and fourfold rotation operation along [100] directions from fluorite structure.

2.3.2. Spinel-type structure ScFeO₃

Spinel structure is similar to NaCl-type structure and the lattice constant of spinel structure is twice as large as that of NaCl-type structure. In order to stabilize spinel-type structure, we selected MgAl₂O₄(001) substrate and MgO(001) substrate. Crystal structures of MgAl₂O₄ and MgO are spinel-type and NaCl-type structures, respectively. It is note that spinel-type sesquioxide is classified as defect-spinel structure. ScFeO₃ films were deposited at same condition of bixbyite-type ScFeO₃ film. Figure 2-8 shows XRD 2 θ - θ pattern of ScFeO₃ film on MgO(001). Two peaks correspond to 002 and 004 reflections of spinel-type structure. The 2D RSM for the ScFeO₃ film on MgO was performed along MgO[110] direction (Figure 2-9). In Figure 2-9, *hhl* (*l* and *h* = 2*n*, 2*m* or 2*n*+1, 2*m*+1) corresponding to super lattice peaks were observed and consequently crystal structure of ScFeO₃ film is spinel-type. The lattice constant of spinel-type ScFeO₃ film calculated from out of plane pattern is 8.64 Å. In order to estimate to in-plane lattice constant, we also measured the RSM around MgO 024 diffraction. The RSM around MgO 024 diffraction indicates that the in-plane lattice constant of ScFeO₃ film was same as that of the MgO substrate (*a* = 4.21 Å) and the spinel-type ScFeO₃ film has a tetragonal lattice. We also characterized spinel-type ScFeO₃ film by HAADF-STEM measurements. Figure 2-10 shows the cross-sectional HAADF-STEM image along MgO[110] direction. As can be seen in Figure 2-11, the atomic arrangement of ScFeO₃ film on MgO substrate clearly

matches with that of spinel-type structure, where red spheres are cation in the 4-fold symmetry site and blue spheres cation in 6-fold symmetry site. From these results, we confirmed that the defect-spinel-type ScFeO_3 film was epitaxially grown on MgO substrate. We also deposited ScFeO_3 film on MgAl_2O_4 (001) substrate, however spinel-type structure did not appear. Lattice mismatch was estimated using lattice constants of $\gamma\text{-Fe}_2\text{O}_3$ ($a = 8.351 \text{ \AA}$)[5]. Lattice mismatch between $\gamma\text{-Fe}_2\text{O}_3$ and substrate are 3.89% for MgAl_2O_4 and -1.19% for MgO , respectively. Here, since the ionic radius of Sc^{+3} is larger than that of Fe^{3+} , lattice constant of defect-spinel-type ScFeO_3 could be large than that of $\gamma\text{-Fe}_2\text{O}_3$. Thus, lattice mismatch between defect-spinel-type ScFeO_3 and substrate could be larger than that between $\gamma\text{-Fe}_2\text{O}_3$ and substrates. Due to a larger lattice mismatch, it is estimated that defect spinel-type ScFeO_3 was not stabilized on MgAl_2O_4 substrates.

2.3.3. YMnO_3 -type structure ScFeO_3

In the previous reports, YMnO_3 -type structure such as ReFeO_3 and ReMnO_3 was stabilized on $\text{YSZ}(111)$ and $\text{Al}_2\text{O}_3(0001)$ substrates[6]–[8]. We attempted to deposit ScFeO_3 film on $\text{YSZ}(111)$ and $\text{Al}_2\text{O}_3(0001)$ substrates. The growth condition of ScFeO_3 film is the same as that of bixbyite-type ScFeO_3 film. The ScFeO_3 film on $\text{YSZ}(111)$ substrate have bixbyite and YMnO_3 -type phase, while the ScFeO_3 film on Al_2O_3 substrate have single phase of YMnO_3 -type structure. Figure 2-12 shows XRD 2θ - θ pattern of ScFeO_3 film on $\text{Al}_2\text{O}_3(001)$. To investigate the in-plane relationship, Phi-scan was measured around $\text{ScFeO}_3\{30\bar{1}2\}$ and $\text{Al}_2\text{O}_3\{204\}$ reflections. Phi-scan measurement reveals that the in-plane epitaxial relationship is YMnO_3 -type $\text{ScFeO}_3[100]//\text{Al}_2\text{O}_3[100]$. Figure 2-13 shows 2D RSM around $11\bar{3}l$ diffractions of Al_2O_3 . $11\bar{1}$ and $22\bar{1}$ diffractions of YMnO_3 -type structure were observed. The lattice constants of YMnO_3 -type ScFeO_3 film

are $a = 5.72 \text{ \AA}$ and $c = 11.71 \text{ \AA}$. Masuno *et al.* reported YMnO₃-type Lu_{1-x}Sc_xFeO₃ ($0 \leq x \leq 0.8$) prepared by containerless processing[9]. Both a and c lattice constants decrease with increasing Sc contents. It is note that lattice constant a largely changed and lattice constant a show small change in YMnO₃-type $ReFeO_3$ and $ReMnO_3$. The ratio of the change in lattice constant from LuFeO₃ powder to ScFeO₃ film is -4.5% for a -axis and -0.34% for c -axis, respectively. This result constituents with that of YMnO₃-type $ReFeO_3$ and $ReMnO_3$.

$ReFeO_3$ ($Re = \text{Tb-Lu, Y}$) has a polar structure with S.G. $P6_3cm$ [6], [10], whereas $InFeO_3$ has a nonpolar structure with a S.G. $P6_3/mmc$ [11], i.e. nonpolar hexagonal $ReFeO_3$ is considered to be stabilized for a small ionic radius of rare earth ions. Because of the tilting of the FeO₅ bipyramids and the displacement of Re ions, unite cell volume of the polar phase becomes triple compared to that of nonpolar phase, i.e. $\sqrt{3}a_{P6_3/mmc} \times \sqrt{3}b_{P6_3/mmc}$ [12]. In order to distinguish polar or nonpolar structure, we carried out 2θ - ω scan around 104 and 208 reflections of film. 104 and 208 reflections are observed in $P6_3cm$ phase, while these are not observed in $P6_3/mmc$ phase. The angle of two peaks which are estimated from the $301\bar{2}$ diffraction are 35.60° and 75.38° . Figure 2-14 shows the average of ten times 2θ - θ scan around 104 and 208 reflections. We observed 104 and 208 reflections and confirmed YMnO₃-type ScFeO₃ film. Recently, antiferroelectric phase with S.G. $P-3c$ as a ground state is reported for $InMnO_3$ [13]. It is difficult to distinguish these two phases by XRD, because $P-3$ and $P6_3cm$ phase show the same extinct rule. Therefore, we performed HAADF-STEM along Al₂O₃[110]. The cross-sectional HAADF-STEM image is shown in Figure 2-15. The flat surface of film is observed. Figure2-16 shows atomic-resolution HAADF-STEM image of ScFeO₃ film. Since the intensity is proportional to Z^2 , bright spots correspond to Fe ions and dark spots

correspond to Sc ions. Fe and Sc ions occupy inside bipyramids and *Re* site, respectively. The observed atomic pattern of Sc ions are up-up-down and down-down-up. In the case of polar structure with $P6_3cm$, the atomic displacement pattern of *Re* ions are up-up-down or down-down-up, whereas in the case of nonpolar structure with $P6_3/mmc$ and $P-3c$ they are center-center-center and up-center-down, respectively (Figure2-17)[14], [15]. In terms of arrangements of *Re* ions, it is confirmed that ScFeO₃ film on Al₂O₃(001) is polar structure with $P6_3cm$. In atomic-resolution HAADF-STEM image, the 180° domain boundary is also observed (Figure 2-18). The yellow region corresponds to domain boundary. The atoms pattern in domain boundary is down-center-up, indicating nonpolar. This structure is reported in *RE*FeO₃ film (*Re* = Lu, Er) on YSZ(111) and MgO(111) substrates[14].

2.3.4. Corundum-type structure ScFeO₃ on α -Fe₂O₃/Al₂O₃(001)

Metastable corundum-type Ga₂O₃ and In₂O₃ film are epitaxially grown on a sapphire substrate (α -Al₂O₃)[16], [17]. However, as explained in the previous session, the crystal structure of ScFeO₃ films on α -Al₂O₃(001) substrate is not corundum-type but a YMnO₃-type phase. We selected an α -Fe₂O₃ film on α -Al₂O₃ substrate to stabilize corundum structure due to following reasons. The lattice mismatch between α -Fe₂O₃ ($a = 5.036 \text{ \AA}$ and $c = 13.749 \text{ \AA}$) and α -Al₂O₃ ($a = 4.77 \text{ \AA}$ and $c = 13.04 \text{ \AA}$) substrates is 5.58%, therefore the lattice mismatch between corundum-type ScFeO₃ and α -Al₂O₃ substrate is larger than 5.58%. This large mismatch may be the origin of YMnO₃-type phase stabilization instead of corundum-type ScFeO₃ on the Al₂O₃(001) substrate. In order to decrease the lattice mismatch, we chose using buffer layer with the corundum structure. Consequently, ScFeO₃ film was grown on epitaxially deposited α -Fe₂O₃ buffer layer over α -Al₂O₃(001)

substrates. α -Fe₂O₃ and ScFeO₃ films were deposited at the same condition of bixbyite ScFeO₃ film. Figure 2-19 shows the cross-sectional HAADF STEM. It is clear that the film has a multi-layer of ScFeO₃/Fe₂O₃/Al₂O₃. Figure 2-20 show XRD 2θ - θ pattern of ScFeO₃ film on the Fe₂O₃/Al₂O₃(001). 2D RSM around $10\bar{1}0$, 208 and 306 diffractions of Al₂O₃ is shown in Figure 2-21. ScFeO₃ film shows the same diffraction pattern as α -Fe₂O₃ film and Al₂O₃ substrate, indicating that corundum-type ScFeO₃ film was epitaxially grown on the Fe₂O₃/Al₂O₃ substrate. Lattice constants of corundum-type ScFeO₃ are found to be $a = 5.151 \text{ \AA}$ and $c = 13.991 \text{ \AA}$. Lattice mismatches between corundum-type ScFeO₃ and Al₂O₃ substrate or α -Fe₂O₃ are 7.99% and 2.28%, respectively. The small mismatch of the latter might have stabilized corundum-type ScFeO₃. It is generally known that there are two structures of ilmenite-type and LiNbO₃-type, relevant to the corundum structure. These structures are distinguished by the ordering manner of the cations. In the case of corundum-type structure, the stacking sequence of two cations, A and B, along c-axis is (A, B)-(A, B)-□-(A, B)-(A, B), where (A, B) indicate disordered A and B, and □ indicates vacancy. The stacking sequences along c-axis of ilmenite-type and LiNbO₃-type structures are A-B-□-B-A and A-B-□-A-B, respectively. In the XRD pattern, ilmenite-type structure should show 003 and 009 reflections, whereas these diffraction are forbidden in corundum-type and LiNbO₃-type structures. However, it is difficult to distinguish between corundum and LiNbO₃-type structures by XRD. Thus, the arrangement of cations was investigated by HAADF-STEM. In the atomic-resolution HAADF-STEM image along Al₂O₃<100>, bright spots correspond to two cation sites and two spots show an equal intensity (Figure 2-22). In the case of LiNbO₃-type structure, one should be a bright spot and the other dark spot. We also performed TEM- EDX analysis for two spots. The ratios of Sc and Fe at two spots

are 43:57, indicating that Sc and Fe atoms are disordered at two cation sites. Therefore, we concluded that the crystal structure of ScFeO₃ film deposited on α -Fe₂O₃/Al₂O₃ substrate is corundum-type.

2.3.5. Corundum-type structure ScFeO₃ on NdCaAlO₄(001)

In terms of rotation (Φ) of BO₆ octahedra along the perovskite [111] direction, LiNbO₃-type structure can be described as a distorted perovskite with tilting system of $a^-a^-a^-$ [18]. Perovskite with $\Phi = 0^\circ$ and $0 < \Phi < 15^\circ$ are regarded as cubic and rhombohedral structures, respectively. In the case of $\Phi > 20^\circ$, the crystal structure is LiNbO₃-type[19]. Note that LiNbO₃(012) correspond to pseud-cubic perovskite (001). LiNbO₃ and LiTaO₃ were epitaxially grown on perovskite type substrates with the relationship of LiTaO₃ and LiNbO₃(012)//SrTiO₃(001)[20]. In order to stabilize LiNbO₃-type structure, we deposited ScFeO₃ film on SrTiO₃(001), LaSrAlO₄(001) and NdCaAlO₄(001) substrates. LaSrAlO₄(001) and NdCaAlO₄(001) substrate have K₂NiF₄-type structure with lattice constants of $a = 3.756 \text{ \AA}$ and $a = 3.685 \text{ \AA}$, respectively. ScFeO₃ films were deposited at 800°C under 100mTorr. The laser fluence of 2.4 J cm⁻² was used. Among three perovskite-related substrates, single phased ScFeO₃ film was obtained on NdCaAlO₄ substrate (Figure 2-23). ScFeO₃ films were deposited at the same condition of bixbyite ScFeO₃ film. Figure 2-24 show XRD 2θ - θ pattern of ScFeO₃ film on the NdCaAlO₄(001). Four peaks were observed. It seems that this diffraction pattern corresponds to 00 l diffractions of perovskite structure. In order to investigate the crystal structure of the ScFeO₃ film, 2D RSM along NdCaAlO₄[100] was performed. ScFeO₃ film showed the diffraction pattern like perovskite structure, where red circles indicated peaks of ScFeO₃ film (Figure 2-25). Around 103 diffraction of NdCaAlO₄, two split

peaks of ScFeO₃ film were observed. This split is observed in rhombohedral perovskite film because rhombohedral perovskite film on NdCaAlO₄ (001) have four in-plane domains. There are two expected domain patterns; pseudo-cubic perovskite (001) parallel to in-plane or out-of plane of substrate (Figure 2-26)[21]. ScFeO₃ film on NdCaAlO₄ corresponded to the former. As described the section of corundum-type structure on α -Fe₂O₃/Al₂O₃(001), it is difficult to distinguish between LiNbO₃ and corundum-type structures by XRD. Therefore, the atomic arrangement of ScFeO₃ film was checked by HAADF-STEM. HAADF-STEM along NdCaAlO₄[100] showed the perovskite-like pattern and the intensity of all atoms were same (Figure 2-28). We also carried out TEM- EDX analysis for four spots of ScFeO₃ film. The ratio of Sc and Fe at two spots are almost 50:50, indicating Sc and Fe are disordered at any cation sites. From this result, corundum-type ScFeO₃ is considered to be epitaxially grown on NdCaAlO₄ substrate.

2.3.6. κ -Al₂O₃-type structure ScFeO₃

κ -Al₂O₃-type structure ScFeO₃ film was discussed at chapter 4.

2.4 Dissuasion

Table 2-1 summarizes the deposited films on various substrates, including the main phase, orientation of the crystal structure in the films and substrates, in-plane symmetry of the films and substrates, and secondary phase. Among these results, the κ -Al₂O₃-type phase is only obtained for the film deposited on the SrTiO₃(111) substrate. Although the target composition is Fe : Sc = 50 : 50, the chemical composition of the κ -Al₂O₃ film is Fe : Sc = 76 : 24.

Trial and error to realize the single-phase κ -Al₂O₃-type film revealed that the optimum conditions occur when an energy less than the target ablation (less than 0.32 Jcm⁻²) is used for film deposition. Usually, such a change in the ablation energy alters the composition of the ablated species. Therefore, the smaller ablation energy may have tuned the film composition to Fe : Sc = 76 : 24 when forming the κ -Al₂O₃-type structure, which may have a smaller formation energy than the same structure with a film composition of Fe : Sc = 50 : 50 on SrTiO₃(111). The assumption is supported by the fact that the deposition of the film using Sc-rich Sc_{1.5}Fe_{0.5}O₃ target gives bixbyite-type ScFeO₃ thin film without a trace of a κ -Al₂O₃-type ScFeO₃ film.

A necessary condition to achieve spinel- and corundum-types of ScFeO₃ is the small lattice mismatch between ScFeO₃ and the substrate. This idea is based on the fact that the corundum and spinel phases appear in mismatches of 2.28% between corundum-type ScFeO₃ and α -Fe₂O₃ on Al₂O₃(0001) and 0.83% between spinel-type ScFeO₃ and MgO(001), respectively, while the bixbyite-type phase appears on YSZ(111) (6.60% mismatch). The appearance of corundum-type ScFeO₃ on NdCaAlO₄(001) is attributed to the lattice mismatch of 2.31%, which is calculated using the pseudocubic lattice constant of 3.77 Å for the corundum-type ScFeO₃ and NdCaAlO₄(100). The appearance of LiNbO₃-type ScFeO₃ has been reported in the decompression of perovskite-type ScFeO₃ stabilized at a static pressure of 15 GPa, which is a reasonable result from the structural viewpoint that Sc and Fe are ordered in both structures.

The cation-ordered perovskite-type ScFeO₃ cannot be stabilized by the thin film technique. Changing from the cation-disordered corundum-type ScFeO₃ structure to the cation-ordered LiNbO₃ or the perovskite structure may be difficult by the thin film technique utilizing two-dimensional interfacial strain. From these points, we expect that

LiNbO₃-type ScFeO₃ may be grown by applying three-dimensional isostatic strain to the film or by applying a chemical pressure using ions with similar valences but different ionic radii (e.g., a combination of lanthanide family and iron or applying chemical pressure using ions with +2/+4 or +1/+5 valencies and different radii).

In the case of substrates with a large mismatch for spinel- and corundum-type ScFeO₃, either bixbyite- or YMnO₃-type phase or both are grown. These results indicate that formation energies of bixbyite- and YMnO₃-type phases are smaller than the other phases in the strained thin film state. Considering that YMnO₃-type ScFeO₃ has yet to be obtained in bulk form, the hierarchy of the energies of the relevant phases in the strained film form differs from that in a bulk state at ambient or high pressure.

Finally, the in-plane symmetries of the deposited films and the substrates were considered. κ -Al₂O₃-type Sc_{0.48}Fe_{1.52}O₃ on SrTiO₃(111), YMnO₃-type ScFeO₃ on SrTiO₃(001), and MgAl₂O₄(001) show different in-plane symmetries in the deposited films and the substrates. The formation of three in-plane domains rotated 120° from each other is already explained in the previous section for κ -Al₂O₃-type Sc_{0.48}Fe_{1.52}O₃ on SrTiO₃(111). The formation of hexagonal YMnO₃-type ScFeO₃ films on cubic SrTiO₃(001) and MgAl₂O₄(001) substrates may be ascribed to the effect of the interfacial layer such as amorphous phase, which has been reported in the YMnO₃ and YbFeO₃ films deposited on YSZ(111) and Si(001) substrates, respectively.

2.5 Summary

Using the ScFeO₃ target, we stabilized five crystal structures in the film form by selecting the appropriate substrates or using a buffer layer: κ -Al₂O₃-, spinel-, corundum-, YMnO₃-, and bixbyite-type structures. XRD and HAADF-STEM were used to identify

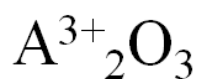
the phases. The lattice mismatch likely plays an important role in the phase stabilization of spinel- and corundum-type ScFeO_3 films. Additionally, the chemical atomic arrangement between the film and the substrate plays a vital role in all structures. The bottom layer is only formed in the $\kappa\text{-Al}_2\text{O}_3$ -type structure. Four of structures were obtained for the first time: $\kappa\text{-Al}_2\text{O}_3$ -, spinel-, corundum-, and YMnO_3 -type ScFeO_3 .

From the results of the present study, we can infer that targeted structures can be obtained by carefully selecting the substrate, crystal structure, and preparation conditions of the film (e.g., the oxygen partial pressure, temperature, and laser fluence), even if a structure has not been achieved by conventional methods. Moreover, this study suggests that the epitaxial thin film fabrication technique may be a powerful tool to explore new functional materials. The selection of the appropriate combination of materials, substrates, and preparation conditions may overcome the small potential barrier to the adjacent metastable phase or bypass the hierarchy of Gibbs energy to reach other metastable phases.

Figures



	Al	Ga	Fe	Sc	In	Lu
Ionic radius	0.535	0.620	0.645	0.745	0.800	0.861
GaFeO ₃ -type	M	S	M			
LiNbO ₃ -type				M		
YMnO ₃ -type					M	M
Perovskite						S



	Al	Ga	Fe	Sc	In	Lu
Ionic radius	0.535	0.620	0.645	0.745	0.800	0.861
Corundum-type	S	M	S		M	
Spinel-type	M	M	M			
GaFeO ₃ -type	M	M	M			
Bixbyite-type			M	S	S	S
β -Ga ₂ O ₃ -type		S				

Figure 2-1 (a) Phase relationship for (a) $A^{3+}FeO_3$ and (b) $A^{3+}_2O_3$. M means metastable phase.

S means stable phase.

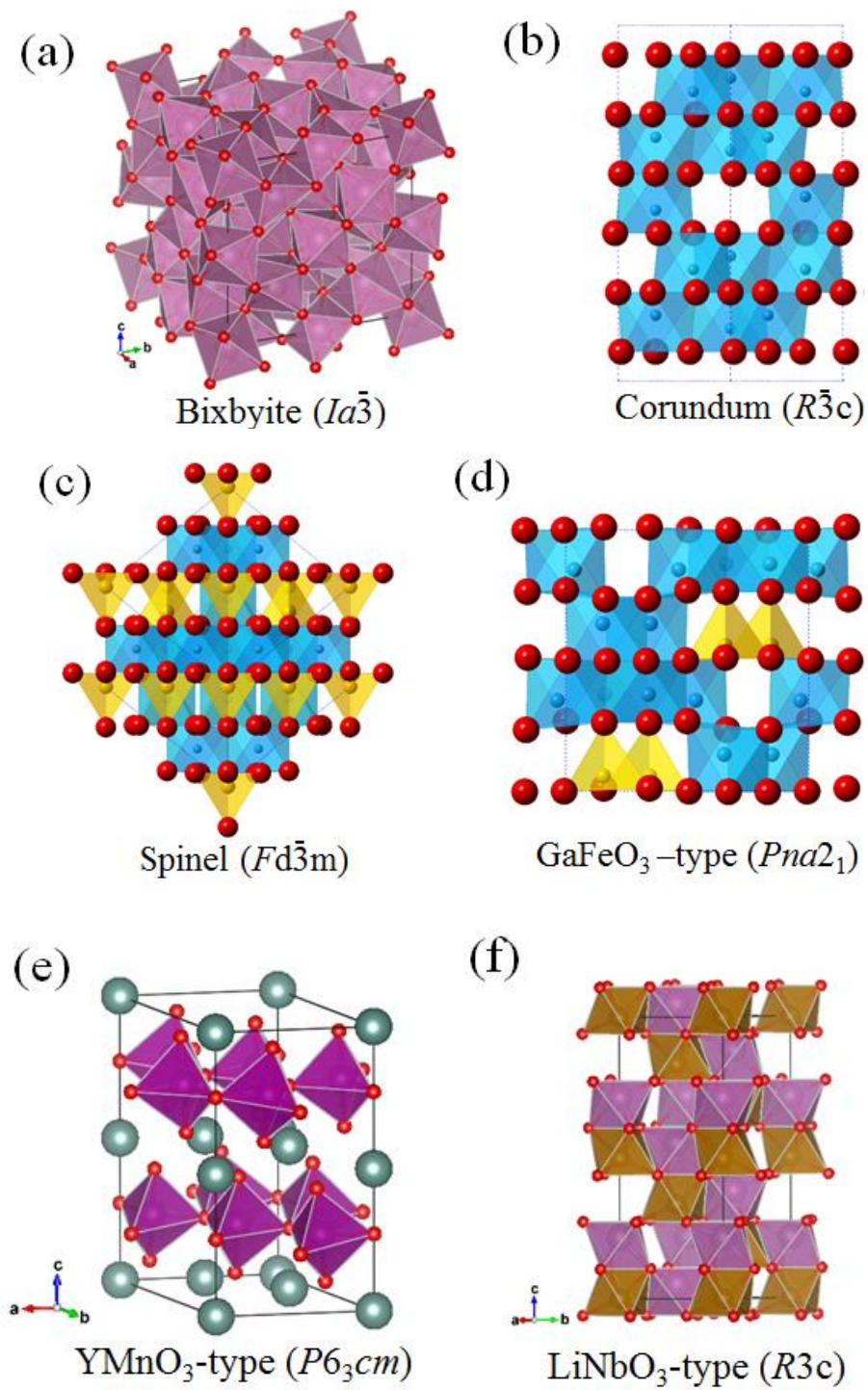


Figure 2-2 Schematic illustration of crystal structures. (a) Bixbyite ($Ia\bar{3}$), (b) Corundum ($R\bar{3}c$), (c) Spinel ($Fd\bar{3}m$), (d) κ -Al₂O₃-type ($Pna2_1$), (e) YMnO₃-type ($P6_3cm$) and (f) LiNbO₃-type ($R3c$)

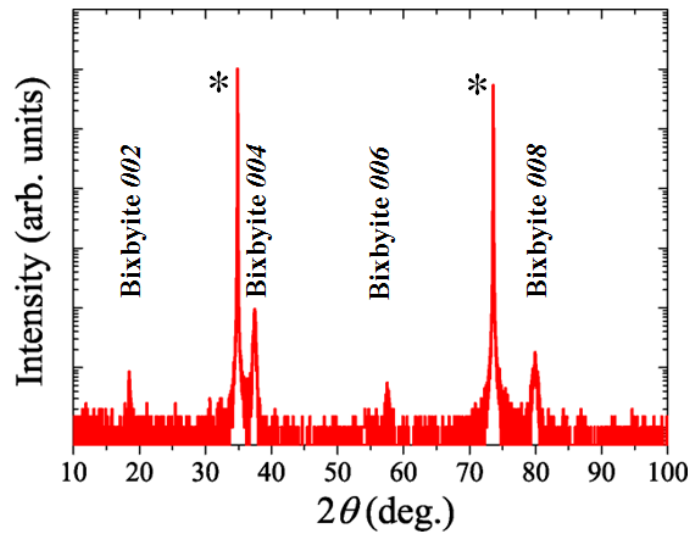


Figure 2-3 XRD θ - 2θ pattern of ScFeO_3 film on $\text{YSZ}(001)$ with 2θ angle of 10-100°. * correspond to the peaks of substrates.

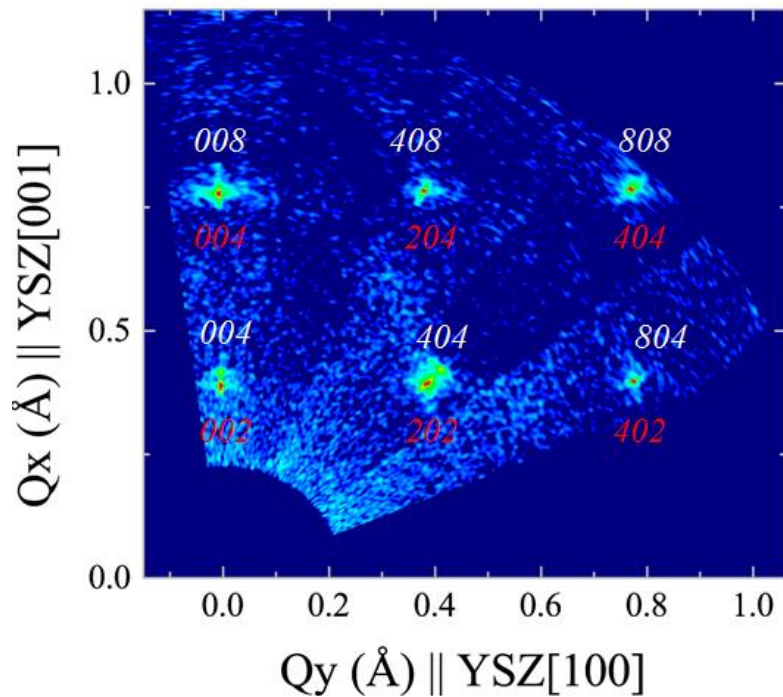


Figure 2-4 2D RSM of ScFeO_3 film on $\text{YSZ}(001)$ along $\text{YSZ}[100]$. Red and white indexes indicate YSZ substrate and ScFeO_3 film, respectively.

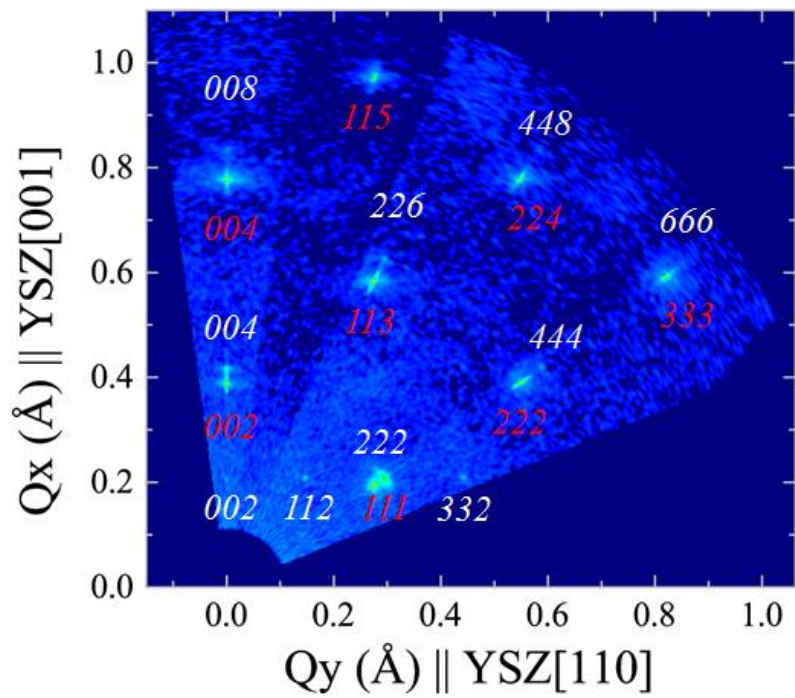


Figure 2-5 2D RSM of ScFeO₃ film on YSZ(001) along YSZ[100]. Red and white indexes indicate YSZ substrate and ScFeO₃ film, respectively.

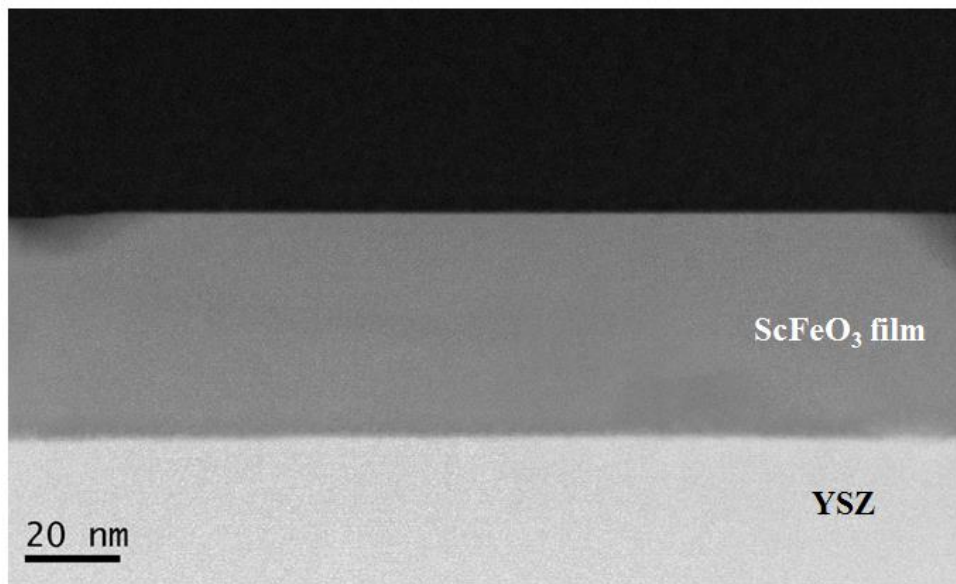


Figure 2-6 Cross sectional HAADF-STEM image of ScFeO₃ film on YSZ(001).

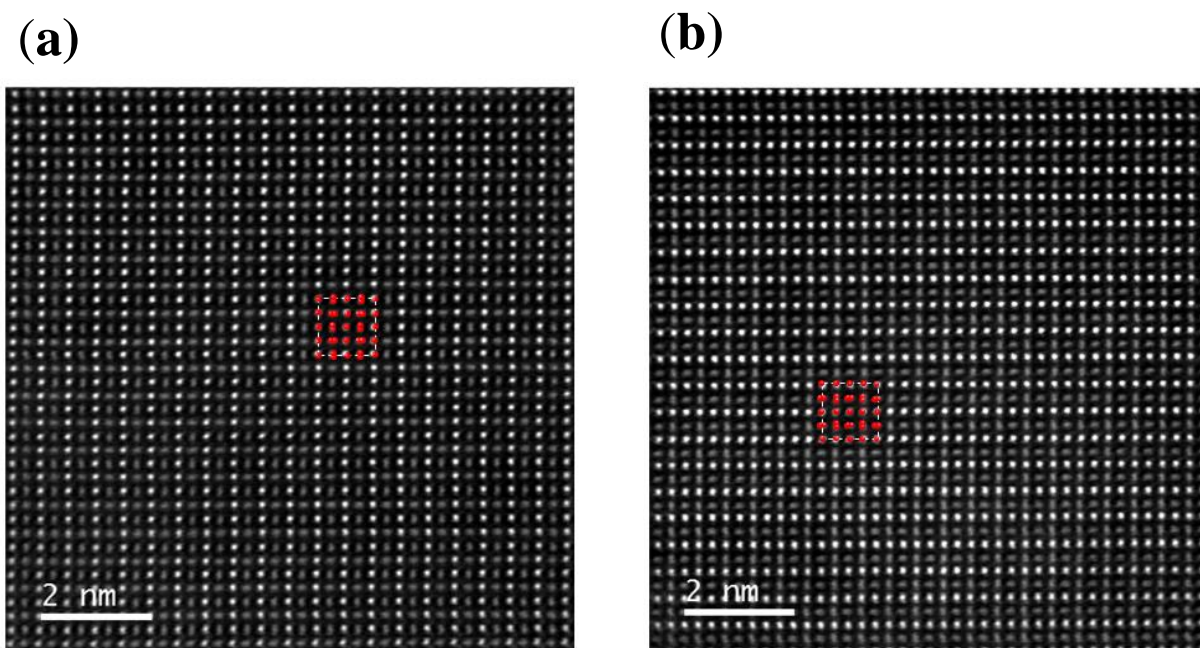


Figure 2-7 HAADF-STEM image of ScFeO_3 film on $\text{YSZ}(001)$. The direction of view is $\text{YSZ}[100]$. Simulated cationic positions and the unit cell are indicated by circles and broken lines, respectively.

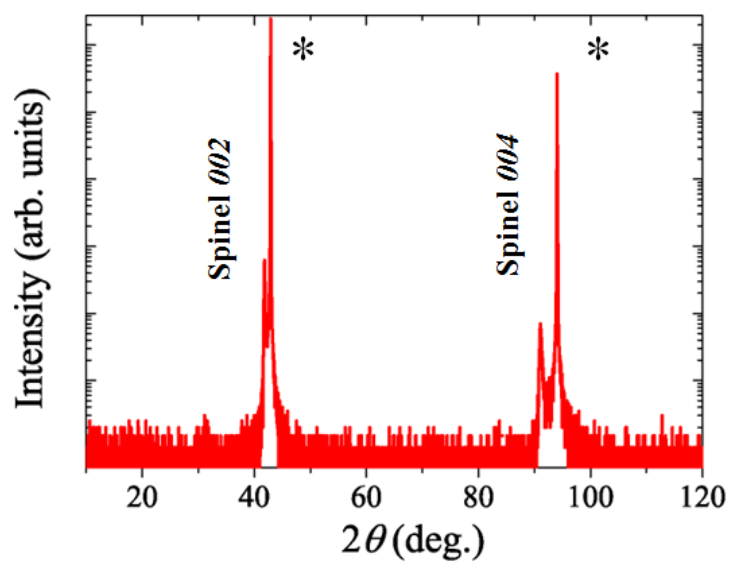


Figure 2-8 XRD θ - 2θ pattern of ScFeO_3 film on $\text{MgO}(001)$ with 2θ angle of 10 - 100° . * correspond to the peaks of substrates.

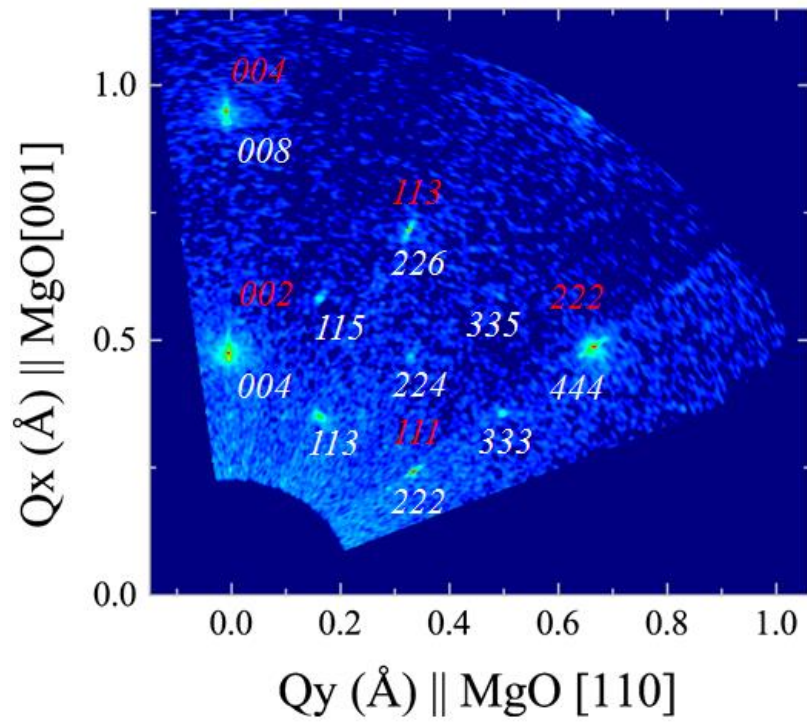


Figure 2-9 2D RSM of ScFeO₃ film on MgO(001) along MgO[110]. Red and white indexes indicate MgO substrate and ScFeO₃ film, respectively.

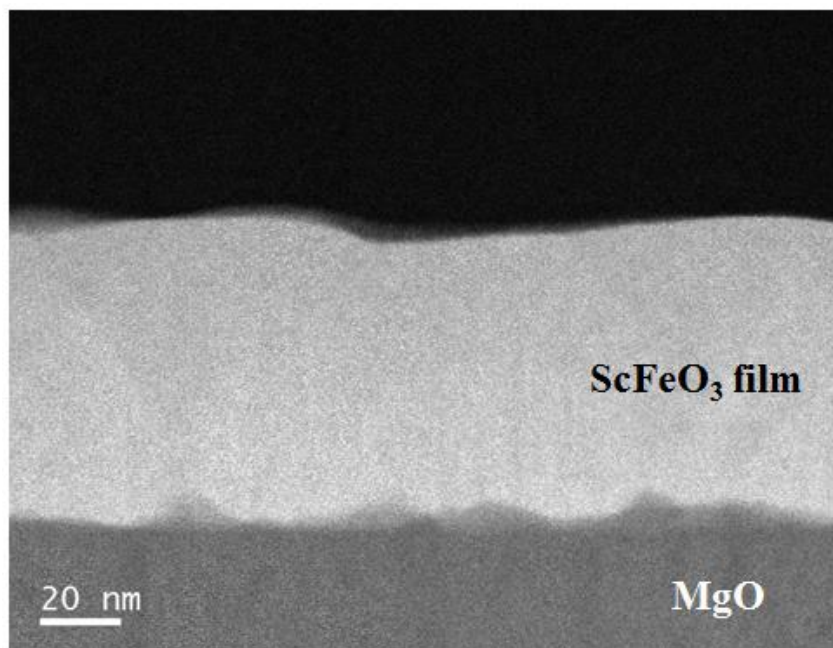


Figure 2-10 Cross sectional HAADF-STEM image of ScFeO₃ film on MgO(001).

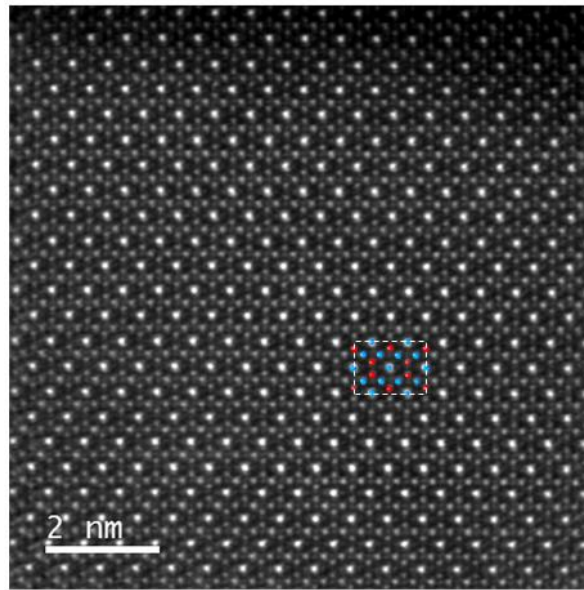


Figure 2-11 HAADF-STEM image of ScFeO₃ film on MgO(001). The direction of view is MgO[100]. Simulated cationic positions and the unit cell are indicated by circles and broken lines, respectively.

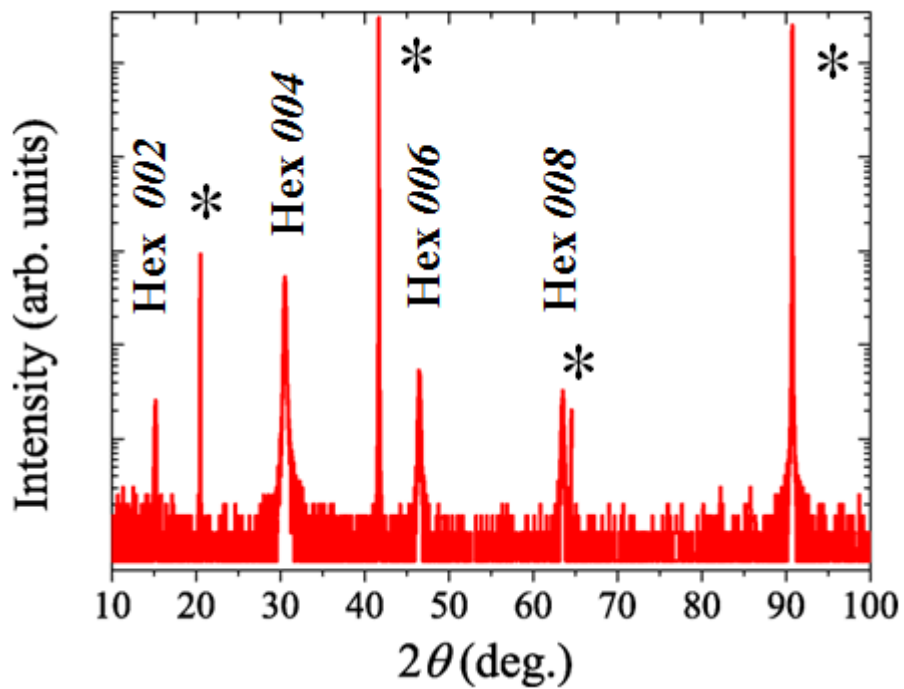


Figure 2-12 XRD θ - 2θ pattern of ScFeO₃ film on Al₂O₃(0001) with 2θ angle of 10-100°. * correspond to the peaks of substrates.

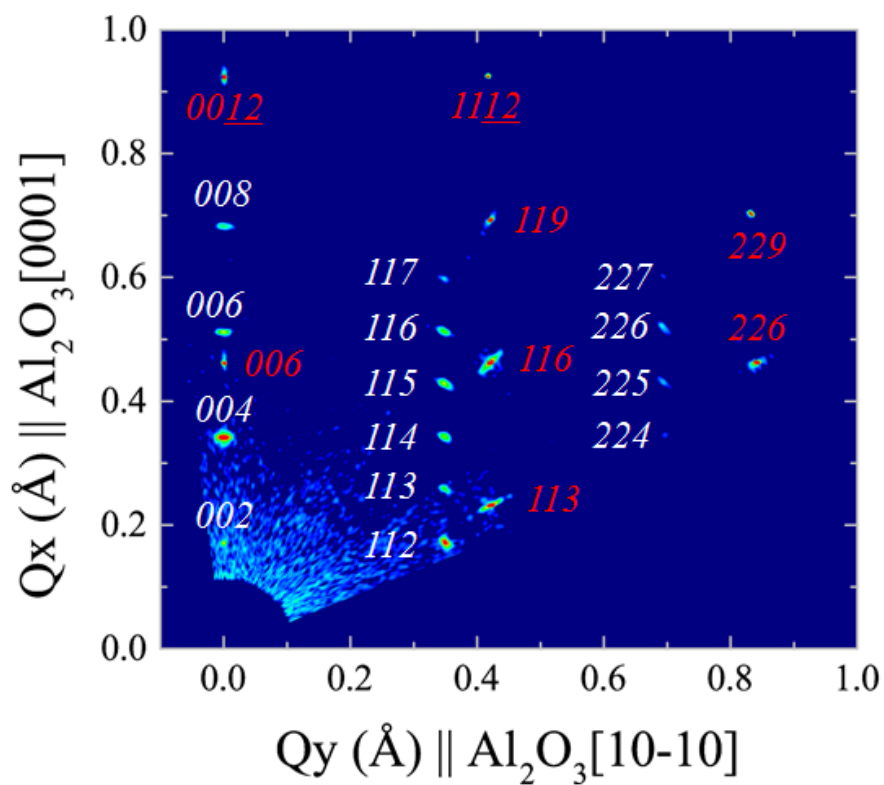


Figure 2-13 2D RSM of ScFeO₃ film on Al₂O₃(0001) along Al₂O₃[10-10]. Red and white indexes indicate Al₂O₃ substrate and ScFeO₃ film, respectively.

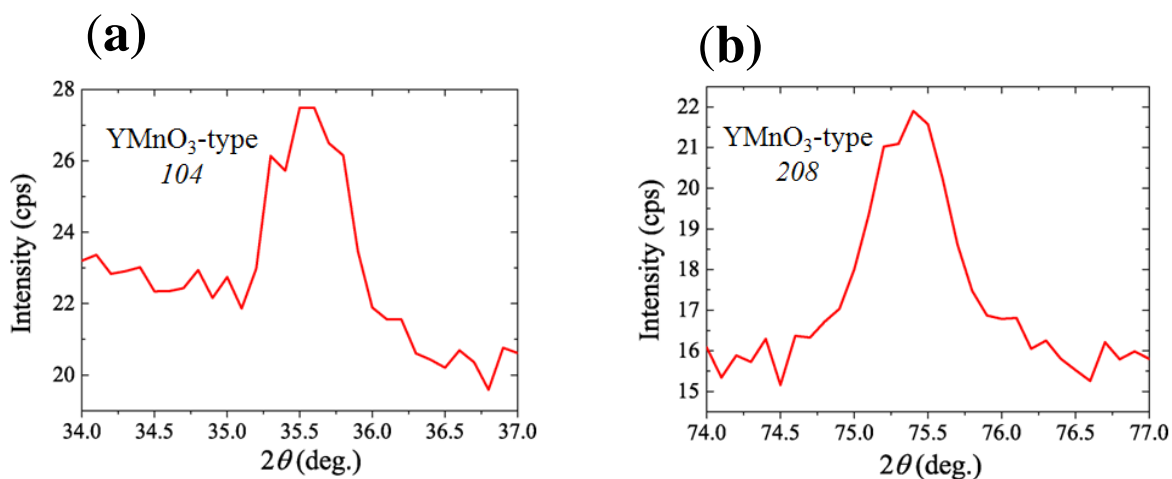


Figure 2-14 XRD ω - 2θ pattern around 104 (a) and 208 (b) of ScFeO₃ film on Al₂O₃(0001)

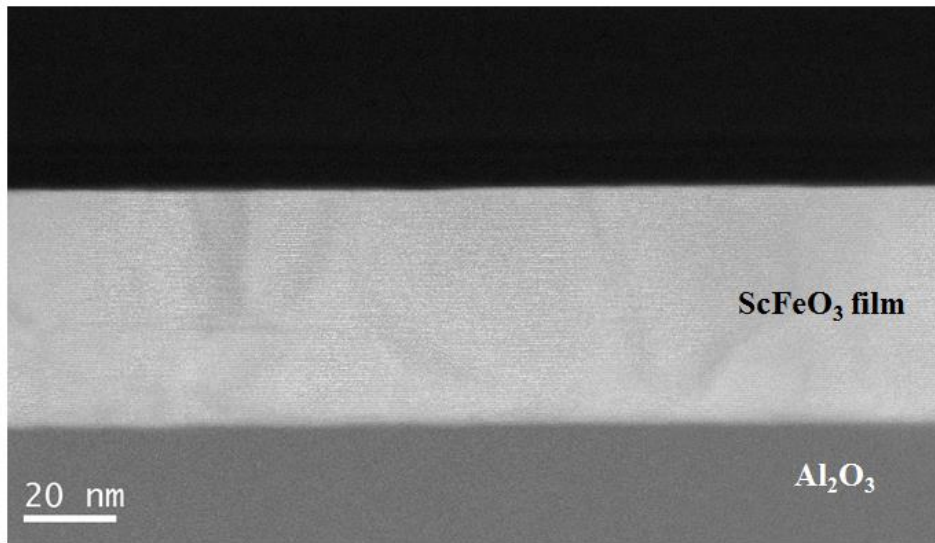


Figure 2-15 Cross sectional HAADF-STEM image of ScFeO₃ film on Al₂O₃(0001).

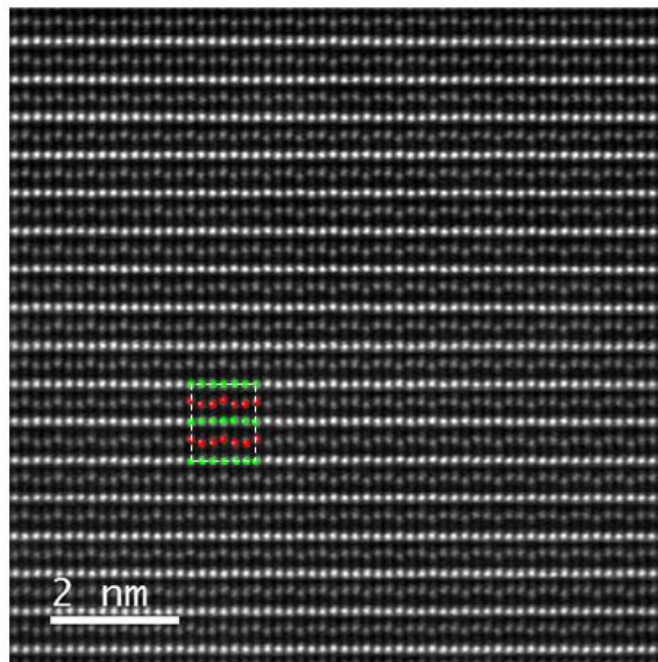
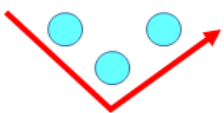
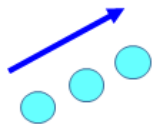
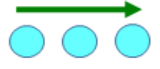


Figure 2-16 HAADF-STEM image of ScFeO₃ film on Al₂O₃(0001). The direction of view is Al₂O₃ [10-10]. Simulated cationic positions and the unit cell are indicated by circles and broken lines, respectively.

	$P6_3cm$	$P-3c1$	$P6_3/mmc$
XRD SL 104, 204	Yes	Yes	No
TEM			
P-E hys	Yes	No	No

● Re

Figure 2-17 The difference of crystal structures ($P6_3cm$, $P-3c1$ and $P6_3/mmc$)

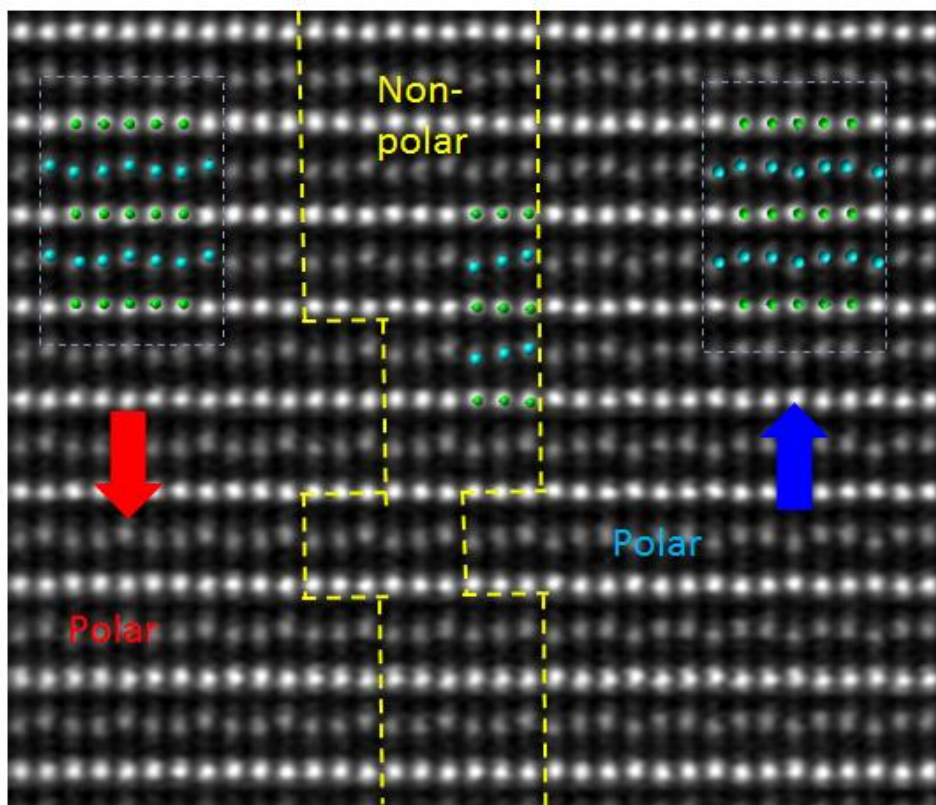


Figure 2-18 HAADF-STEM image around 180° domain boundary.

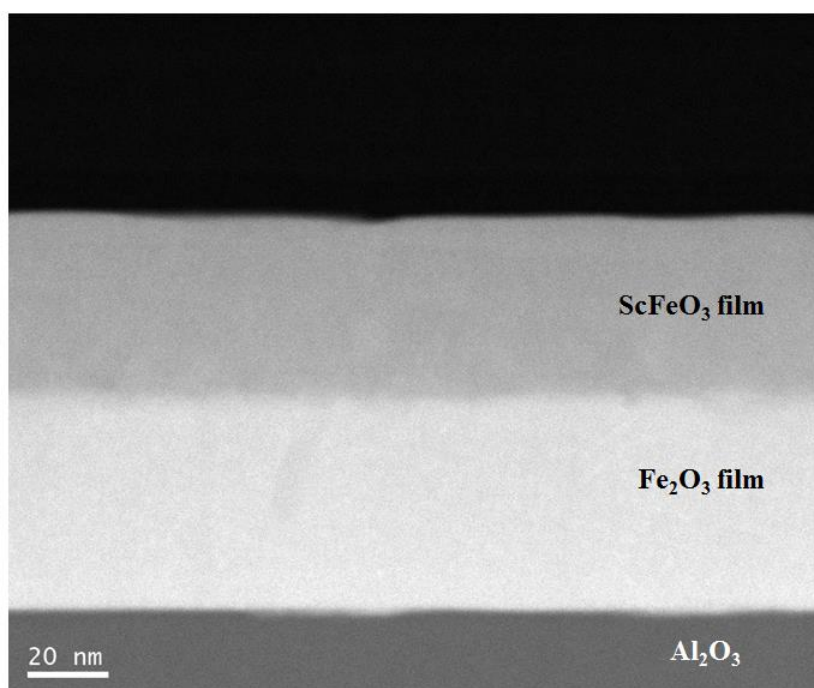


Figure 2-19 Cross sectional HAADF-STEM image of ScFeO₃ film on Fe₂O₃/Al₂O₃(0001)

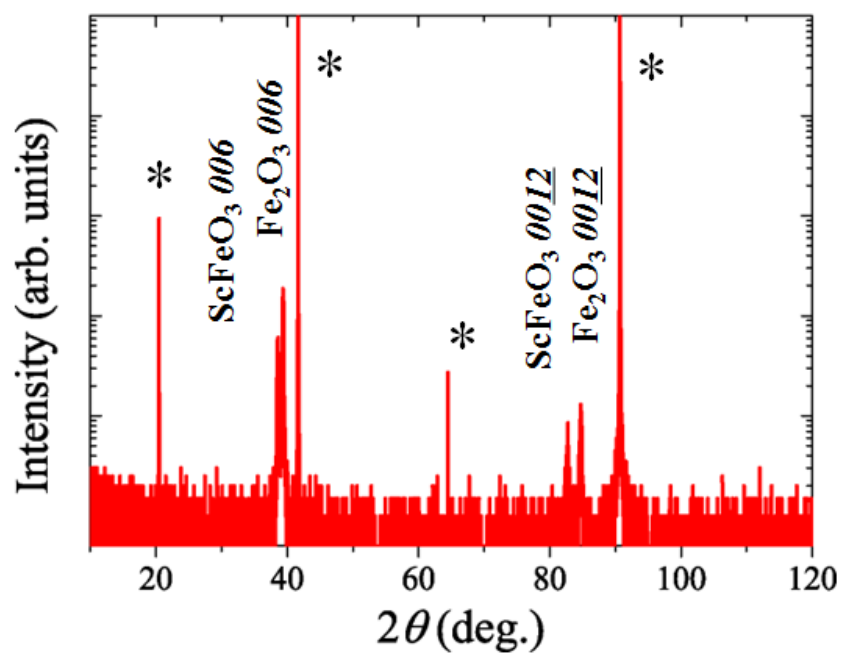


Figure 2-20 XRD θ - 2θ pattern of ScFeO₃ film on Fe₂O₃/Al₂O₃(0001) with 2θ angle of 10-100°. * correspond to the peaks of substrates.

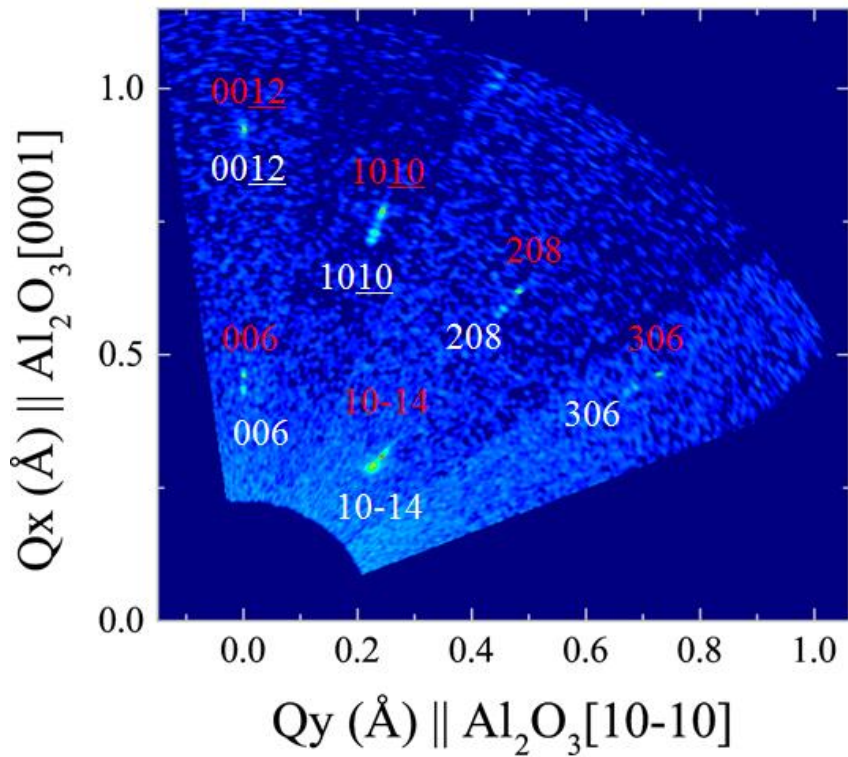


Figure 2-21 2D RSM of ScFeO_3 film on $\text{Fe}_2\text{O}_3/\text{Al}_2\text{O}_3(0001)$ along $\text{Al}_2\text{O}_3[10-10]$. Red and white indexes indicate Al_2O_3 substrate and ScFeO_3 film, respectively.

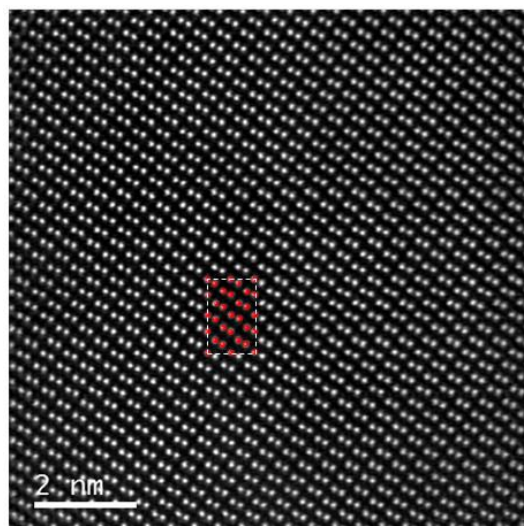


Figure 2-22 HAADF-STEM image of ScFeO_3 film on $\text{Fe}_2\text{O}_3/\text{Al}_2\text{O}_3(0001)$. The direction of view is $\text{Al}_2\text{O}_3 [10-10]$. Simulated cationic positions and the unit cell are indicated by circles and broken lines, respectively.

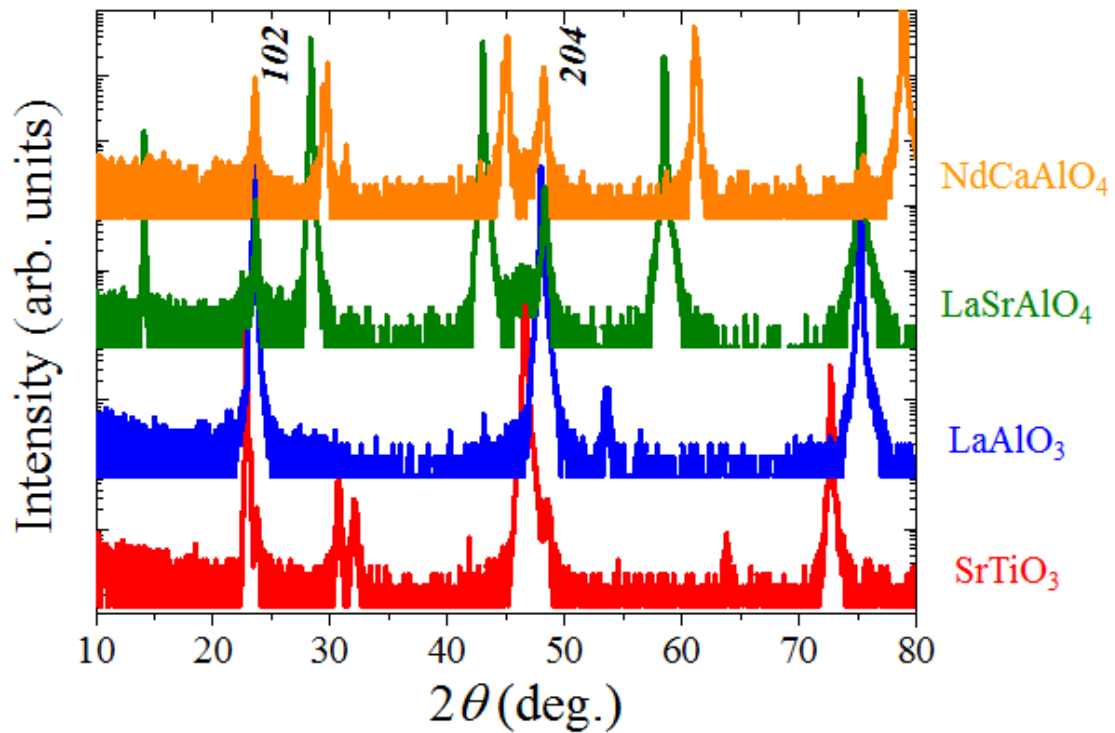


Figure 2-23 XRD θ - 2θ pattern of ScFeO₃ film on NdCaAlO₄(001), LaSrAlO₄(001), LaAlO₃(001) and SrTiO₃(001) substrates.* correspond to the peaks of substrates.

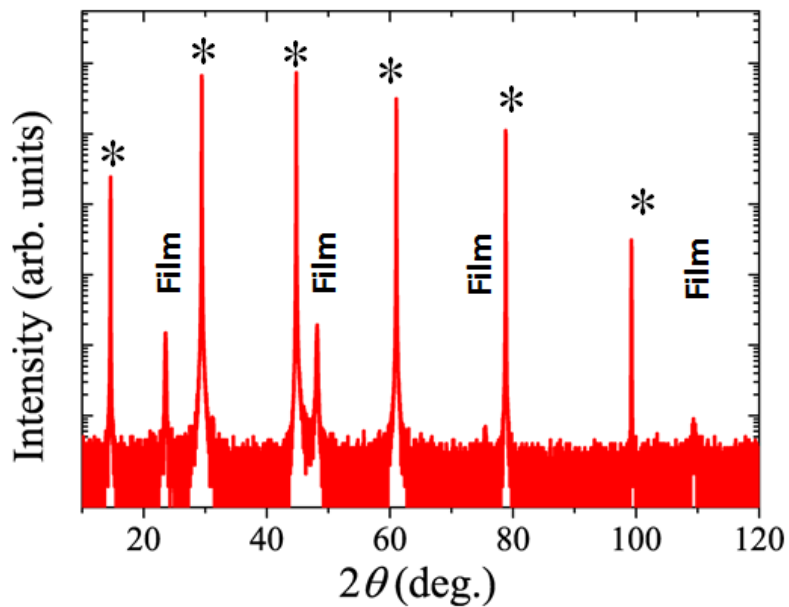


Figure 2-24 XRD θ - 2θ pattern of ScFeO₃ film on NdCaAlO₄(001) substrate.* correspond to the peaks of substrates.

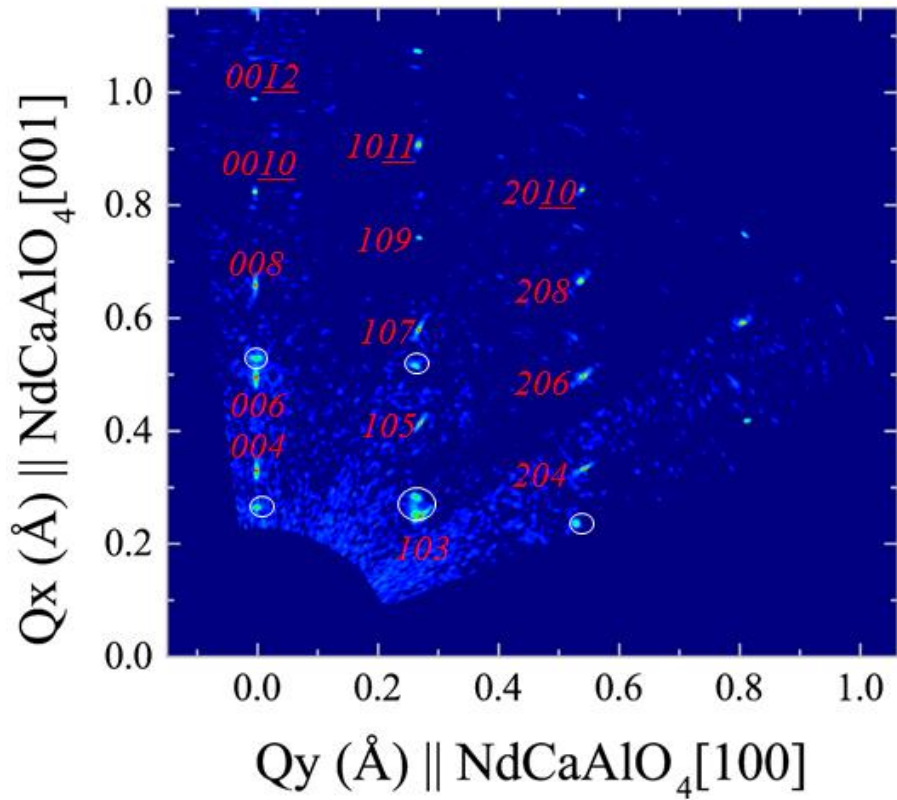


Figure 2-25 2D RSM of ScFeO_3 film on $\text{NdCaAlO}_4(001)$ along NdCaAlO_4 $[100]$.

Red indexes and white circle indicate Al_2O_3 substrate and ScFeO_3 film, respectively

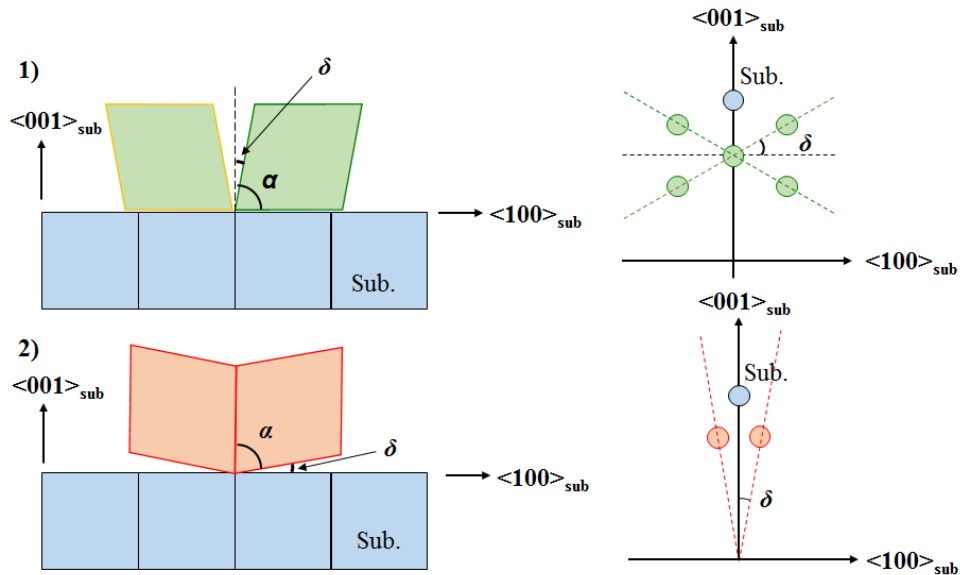


Figure 2-26 Schematic illustrate of two kinds of domain structures and XRD patterns.

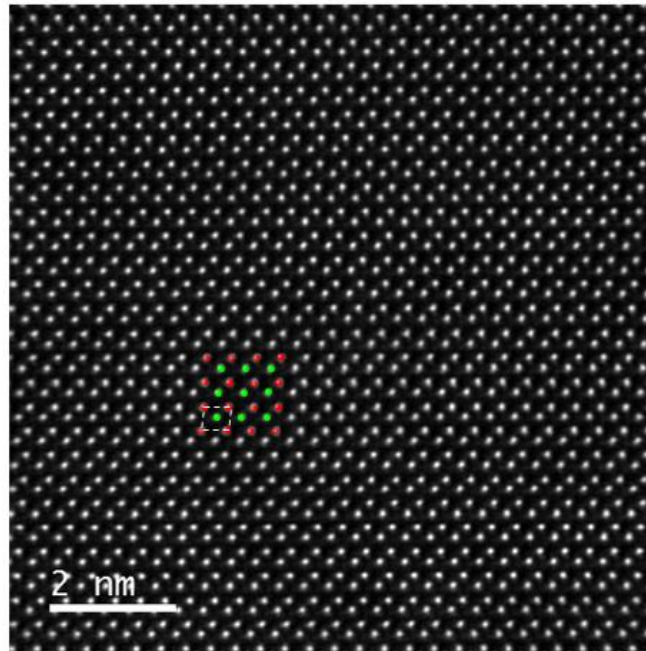


Figure 2-27 HAADF-STEM image of ScFeO_3 film on $\text{NdCaAlO}_4(001)$. The direction of view is NdCaAlO_4 [100]. Simulated cationic positions and the unit cell are indicated by circles and broken lines, respectively.

Table 2-1. Summary of the crystal structures of ScFeO₃ films deposited on various substrates. Rectangle, triangle, and square indicate two-, three- and four-fold in-plane symmetry, respectively.

Main phase	Out-of-plane direction	In-plane symmetry	Substrate	In-plane symmetry	Secondary Phase
κ -Al ₂ O ₃ -type	001	□	SrTiO ₃ (111)	△	-
Spinel-type	001	□	MgO(001)	□	-
Corundum-type	0001	△	Fe ₂ O ₃ /Al ₂ O ₃ (0001)	△	-
	012	□	NdCaAlO ₄ (001)	□	-
	012	□	LaSrAlO ₄ (001)	□	unknown
YMnO ₃ -type	0001	△	Al ₂ O ₃ (0001)	△	-
	0001	△	SrTiO ₃ (001)	□	Bixbyite-type
	0001	△	MgAl ₂ O ₄ (001)	□	-
	0001	△	MgAl ₂ O ₄ (111)	△	-
Bixbyite-type	001	□	YSZ(001)	□	-
	111	△	YSZ(111)	△	YMnO ₃ -type
	111	△	ITO/YSZ(111)	△	-
	111	△	MgO(111)	△	-
	111	△	Pt/Al ₂ O ₃ (0001)	△	YMnO ₃ -type
	111	△	ZnO/Al ₂ O ₃ (0001)	△	YMnO ₃ -type

References

- [1] N. Ramadass, "ABO₃-Type Oxides - Their Structure and Properties - A Bird's Eye View," *Mater. Sci. Eng.*, vol. 36, no. 1978, pp. 231–239, 1978.
- [2] D. M. Giaquinta and H.-C. zur Loye, "Structural Predictions in the ABO₃ Phase Diagram," *Chem. Mater.*, vol. 6, no. 4, pp. 365–372, 1994.
- [3] Y. Inaguma, M. Yoshida, T. Tsuchiya, A. Aimi, K. Tanaka, T. Katsumata, and D. Mori, "High-pressure synthesis of novel lithium niobate-type oxides," *J. Phys. Conf. Ser.*, vol. 215, p. 012131, 2010.
- [4] Y.-L. Hu, E. Rind, and J. S. Speck, "Antiphase boundaries and rotation domains in In₂O₃(001) films grown on yttria-stabilized zirconia (001)," *J. Appl. Crystallogr.*, vol. 47, no. 1, pp. 443–448, 2014.
- [5] L. MacHala, J. Tuček, and R. Zbořil, "Polymorphous transformations of nanometric iron(III) oxide: A review," *Chem. Mater.*, vol. 23, no. 14, pp. 3255–3272, 2011.
- [6] A. a. Bossak, I. E. Graboy, O. Y. Gorbenko, A. R. Kaul, M. S. Kartavtseva, V. L. Svetchnikov, and H. W. Zandbergen, "XRD and HREM Studies of Epitaxially Stabilized Hexagonal Orthoferrites RFeO₃ (R = Eu-Lu)," *Chem. Mater.*, vol. 16, no. 9, pp. 1751–1755, 2004.
- [7] D. Lee, J.-H. Lee, P. Murugavel, S. Y. Jang, T. W. Noh, Y. Jo, M.-H. Jung, Y.-D. Ko, and J.-S. Chung, "Epitaxial stabilization of artificial hexagonal GdMnO₃ thin films and their magnetic properties," *Appl. Phys. Lett.*, vol. 90, no. 18, p. 182504, 2007.
- [8] J.-H. Lee, P. Murugavel, H. Ryu, D. Lee, J. Y. Jo, J. W. Kim, H. J. Kim, K. H. Kim, Y. Jo, M.-H. Jung, Y. H. Oh, Y.-W. Kim, J.-G. Yoon, J.-S. Chung, and T.

- W. Noh, "Epitaxial Stabilization of a New Multiferroic Hexagonal Phase of TbMnO₃ Thin Films," *Adv. Mater.*, vol. 18, no. 23, pp. 3125–3129, 2006.
- [9] A. Masuno, A. Ishimoto, C. Moriyoshi, H. Kawaji, Y. Kuroiwa, and H. Inoue, "Expansion of the Hexagonal Phase-Forming Region of Lu_{1-x}Sc_xFeO₃ by Containerless Processing," *Inorg. Chem.*, vol. 54, no. 19, pp. 9432–9437, 2015.
- [10] S. J. Ahn, J. H. Lee, Y. K. Jeong, E. H. Na, Y. M. Koo, and H. M. Jang, "Artificially imposed hexagonal ferroelectricity in canted antiferromagnetic YFeO₃ epitaxial thin films," *Mater. Chem. Phys.*, vol. 138, no. 2–3, pp. 929–936, 2013.
- [11] D. M. Giaquinta, W. M. Davis, and H. C. zur Loye, "Structure of indium iron oxide," *Acta Crystallogr. Sect. C Cryst. Struct. Commun.*, vol. 50, no. 1, pp. 5–7, 1994.
- [12] W. Wang, J. Zhao, W. Wang, Z. Gai, N. Balke, M. Chi, H. N. Lee, W. Tian, L. Zhu, X. Cheng, D. J. Keavney, J. Yi, T. Z. Ward, P. C. Snijders, H. M. Christen, W. Wu, J. Shen, and X. Xu, "Room-Temperature Multiferroic Hexagonal LuFeO₃ Films," *Phys. Rev. Lett.*, vol. 110, no. 23, p. 237601, 2013.
- [13] Y. Kumagai, A. a. Belik, M. Lilienblum, N. Leo, M. Fiebig, and N. a. Spaldin, "Observation of persistent centrosymmetry in the hexagonal manganite family," *Phys. Rev. B - Condens. Matter Mater. Phys.*, vol. 85, no. 17, pp. 1–7, 2012.
- [14] V. V. Roddatis, A. R. Akbashev, S. Lopatin, and A. R. Kaul, "Complex structural-ferroelectric domain walls in thin films of hexagonal orthoferrites RFeO₃ (R = Lu, Er)," *Appl. Phys. Lett.*, vol. 103, pp. 1–6, 2013.
- [15] F. T. Huang, X. Wang, Y. S. Oh, K. Kurushima, S. Mori, Y. Horibe, and S. W.

- Cheong, “Delicate balance between ferroelectricity and antiferroelectricity in hexagonal InMnO_3 ,” *Phys. Rev. B - Condens. Matter Mater. Phys.*, vol. 87, no. 18, pp. 2–5, 2013.
- [16] T. Oshima, T. Okuno, and S. Fujita, “ Ga_2O_3 Thin Film Growth on c -Plane Sapphire Substrates by Molecular Beam Epitaxy for Deep-Ultraviolet Photodetectors,” *Jpn. J. Appl. Phys.*, vol. 46, no. 11, pp. 7217–7220, 2007.
- [17] N. Suzuki, K. Kaneko, and S. Fujita, “Growth of corundum-structured In_2O_3 thin films on sapphire substrates with Fe_2O_3 buffer layers,” *J. Cryst. Growth*, vol. 364, pp. 30–33, 2013.
- [18] H. D. Megaw, “A note on the structure of lithium niobate, LiNbO_3 ,” *Acta Crystallogr. Sect. A Cryst. Physics, Diffraction, Theor. Gen. Crystallogr.*, vol. 24, no. 6, pp. 583–588, 1968.
- [19] H. D. Megaw and C. N. W. Darlington, “Geometrical and structural relations in the rhombohedral perovskites,” *Acta Crystallogr. Sect. A*, vol. 31, no. 2, pp. 161–173, 1975.
- [20] M. A. Tagliente, L. De Caro, A. Sacchetti, L. Tapfer, G. Balestrino, P. G. Medaglia, A. Tebano, and A. Tucciarone, “X-ray characterization of LiNbO_3 films grown by pulsed laser deposition on SrTiO_3 (1 0 0),” *J. Cryst. Growth*, vol. 216, pp. 335–342, 2000.
- [21] S. Yasui, H. Naganuma, S. Okamura, K. Nishida, T. Yamamoto, T. Iijima, M. Azuma, H. Morioka, K. Saito, M. Ishikawa, T. Yamada, and H. Funakubo, “Crystal Structure and Electrical Properties of {100}-Oriented Epitaxial BiCoO_3 – BiFeO_3 Films Grown by Metalorganic Chemical Vapor Deposition,” *Jpn. J. Appl. Phys.*, vol. 47, no. 9, pp. 7582–7585, 2008.

Chapter 3

$\text{Al}_2\text{O}_3\text{-Fe}_2\text{O}_3$ System

3.1 Introduction

It is well known that the stable phase of Al_2O_3 and Fe_2O_3 is corundum. In Al_2O_3 - Fe_2O_3 phase diagram, two phases of corundum-type alumina and ferrite coexist (Figure 3-1)[1]. This can be explained by the Hume-Rothery rule, and the radius of Al^{3+} (0.53 Å) is about 10 % smaller than that of Fe^{3+} (0.64 Å). Therefore, it is difficult to be formed $\text{Al}_x\text{Fe}_{2-x}\text{O}_3$ solid solution. At AlFeO_3 composition, κ - Al_2O_3 -type structure is stable above 1300°C, however this phase decompose to two corundum phase on cooling [2]. It is difficult to prepare κ - Al_2O_3 -type AlFeO_3 by a combinational solid reaction. Note that κ - Al_2O_3 -type AlFeO_3 is solid solution between κ - Al_2O_3 and ε - Fe_2O_3 [3], [4]. Both κ - Al_2O_3 and ε - Fe_2O_3 are metastable phase. κ - Al_2O_3 is obtained by heat treatment of aluminum hydroxide and hydrate such as γ - $\text{Al}(\text{OH})_3$ (gibbsite) and $5\text{Al}_2\text{O}_3 \cdot \text{H}_2\text{O}$ (tohdite)[5]. ε - Fe_2O_3 is prepared by combining revers micelle and sol-gel technique and the size of particle is important factor to stabilize ε - Fe_2O_3 [6]. κ - Al_2O_3 -type structure have the non-centrosymmetric space group (S.G.) of $Pna2_1$ and is polar. Due to the polar structure, a ferroelectricity is expected in κ - Al_2O_3 -type structure. In bulk, ferroelectric polarization-electric filed hysteresis loop have not been reported because of leak currents. In this study, we focused on the film technique. The film technique sometimes make stabilization of a metastable phase possible. In this chapter, we attempted to stabilize κ - Al_2O_3 -type $\text{Al}_x\text{Fe}_{2-x}\text{O}_3$ by PLD technique and investigate ferroelectricity in κ - Al_2O_3 -type $\text{Al}_x\text{Fe}_{2-x}\text{O}_3$ films.

3.2 Experiment

$\text{Al}_x\text{Fe}_{2-x}\text{O}_3$ films were grown on $\text{SrTiO}_3(111)$ single-crystal substrates by PLD technique. A fourth-harmonic wave of a Nd: YAG laser ($\lambda = 266 \text{ nm}$) was used. A

repetition rate and a fluence of a Nd: YAG laser are 5Hz and 2.4, respectively. The target was prepared by mixing α -Al₂O₃ and α -Fe₂O₃ powder and sintering at 1450°C for 14 hours in air. Chemical composition of targets are Al₂O₃, Al_{1.8}Fe_{0.2}O₃, Al_{1.5}Fe_{0.5}O₃, AlFeO₃, Al_{0.5}Fe_{1.5}O₃ and Fe₂O₃. The crystal structure of films were investigated by high-resolution X-ray diffraction (XRD) using a Rigaku Smart-Lab diffractometer. X-ray was monochromatized using a Ge(220) 2-bounce crystal and Cu K α radiation ($\lambda=1.5406 \text{ \AA}$) was used. The Reciprocal space mapping (RSM) was measured to estimate to lattice constants. Atomic force microscopy (AFM) and piezo-response force microscopy (PFM) images was recorded by SPI 4000. P-E hysteresis loop was measured by ferroelectric tester (Toyo Corporation, FCE) Pt as top electrode was deposited by the electric beam evaporation method.

3.3 Result and Discussion

3.3.1 Growth of AlFeO₃ Film

It is reported that κ -Al₂O₃-type compounds such as GaFeO₃ and ϵ -Fe₂O₃ were grown on SrTiO₃(111) substrates [7], [8]. In the GaFeO₃-type structure, closed packing oxygen layers are stacked along c axis with the pattern of ABACABAC·····, where A, B and C are closed packing layers [9]. The arrangement of oxygen ions in κ -Al₂O₃-type structure are similar that of SrTiO₃(111) substrates. In this study, we selected to SrTiO₃(111) single crystal substrates to stabilize κ -Al₂O₃-type AlFeO₃. AlFeO₃ film was deposited on SrTiO₃(111) substrate under 100mTorr in O₂. During the deposition, the substrate was kept at 800°C. XRD 2θ - θ pattern of AlFeO₃ film was shown in Figure 3-2. Four peaks at $2\theta = 19.12^\circ$, 38.81° , 59.79° and 83.31° without that of substrates were observed. These peaks were corresponded to 002, 004, 006 and 008 reflections of κ -Al₂O₃-type

structures. The result indicates that κ -Al₂O₃-type AlFeO₃ was epitaxially grown on SrTiO₃(111) substrate with the out of plane orientation relationship of κ -Al₂O₃-type AlFeO₃(001) \parallel SrTiO₃(111) without impurity phase. The *c* lattice constant of AlFeO₃ film estimated from out of plane pattern was 9.271 Å. The full-width-at-half-maximum (FWHM) value of rocking curve was measured at 008 reflections. The measured value of FWHM was 0.135°, suggesting a well-crystallized and high quality film. In order to characterize in-plane relationship, phi scan was carried out around the AlFeO₃{201} and SrTiO₃{110} reflections as shown Figure 3-3. Three SrTiO₃(110) peaks at 120° intervals were observed, whereas six AlFeO₃(201) peaks at 60° intervals were observed. This result indicates that κ -Al₂O₃-type AlFeO₃ film on SrTiO₃(111) substrate has three in-plane domains rotated 120° from each other, reflecting the three-fold symmetry of the SrTiO₃(111) plane. The in-plane relationship between AlFeO₃ film and SrTiO₃ substrate can be described as AlFeO₃[100] \parallel SrTiO₃[11-2], AlFeO₃[100] \parallel SrTiO₃[1-21] and AlFeO₃[100] \parallel SrTiO₃[-211], respectively. Figure 3-4 shows the schematic illustrate of the in-plane relationship. RSM were measured around AlFeO₃ $20\bar{1}0$ and SrTiO₃ $3\bar{1}3$ reflections (Figure 3-5). In-plane lattice constants of AlFeO₃ film was different from that of SrTiO₃ substrate. This result implied that there were not lattice strain in AlFeO₃ film on SrTiO₃ substrate. We also performed in-plane $2\theta_{\chi}$ - ϕ scan along SrTiO₃[11-2] and SrTiO₃[1-10] directions. In $2\theta_{\chi}$ - ϕ scan along SrTiO₃[11-2], 200 and 400 reflections of κ -Al₂O₃-type AlFeO₃ were observed (Fig. 3-6). In $2\theta_{\chi}$ - ϕ scan along SrTiO₃[1-10], 060 reflection of κ -Al₂O₃-type AlFeO₃ was observed (Fig. 3-7). These results were consisted with the in-plane relationship investigated from phi scan. From these results, the in-plane epitaxy was confirmed. The film surface was characterized by AFM (Fig. 3-8). AFM image reveals that particles with a diameter of about 300 nm formed in

AlFeO₃ film. The structures reflecting three in-plane domains were not observed. The surface roughness root mean square (RMS) value was 2.19 nm, suggesting smooth surface.

We also deposited AlFeO₃ at various condition. First, AlFeO₃ films were deposited under 1, 20, 50 and 100 mTorr. The substrates were kept at 800 °C. Out of plane XRD pattern of AlFeO₃ deposited under various oxygen pressure was shown in Figure 3-9. AlFeO₃ film deposited under 20, 50 and 100 mTorr have single phase κ -Al₂O₃-type structure, which AlFeO₃ film deposited under 1 mTorr decomposed. In this study, we evaluated the quality of AlFeO₃ films by FWHM of rocking curve. FWHM values of AlFeO₃ films were listed in Table 3-1 with oxygen pressure. FWHM values of AlFeO₃ films decreased with increasing oxygen pressure. This result indicates that AlFeO₃ film deposited under high oxygen pressure was well crystallized. Then, AlFeO₃ films were deposited at 600, 700, 800 and 900 °C under 100 mTorr. Figure 3-10 show the results of XRD 2 θ - θ pattern. AlFeO₃ films deposited at 600 °C had two κ -Al₂O₃-type phase i.e. Fe rich and Al rich GaFeO₃ type AlFeO₃. In AlFeO₃ films deposited at 900 °C, single GaFeO₃-type phase was not obtained. The impurity phase was not corundum phase and was not determined. AlFeO₃ films deposited at 700 and 800 °C were epitaxially grown without impurity phase. FWHM values of AlFeO₃ films were listed in Table 3-2 with substrate temperature. FWHM values of AlFeO₃ films at 700 and 800 °C were 0.204° and 0.135°, respectively, indicating that the substrate temperature of 800 °C was better for AlFeO₃ film. Therefore, the best deposition condition of AlFeO₃ is at 800 °C under 100mTorr.

3.3.2 Stabilization of κ -Al₂O₃-type Al_xFe_{2-x}O₃ films

In order to investigate the stability of κ -Al₂O₃-type structure in Al₂O₃-Fe₂O₃ system, Al_xFe_{2-x}O₃ films ($x = 0, 0.5, 1.0, 1.5, 1.8$ and 2.0) were deposited on SrTiO₃(111) substrates. Here, Fe₂O₃, Al_{1.8}Fe_{0.2}O₃ films were deposited at different conditions. However, Fe₂O₃ film deposited at the same condition as AlFeO₃ film, κ -Al₂O₃-type Fe₂O₃ was not grown. Though the obtained Fe₂O₃ film shows a deep orange color like hematite, the diffraction peaks were not observed in XRD 2θ - θ pattern. Growth of Fe₂O₃ film was sensitive to the growth rate. Therefore, the low laser fluence with 0.96 J/cm² was used for Fe₂O₃ film. Al_{1.8}Fe_{0.2}O₃ film was deposited at 800 °C under 1 mTorr. The laser fluence with 2.88 J/cm² was used for Al_{1.8}Fe_{0.2}O₃ film. However, Al₂O₃ film was deposited at various deposited conditions, κ -Al₂O₃-type structure Al₂O₃ was obtained. XRD 2θ - θ patterns of Al_xFe_{2-x}O₃ films ($x = 0, 0.5, 1.0, 1.5$ and 1.8) displayed in Figure 3-11. All films showed four peaks corresponding to (002 l) diffractions of κ -Al₂O₃-type structures. Therefore, we have succeeded in stabilizing κ -Al₂O₃-type structures in Al_xFe_{2-x}O₃ ($x = 0-1.8$). It can be observed from Figure 3-11 that the peaks were shifted to high angle with increasing Al contents. The c lattice constant changes estimated from 2θ - θ scan were reported in Figure 3-12(c). The c lattice constants of Al_xFe_{2-x}O₃ films monotonically decreased with increasing Al contents because Al³⁺ ionic radius (0.535 Å) is smaller than that of Fe³⁺ (0.645 Å). The in-plane relationship between films and substrates was probed by XRD ϕ -scan. As with AlFeO₃ film, films show the six-fold symmetry reflecting three-fold symmetry in SrTiO₃(111), i.e. there are in-plane domains rotated 120° each other in Al_xFe_{2-x}O₃ films. RSM of Al_xFe_{2-x}O₃ films were performed around Al_xFe_{2-x}O₃{2010} and Al_xFe_{2-x}O₃{057} reflections (Figure 3-13, 14). There were no lattice strain in all κ -Al₂O₃-type Al_xFe_{2-x}O₃ films on SrTiO₃ substrate. The a and b lattice

constants were estimated from RSM and were shown in Figure 3-12 (a), (b). Both a and b lattice constants decreased with increasing Al contents as well as the c lattice constants. The unit cell volume of films were plotted on Figure 3-15 with that of bulk [3], [9]–[11]. Unit cell volume of $\text{Al}_x\text{Fe}_{2-x}\text{O}_3$ films clearly show the same tendency for the bulk sample. This result indicates that $\text{Al}_x\text{Fe}_{2-x}\text{O}_3$ film ($x = 0, 0.5, 1.0, 1.5, 1.8$ and 2.0) are κ - Al_2O_3 -type Al_2O_3 - Fe_2O_3 solid solution. The FWHM value with $x = 0, 0.5, 1, 1.5, 1.8$ were $0.08, 0.13, 0.14, 0.17$ and 0.91° , respectively (see Figure 3-16). FWHM value of the film with $x = 1.8$ became larger in one order in magnitude compared to that of films with $x = 0\sim 1.5$, indicating that κ - Al_2O_3 -type $\text{Al}_{1.8}\text{Fe}_{0.2}\text{O}_3$ is near the boundary of the formation on the STO (111) substrate by the PLD technique although deposition conditions of temperature, oxygen partial pressure, and laser fluence were changed in the possible ranges of the experiment. Therefore, the mechanism of the de-stabilization of the κ - Al_2O_3 -type phase near $x \sim 2.0$ may be attributed to the chemical origin.

Lattice mismatches between ε - Fe_2O_3 and SrTiO_3 substrates is 6.50% for the directions ε - Fe_2O_3 [100] and SrTiO_3 [1-21], and 6.01% for the directions ε - Fe_2O_3 [010] and SrTiO_3 [10-1], respectively. On the other hand, lattice mismatches between κ - Al_2O_3 and SrTiO_3 substrates is 1.28% for the directions ε - Fe_2O_3 [100] and SrTiO_3 [1-21], and 0.55% for the directions κ - Al_2O_3 [010] and SrTiO_3 [10-1], respectively. From the viewpoint of lattice mismatch, films on SrTiO_3 (111) substrates should be more stable with increasing Al contents. However, we did not get a result reflecting the expectation from the value of lattice mismatches. Orthorhombic κ - Al_2O_3 -type structure can be described as pseudohexagonal structure. Here, orthorhombicity was defined by $\sqrt{3}a/b$. When $\sqrt{3}a/b = 1$, the symmetry of unit cell with this ratio is hexagonal (Figure 3-17). In the case of $\sqrt{3}a/b \neq 1$, the symmetry of unit cell with this ratio is orthorhombic. Because

orthorhombicity of κ -Al₂O₃-type AlFeO₃ is 1.0091, κ -Al₂O₃-type AlFeO₃ is described as pseud-hexagonal structure. Figure 3-18 shows the orthorhombicity of the films and bulk. Orthorhombicity of both films and bulk tend to increase with increasing Al contents. Orthorhombicity of films was smaller than that of bulk. The trend indicate that the symmetry of films become hexagonal compared with that of bulk. Here, SrTiO₃(111) substrates is composed of alternately stacked Ti⁴⁺ and SrO₃⁴⁻ layers. Atomic arrangements of Ti⁴⁺ and SrO₃⁴⁻ layers are hexagonal symmetry. The reason of decreasing orthorhombicity of films might be reflecting hexagonal symmetry in SrTiO₃(111) substrates.

3.3.3 Investigation of Interface by TEM

Crystal structure of AlFeO₃ film was also investigated by TEM. Figure 3-19 (a)-(c) show the bright field, LAADF-STEM and ABF-STEM image of AlFeO₃ film on SrTiO₃(111) substrate in cross section view along SrTiO₃[11-2]. In three images, 100 nm grains were can be find. Moreover, a striped contrast was observed in AlFeO₃ film. This striped structure corresponds to the three in-plane domain revealed by phi-scan. The width of striped structure is about 10nm, which are fine domain. Figure 3-20(a) illustrates the atomic arrangement of cations along AlFeO₃[100]. As can be seen in figure 3-20(b), the atomic arrangement of AlFeO₃ film in HAADF-STEM image clearly matches with that of κ -Al₂O₃-type structure, and consequently κ -Al₂O₃-type AlFeO₃ film is confirmed by HAADF-STEM. Figure 3-21 displays a magnified LAADF-STEM image around interface. At interface, the bottom layer was observed, i.e. κ -Al₂O₃-type AlFeO₃ is epitaxially grown on not SrTiO₃ substrate but bottom layer. Thickness of bottom layer is not uniform and is 2-20 nm. TEM-EDS analysis revealed that the

composition of AlFeO_3 film is equal, indicating that the composition of bottom layer is equal to that of $\kappa\text{-Al}_2\text{O}_3$ -type AlFeO_3 layer (Figure 3-22).

In order to characterize the bottom layer, HAADF STEM image at interface was recorded. Since the intensity is proportional to Z^2 in HAADF STEM image, the spots correspond to cations. Thus, we focused on the cations in bottom layer. It is apparent that the atomic arrangement of bottom layer is different from $\kappa\text{-Al}_2\text{O}_3$ -type AlFeO_3 (Figure 3-23). From the view point of cation arrangement, the angle of cation packing layer of $\kappa\text{-Al}_2\text{O}_3$ -type AlFeO_3 is 45° , whereas that of bottom layer is 60° (Figure 3-24). The bottom layer consists of two layers (A and B), and these two layers are alternately stacked along out of plane (Figure 3-25). Note that bottom layer mainly consists of layer A and the height of each layer A is different. It seems that cation arrangement of layer A are closed packing. In general, the cations are in space between closed packing oxygen layers, since ionic radius of oxygen anion is larger than that of cation. Therefore, the closed packing arrangement of cations is a rare case. The closed packing arrangement of cations is found in bixbyite-type structure. Bixbyite-type structure is one of few oxides with closed packing cations. Figure 3-26 illustrates the arrangement of cations in bixbyite-type structure. Comparing the cation arrangement of layer A and bixbyite-type structure, it seems that crystal structure of layer A is similar to bixbyite-type structure. In the case of layer B, the pillar structure was observed. This pillar structure can be explained by stacking fault of layer A. Therefore, the bottom layer is the oxide with distorted closed-packing cations and due to distortion there are stacking faults.

3.3.4 Ferroelectric Property by PFM

In order to investigate the ferroelectricity of $\kappa\text{-Al}_2\text{O}_3$ -type AlFeO_3 film, PFM

measurement was performed. SrRuO₃ film as a bottom electrode was deposited on SrTiO₃(111) substrate. Then, AlFeO₃ film was deposited at 700 °C under 100 mTorr on SrRuO₃/SrTiO₃(111). In the AlFeO₃ film deposited at 800°C, impurity phase was observed. To ensure oxygen stoichiometry, the AlFeO₃ film was subjected to in-situ post-growth annealing at 600 °C under 760 Torr of O₂ for 1 hour. The XRD 2 θ - θ pattern revealed that κ -Al₂O₃-type AlFeO₃ was epitaxially grown on SrRuO₃(111)/SrTiO₃(111) (see Figure 3-27).

The topographic AFM image of κ -Al₂O₃-type AlFeO₃ film was shown in Figure 3-28 (a). PFM images were recorded along substrate surface normal because spontaneous polarization of κ -Al₂O₃-type AlFeO₃ is parallel to the *c*-axis direction. Note that since κ -Al₂O₃-type structure is uniaxial ferroelectric, 180 ° ferroelectric domains should form. To investigate the polarization reversal, the square pattern was written by conducting cantilever during an applied dc voltage. The film was first poled at a negative dc bias (-40 V) applied through a conducting cantilever over a 15×15 μm^2 area. Then, the second switching poling was performed with a positive voltage (+35 V) during a scan over a 10×10 μm^2 area and finally performed with a negative voltage (-40 V) during a scan over a 5×5 μm^2 area. Figure 3-28(b) and (c) shows the phase image of vertical piezoresponse at room temperature after poling treatment as above mentioned and the amplitude image. This phase image clearly shows a distinct contrast between positively and negatively poled areas. In the amplitude image, the domains boundary show black color. Because the domains boundary is non-polar region, the amplitude goes to zero. These results indicate that the polarization can be reversed by the applying the dc bias, i.e. κ -Al₂O₃-type AlFeO₃ is ferroelectric. The figure 3-29 displays the phase image before the poling by the external dc bias. The clear ferroelectric domain cannot be

found. Due to the nanoscale domain revealed by HAADF STEM, the signal can not be detected by PFM cantilever.

3.3.5 *P-E* hysteresis loop

In order to investigate the detail of ferroelectricity in κ -Al₂O₃-type Al_xFe_{2-x}O₃ film, we measured electric polarization versus electric field (*P-E*) hysteresis loop. The electric field was applied along the out of plane, which is parallel to the direction of spontaneous polarization in κ -Al₂O₃-type Al_xFe_{2-x}O₃. Top and bottom electrodes were used Pt metal and SrTiO₃: Nb substrate, respectively. *P-E* hysteresis loop of Al_xFe_{2-x}O₃ film was measured at room temperature, however the obtained hysteresis loop showed leaky behavior due to insufficient insulation of Al_xFe_{2-x}O₃ film. In order to decrease leak current, *P-E* hysteresis loop was performed at low temperature. Figure 3-31 shows electric polarization versus electric field hysteresis loops of epitaxial AlFeO₃ and Al_{0.5}Fe_{1.5}O₃ films at 80 K and 30 kHz. Especially, Al_{0.5}Fe_{1.5}O₃ film showed a square-shaped ferroelectric hysteresis loop reflecting 180 ° ferroelectric domain switching. The remnant polarization is about 2 $\mu\text{C}/\text{cm}^2$, and the value is smaller than the calculated value of spontaneous polarization (about 25 $\mu\text{C}/\text{cm}^2$ see appendix). This might be attributed to fact that only partial 180 ° ferroelectric domain under the electrodes were reversed under the applied electric field. The reasons are not only the high activation energies for the polarization switching but also the bottom layer. Here, we consider the effect of bottom layer. The bottom layer observed by HAADF-STEM may be non-polar because structure of bottom layer is based on closed packing cation. Therefore, AlFeO₃ film is described two capacitor which are connected in series; one is ferroelectricity, the other is paraelectricity (Figure 3-32). Here, we suppose that dielectric constant of the

bottom layer is same as that of GaFeO₃-type AlFeO₃. Because each layer store the same amount of electric charge ($Q = Q_f = Q_b$), we get $E_f \cdot \varepsilon_f = E_b \cdot \varepsilon_b$, where Q = charge, E = electric field, ε = permittivity and subscripts of f and b means ferroelectric and bottom layer, respectively. Therefore, the electric field in κ -Al₂O₃-type AlFeO₃ layer is same as that in bottom layer. When ferroelectric materials with virgin state is applied by an electric field, the polarization (P) rapidly increases and reaches a saturation value. Since dielectric response, ε , is described as $\partial D / \partial E$ ($D = \varepsilon_0 E + P$), ε increases rapidly with increasing the polarization. This means that the almost all electric field is applied in the bottom layer and the amount of electric charge is dominated by the bottom layer. The observed polarization is smaller than original one. Therefore, small polarization of AlFeO₃ films can be also explained by the obstruction of the bottom layer.

3.4 Summary

In this chapter, the crystal structure and ferroelectricity of κ -Al₂O₃-type Al_xFe_{2-x}O₃ were investigated. Metastable κ -Al₂O₃-type Al_xFe_{2-x}O₃ ($x = 0-1.8$) thin films were epitaxially grown on SrTiO₃ (111) substrates using PLD method. XRD measurement confirmed three in-plane domains rotated 120° each other. The lattice constants and unit cell volume of κ -Al₂O₃-type Al_xFe_{2-x}O₃ films monotonically decrease with increasing Al contents. HAADF-STEM image revealed the pillar structure with a width of about 10nm, which correspond to three in-plane domains. The bottom layer was also revealed by HAADF-STEM image and crystal structure of the bottom layer is completely different from κ -Al₂O₃-type structure. The ferroelectricity in κ -Al₂O₃-type Al_xFe_{2-x}O₃ films was characterized by PFM and P - E loop measurements. Al_{0.5}Fe_{1.5}O₃ film showed square-shaped ferroelectric hysteresis loop at 80K. The remnant polarization is about 2

$\mu\text{C}/\text{cm}^2$, and the value is smaller than the calculated value of spontaneous polarization (about $25 \mu\text{C}/\text{cm}^2$). The reason might be attributed to the nonpolar bottom layer. From these results, we confirmed ferroelectricity in $\kappa\text{-Al}_2\text{O}_3$ -type $\text{Al}_x\text{Fe}_{2-x}\text{O}_3$ films at first time.

Figures

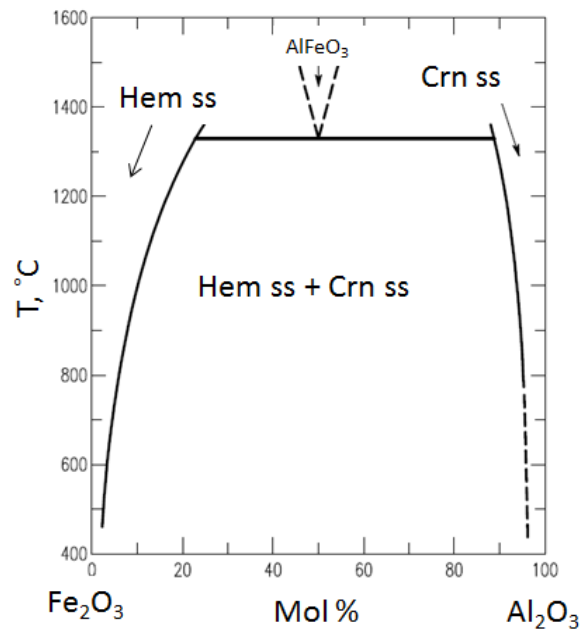


Figure 3-1 Al₂O₃-Fe₂O₃ phase diagram, where ss is solid solution, hem is hematite and crn is corundum.

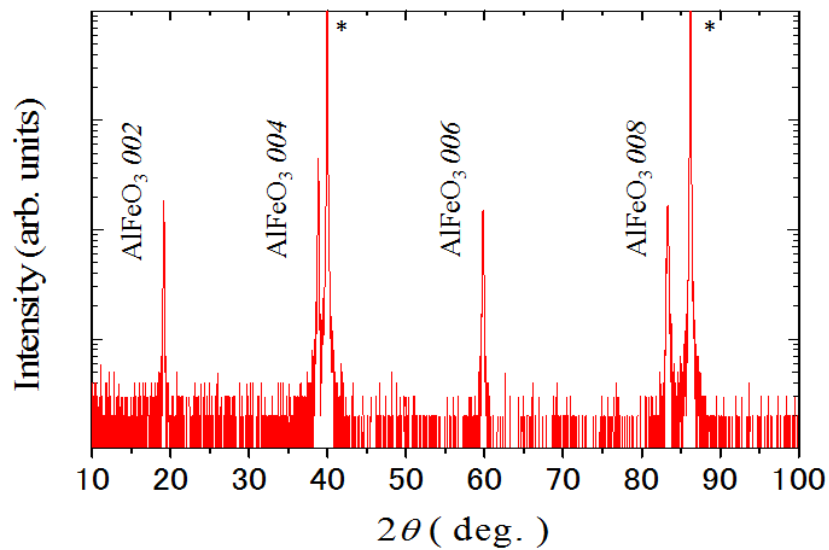


Figure 3-2 XRD θ - 2θ pattern of AlFeO₃ film with 2θ angle of 10-100°. * correspond to the peaks of substrates.

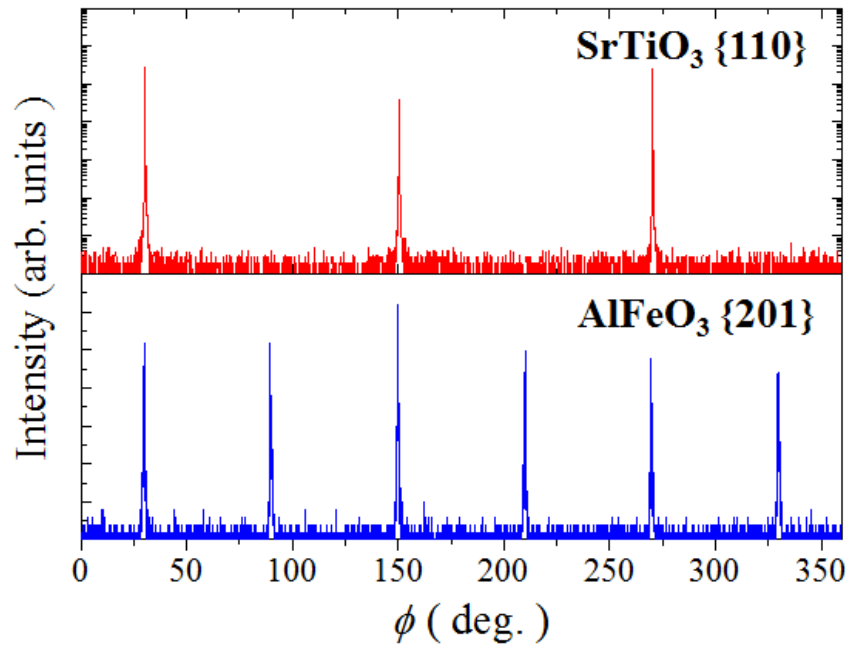


Figure 3-3 XRD ϕ -scan pattern of SrTiO_3 {110} and $\kappa\text{-Al}_2\text{O}_3$ -type AlFeO_3 {201}.

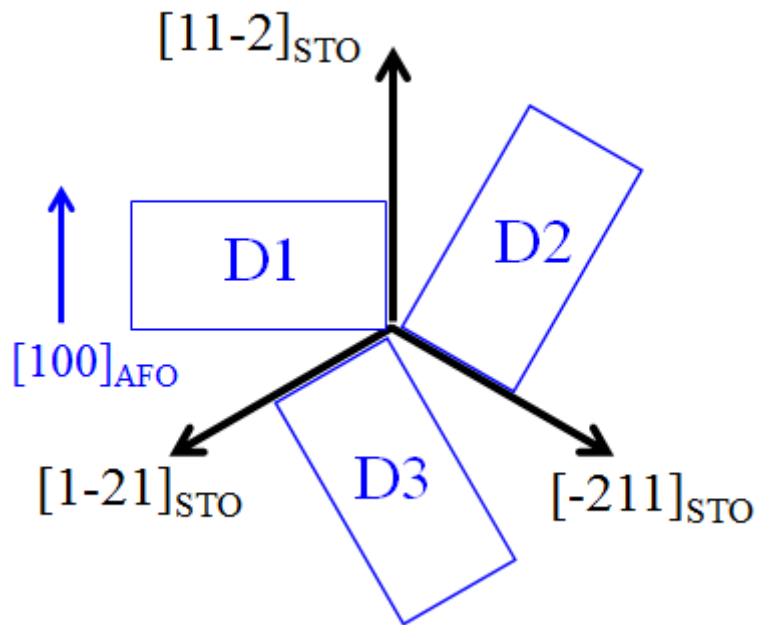


Figure 3-4 Schematic illustrate of three in-plane domains.

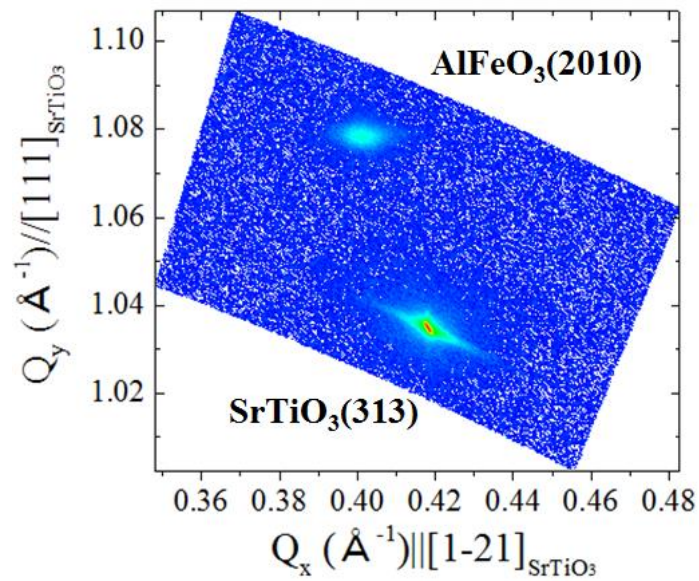


Figure 3-5 XRD-RSM around SrTiO₃(313) and AlFeO₃(2010)

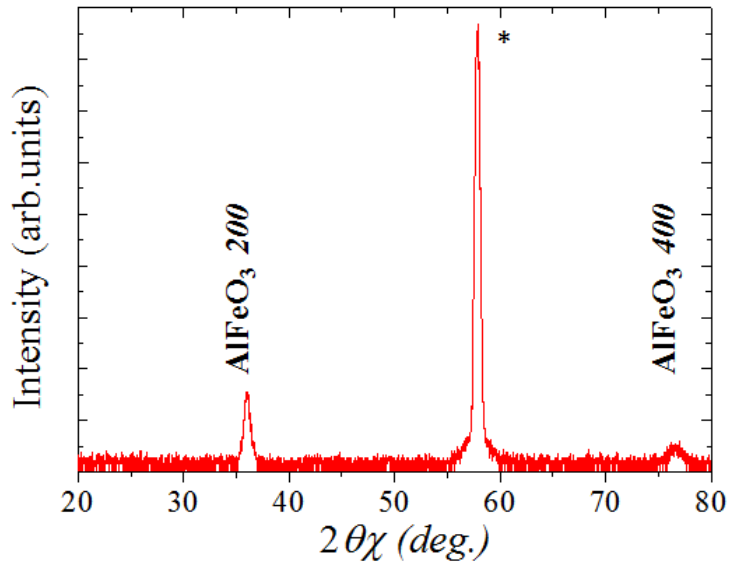


Figure 3-6 ϕ - $2\theta_\chi$ pattern of AlFeO₃ film along SrTiO₃[11-2] with 2θ angle of 20-80°. * correspond to the peaks of substrates.

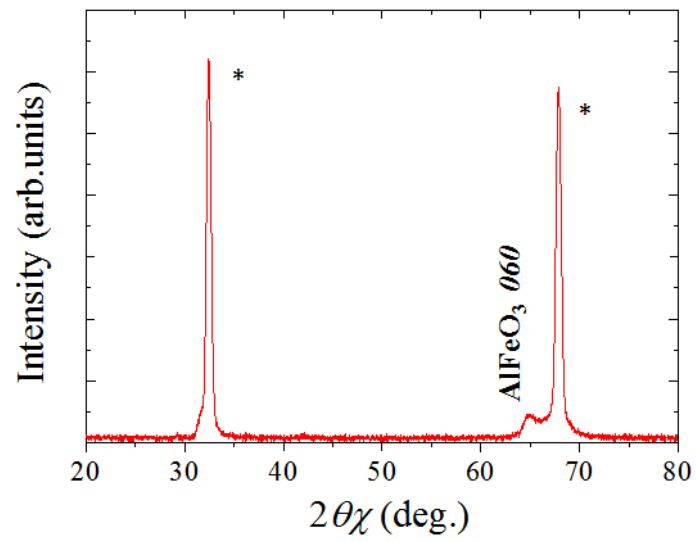


Figure 3-7 ϕ - $2\theta_{\chi}$ pattern of AlFeO₃ film along SrTiO₃[11-2] with 2θ angle of 20-80°. * correspond to the peaks of substrates.

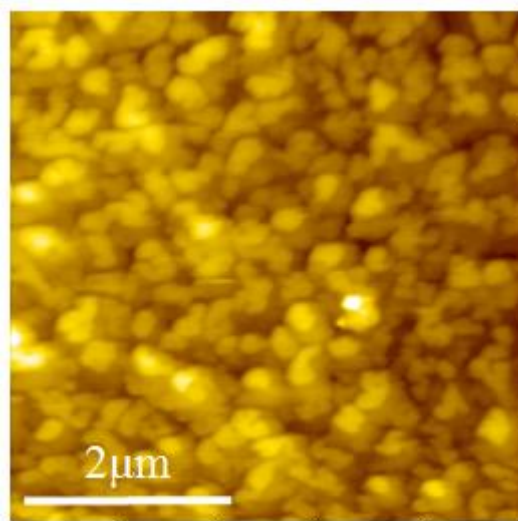


Figure 3-8 AFM image of AlFeO₃ film.

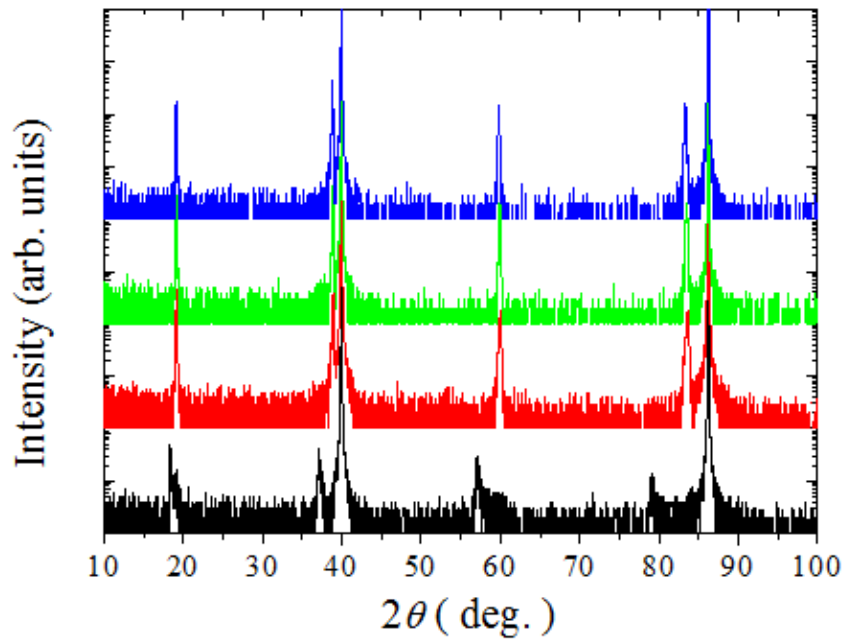


Figure 3-9 XRD θ - 2θ pattern of AlFeO_3 film deposited at 800°C under various oxygen pressure with 2θ angle of 10 - 100° .

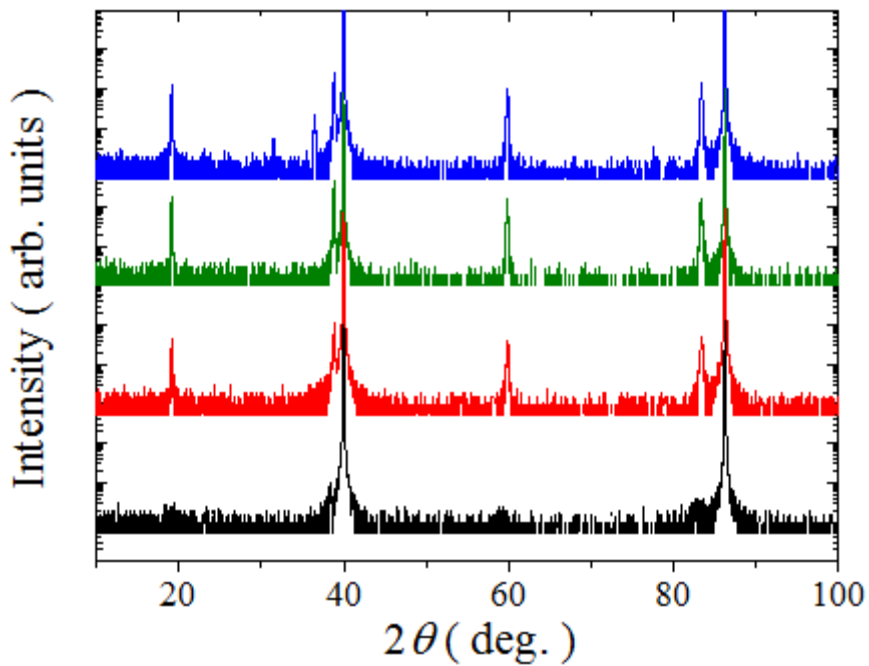


Figure 3-10 XRD θ - 2θ pattern of AlFeO_3 film deposited at various temperature under 100mTorr with 2θ angle of 10 - 100° .

P_{O_2} (mTorr)	20	50	100
FWHM (deg.)	0.301	0.196	0.135

Table 3-1 FWHM values of $AlFeO_3$ film deposited at $800^\circ C$ under various oxygen pressure.

Substrate Temperature ($^\circ C$)	700	800
FWHM (deg.)	0.204	0.135

Table 3-2 FWHM values of $AlFeO_3$ film deposited at various temperature under 100mTorr.

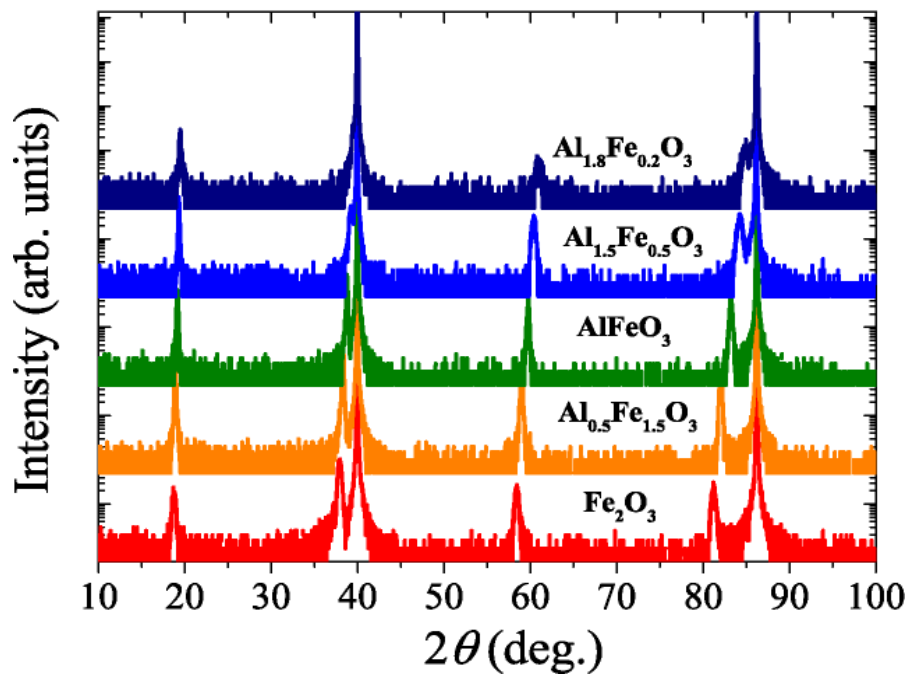


Figure 3-11 XRD θ - 2θ pattern of $Al_xFe_{2-x}O_3$ films ($x = 0-1.8$) deposited on $SrTiO_3(111)$ substrate.

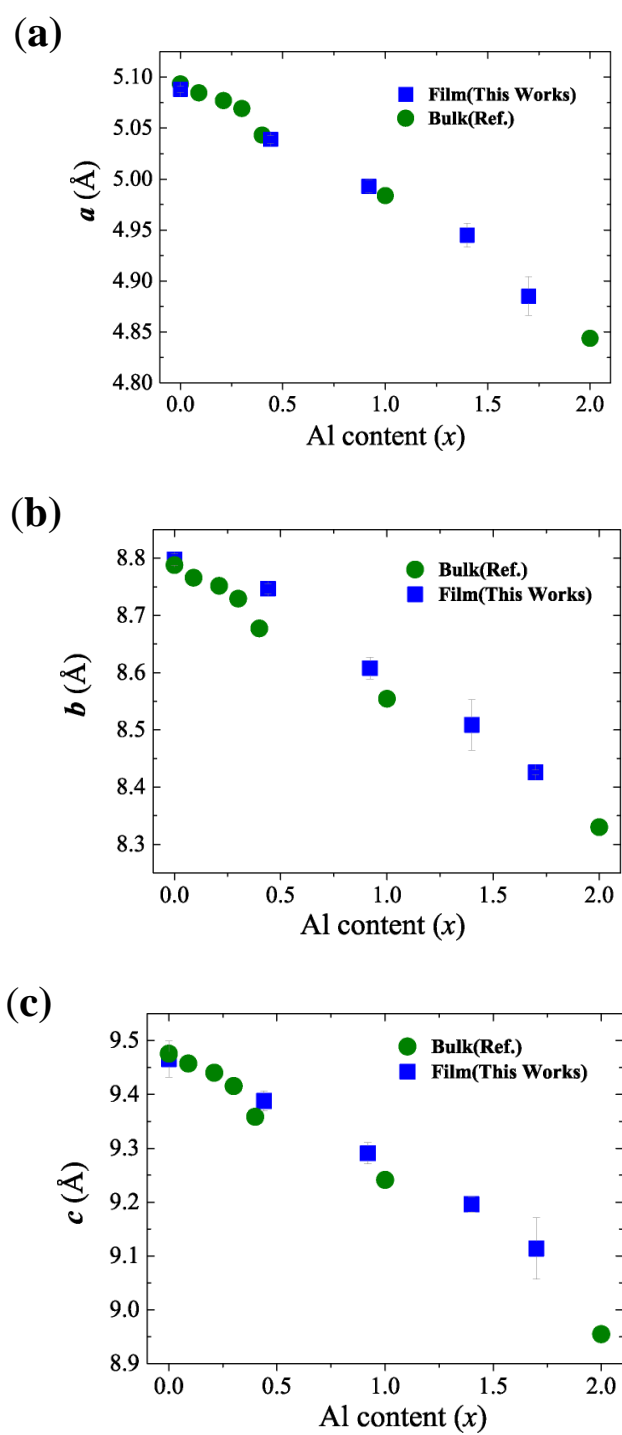


Figure 3-12 Lattice parameter of GaFeO₃-type Al_xFe_{2-x}O₃ films ($x = 0-1.8$) and κ -Al₂O₃-type Al_xFe_{2-x}O₃ powder samples (Ref. [3], [9]–[11]).

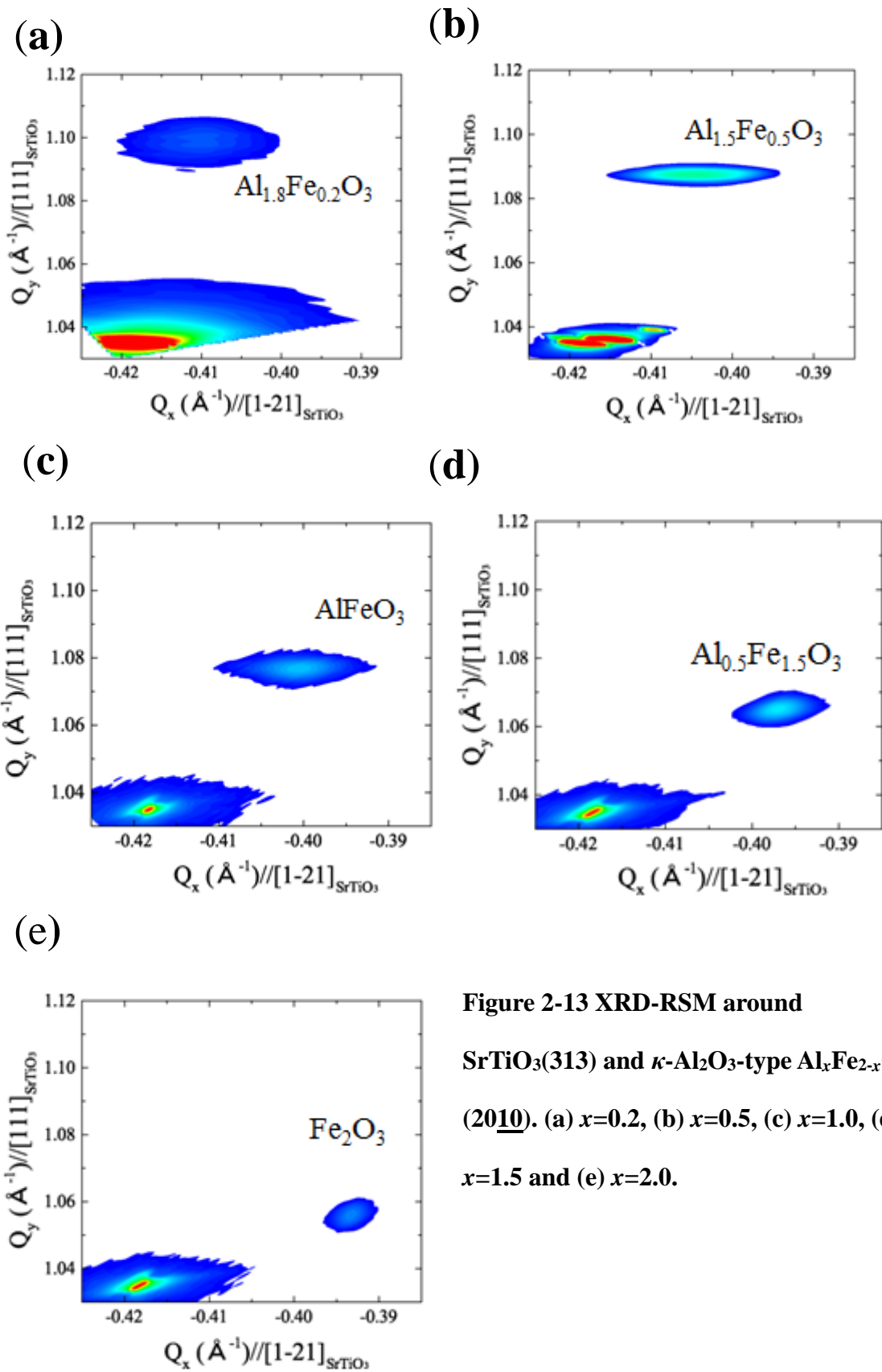


Figure 2-13 XRD-RSM around $SrTiO_3(313)$ and $\kappa-Al_2O_3$ -type $Al_xFe_{2-x}O_3$ (2010). (a) $x=0.2$, (b) $x=0.5$, (c) $x=1.0$, (d) $x=1.5$ and (e) $x=2.0$.

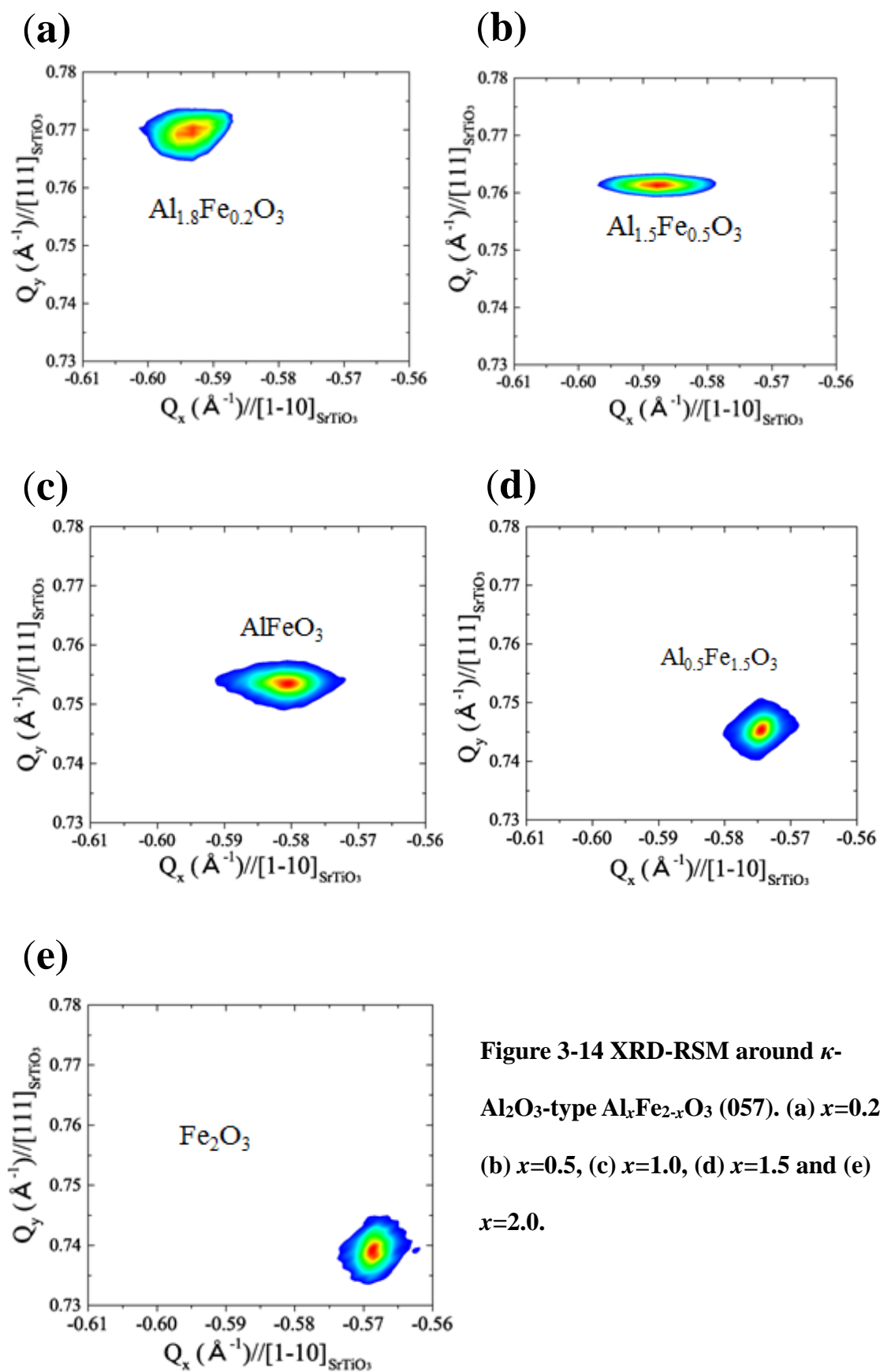


Figure 3-14 XRD-RSM around κ - Al_2O_3 -type $Al_xFe_{2-x}O_3$ (057). (a) $x=0.2$, (b) $x=0.5$, (c) $x=1.0$, (d) $x=1.5$ and (e) $x=2.0$.

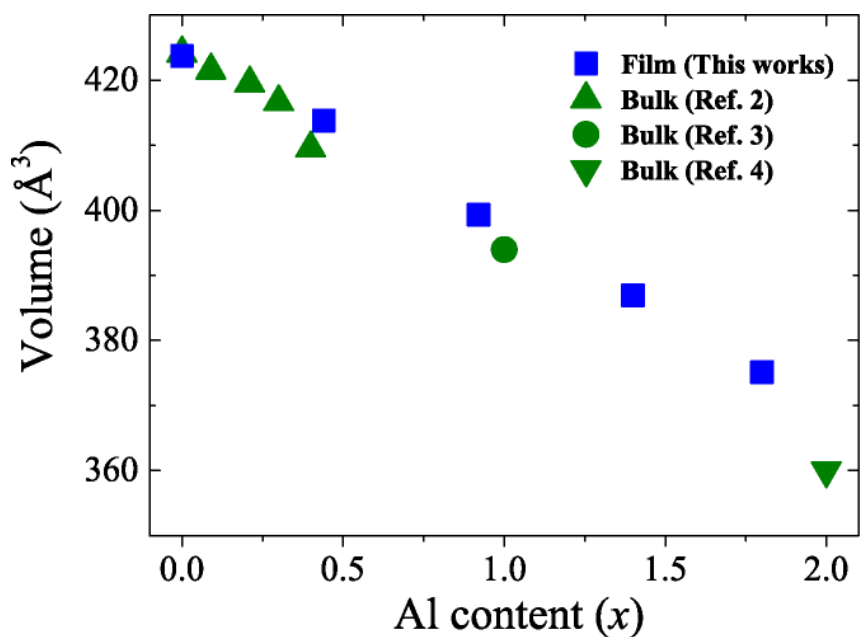


Figure 3-15 Lattice parameter of κ -Al₂O₃-type Al_xFe_{2-x}O₃ films ($x = 0$ -1.8)

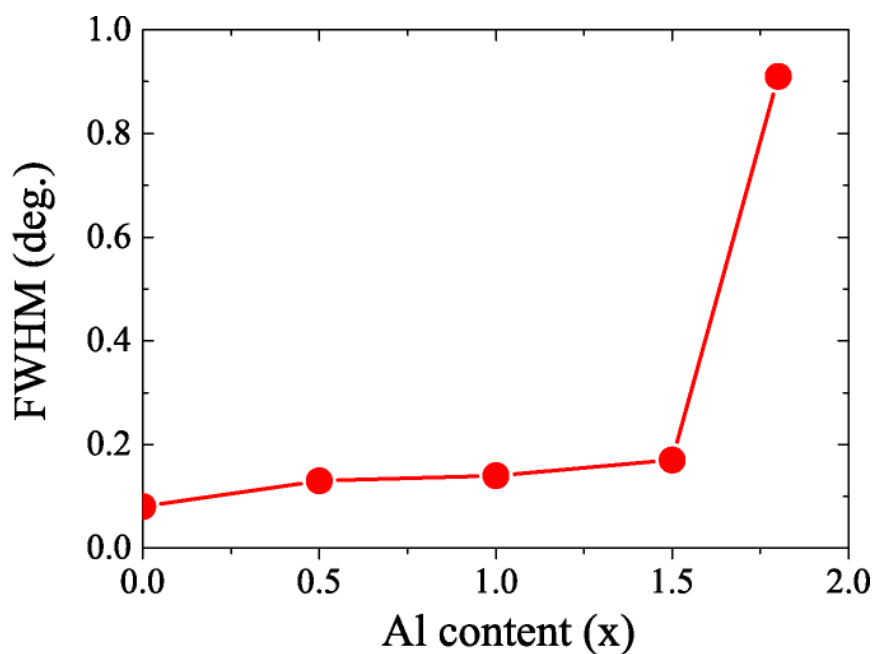


Figure 3-16 FWHM values of κ -Al₂O₃-type Al_xFe_{2-x}O₃ films ($x = 0$ -1.8)

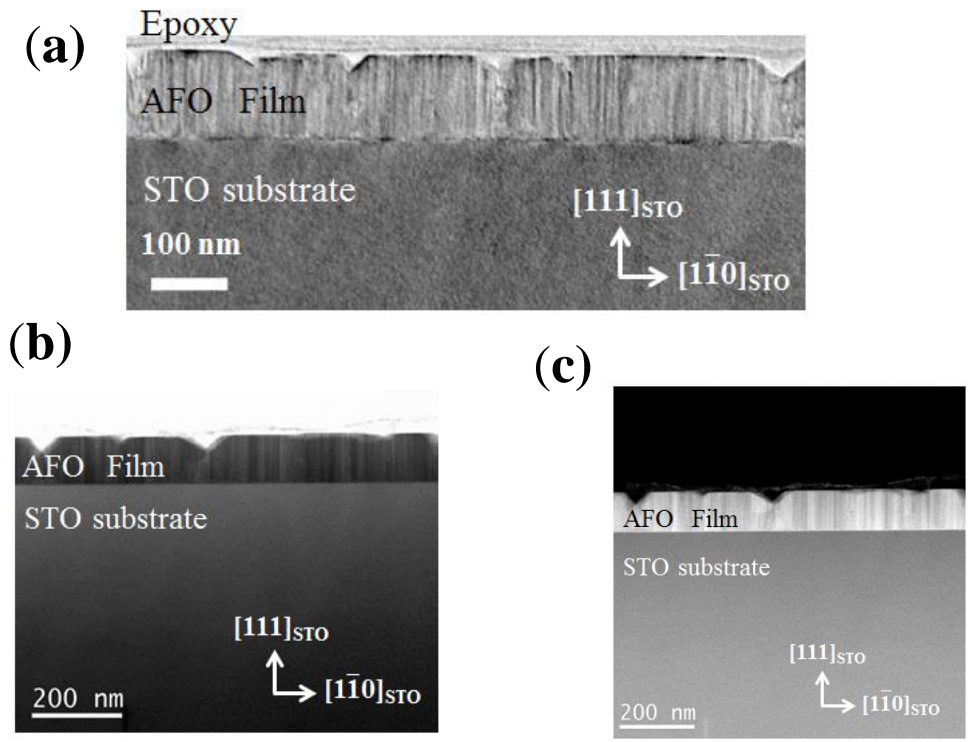


Figure 3-19 TEM and STEM image of AlFeO₃ film. (a) Bright field image (b) LAADF-STEM image (c) ABF-STEM image.

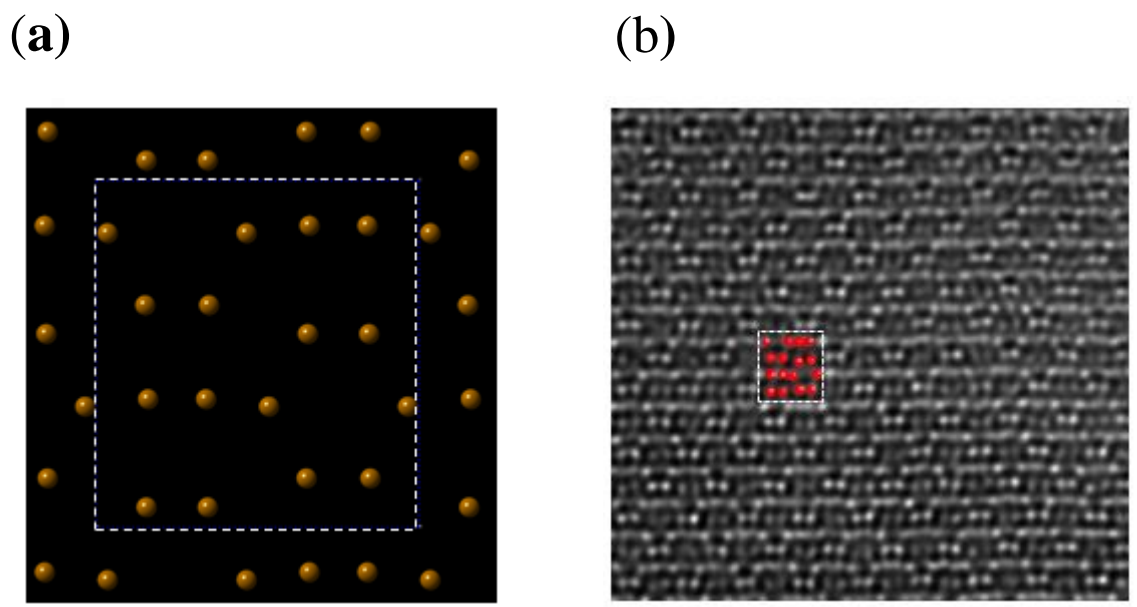


Figure 3-20 (a) Illustrates the atomic arrangement of cations along AlFeO₃[100] (b) Atomic-resolution HAADF-STEM image of κ -Al₂O₃-type AlFeO₃ film. White dot line corresponds to unite cell.

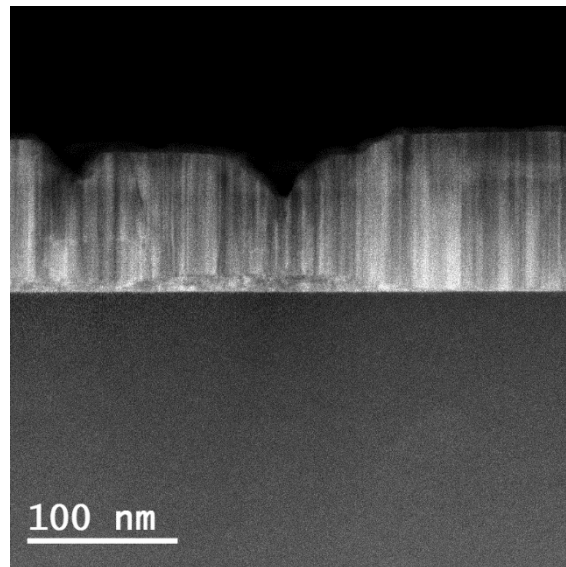


Figure 3-21 Magnified LAADF-STEM image around interface

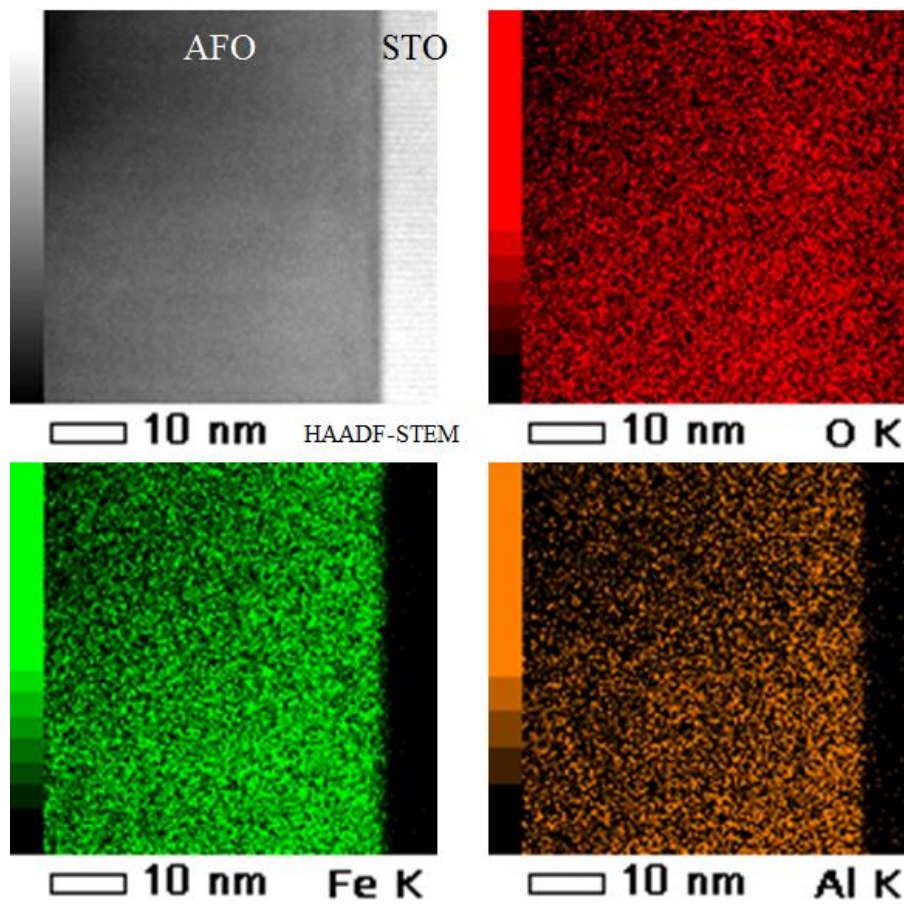


Figure 3-22 TEM-EDS analysis at interface between film and substrate.

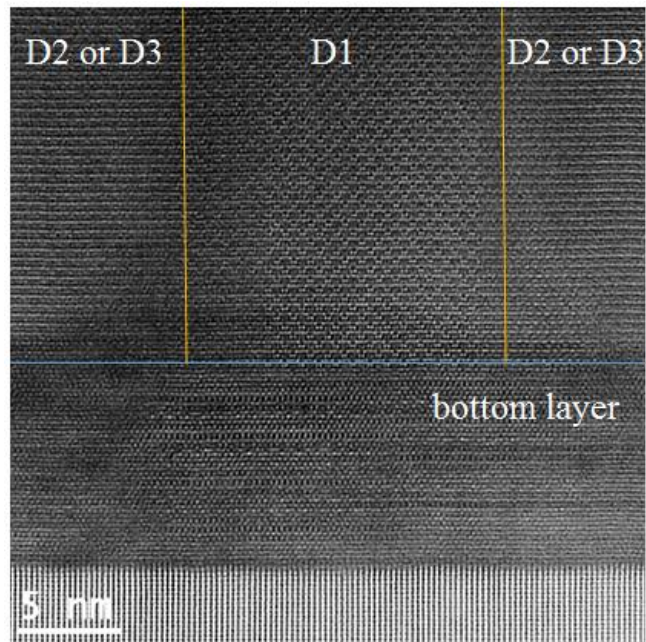


Figure 3-23 Magnified HAADF-STEM image. Blue line corresponds to a boundary between bottom layer and κ -Al₂O₃-type AlFeO₃ layer. Orange line corresponds to a boundary of three in-plane domains.

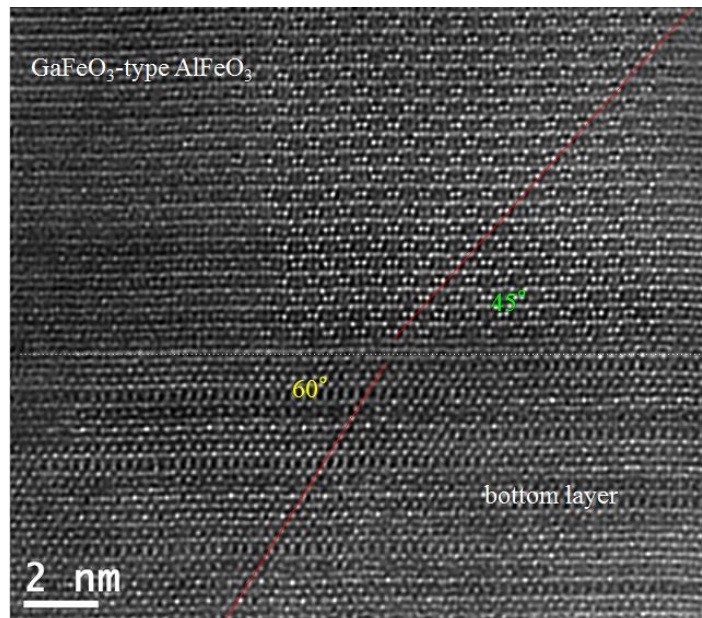


Figure 3-24 Magnified HAADF-STEM image around a boundary between bottom layer and κ -Al₂O₃-type AlFeO₃ layer

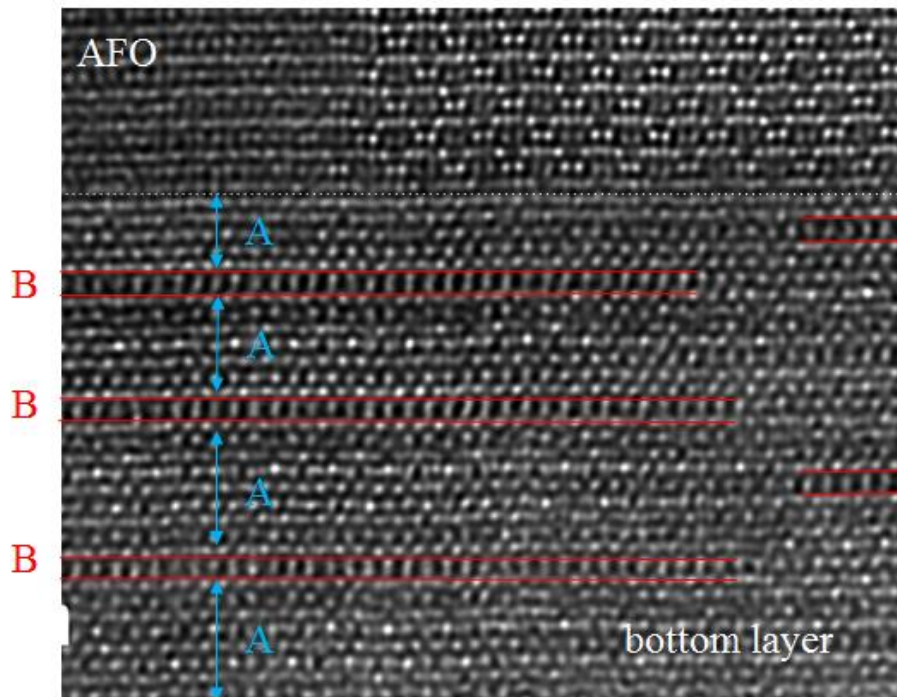


Figure 3-25 Atomic-resolution HAADF-STEM image of bottom layer.

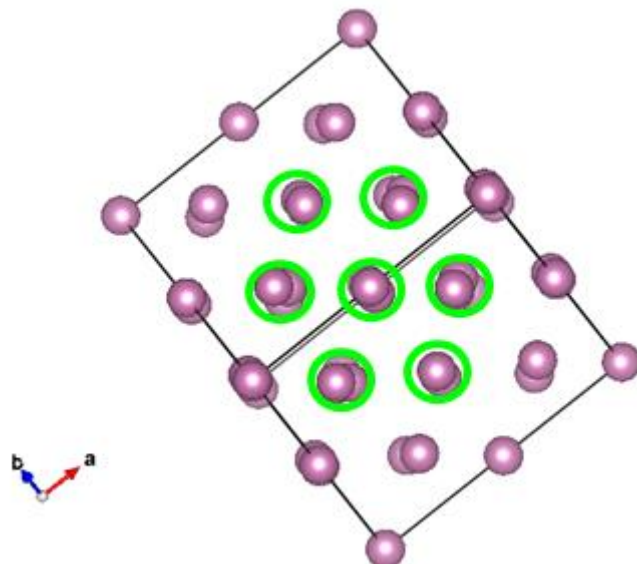


Figure 3-26 Cations arrangement of bixbyite structure.

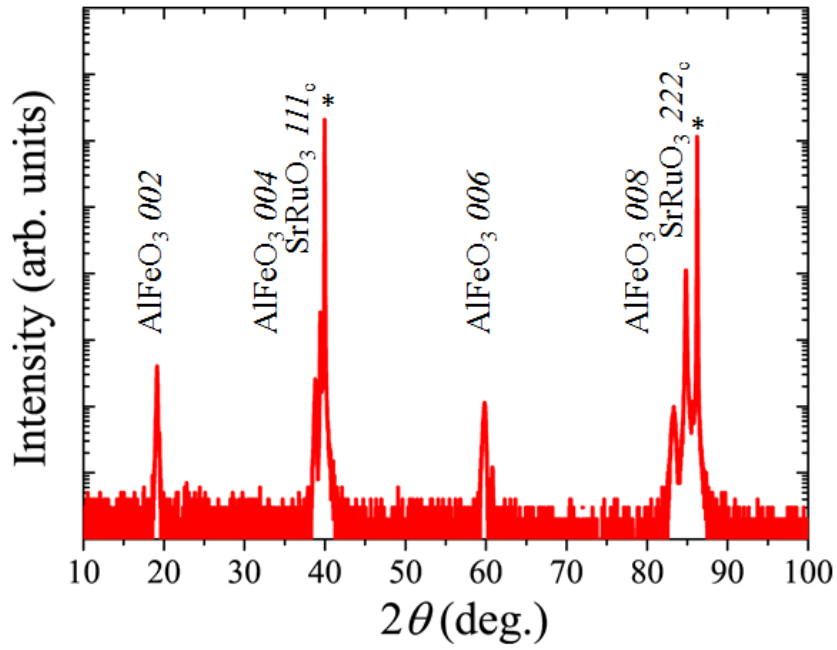


Figure 3-27 XRD θ - 2θ pattern of AlFeO_3 films on $\text{SrRuO}_3/\text{SrTiO}_3(111)$.

* corresponds to diffraction of substrates.

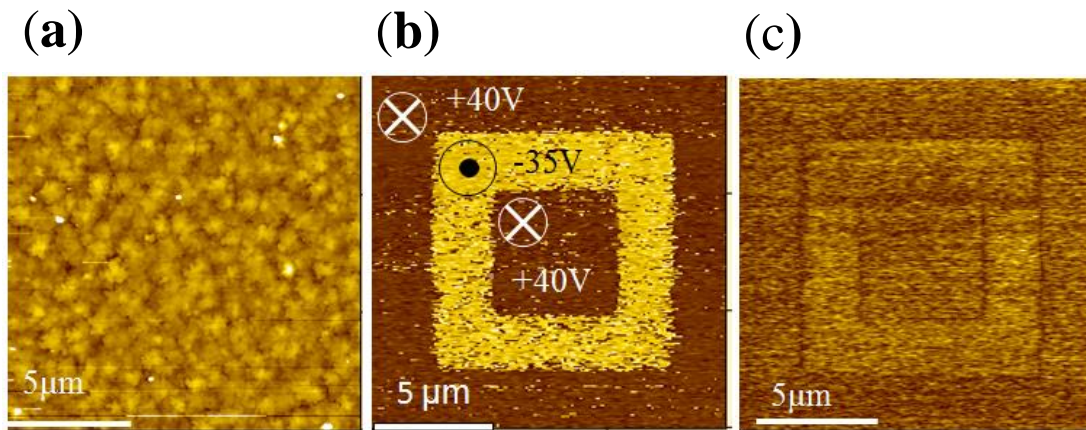


Figure 3-28 PFM image of AlFeO_3 films on $\text{SrRuO}_3/\text{SrTiO}_3(111)$. (a) surface morphology (b) phase image after poling (c) amplitude image after poling.

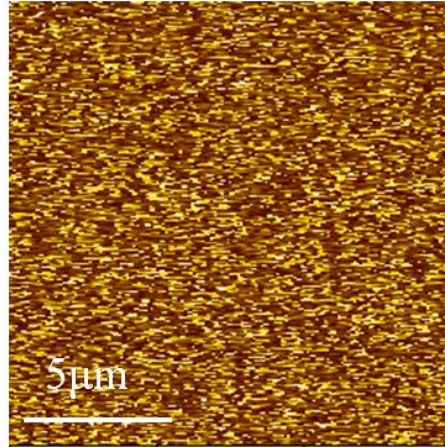


Figure 3-29 PFM image of AlFeO₃ films on SrRuO₃/SrTiO₃(111) before poling.

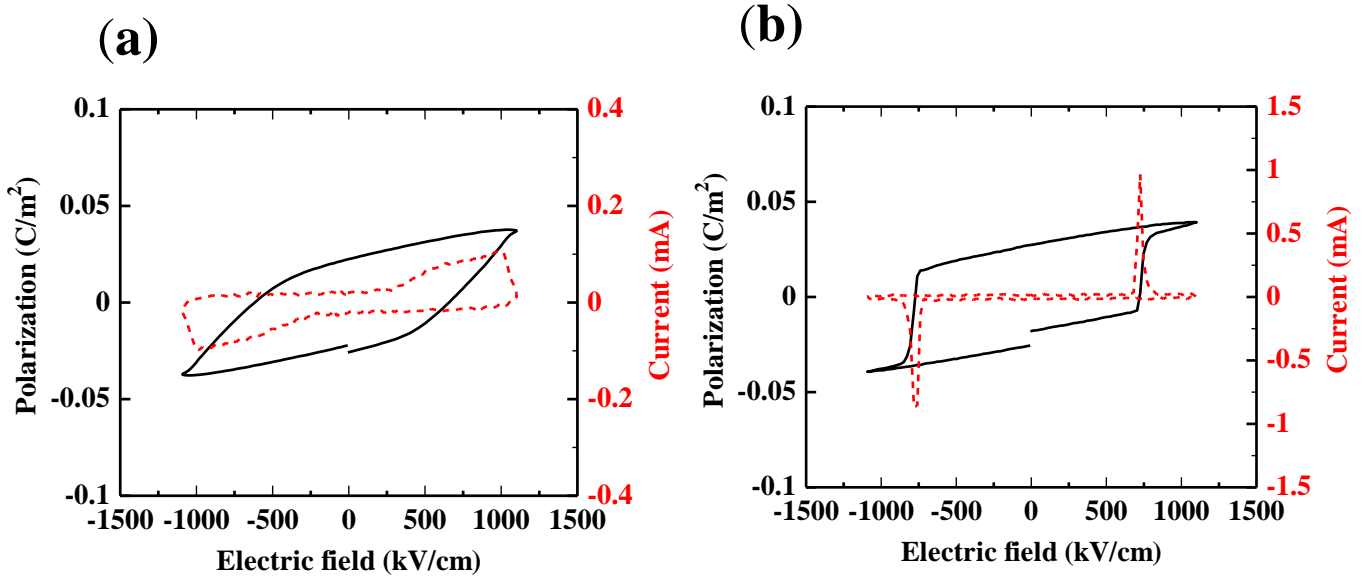


Figure 3-30 P-E hysteresis loops of AlFeO₃ film (a) and Al_{0.5}Fe_{1.5}O₃ film (b)

measured at 80 K and 30 kHz.

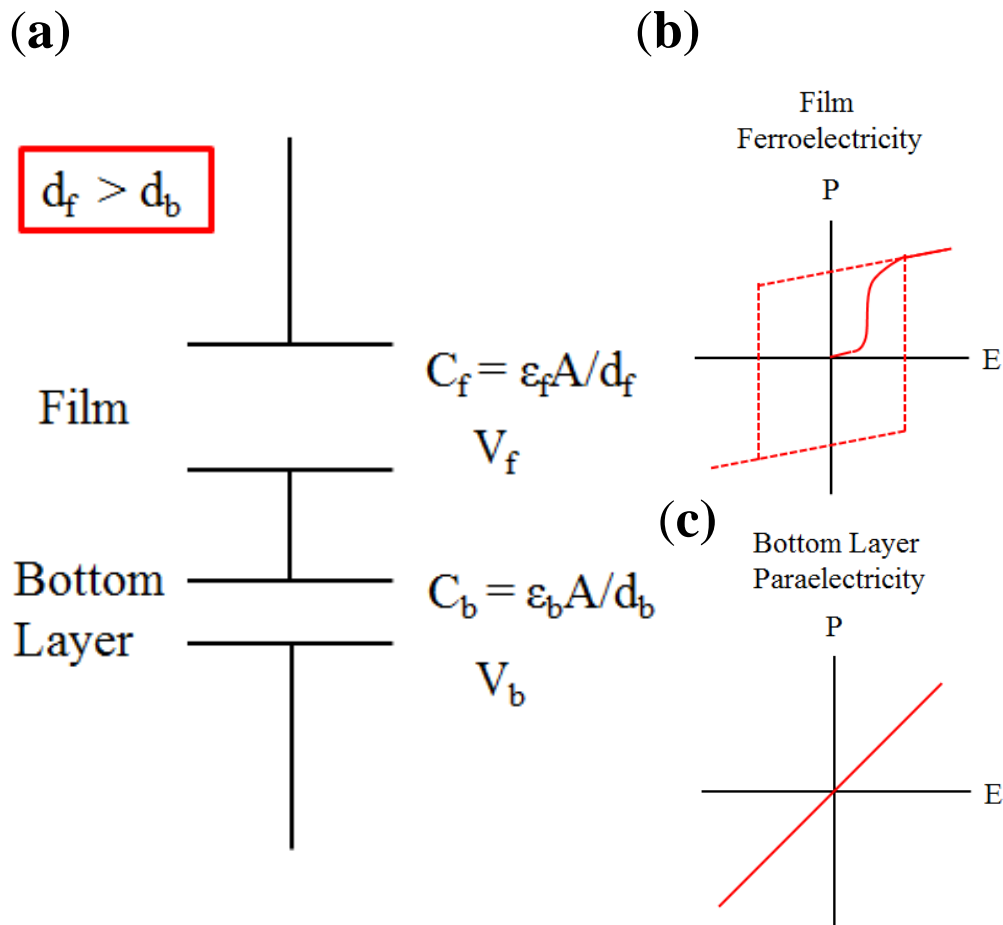


Figure 3-31 Schematic illustrate of the ideal circle for AlFeO_3 film (a), P - E loop of ferroelectric (b) and paraelectric (c) materials.

Reference

- [1] M. I. Pownceby, K. K. Constanti-Carey, and M. J. Fisher-White, "Subsolidus Phase Relationships in the System Fe_2O_3 - Al_2O_3 - TiO_2 between 1000°C and 1300°C," *J. Am. Ceram. Soc.*, vol. 86, no. 6, pp. 975–980, Jun. 2003.
- [2] R. R. Dayal, J. a. Gard, and F. P. Glasser, "Crystal data on FeAlO_3 ," *Acta Crystallogr.*, vol. 18, no. 3, pp. 574–575, Mar. 1965.
- [3] B. Ollivier, R. Retoux, P. Lacorre, D. Massiot, and G. Ferey, "Crystal structure of kappa-alumina: An X-ray powder diffraction, TEM and NMR study," *J. Mater. Chem.*, vol. 7, no. 431484, pp. 1049–1056, 1997.
- [4] E. Tronc, C. Chanéac, and J. P. Jolivet, "Structural and Magnetic Characterization of ϵ - Fe_2O_3 ," *J. Solid State Chem.*, vol. 139, no. 1, pp. 93–104, 1998.
- [5] I. Levin and D. Brandon, "Metastable Alumina Polymorphs: Crystal Structures and Transition Sequences," *J. Am. Ceram. Soc.*, vol. 81, no. 8, pp. 1995–2012, Jan. 1998.
- [6] S. Sakurai, A. Namai, K. Hashimoto, and S.-I. Ohkoshi, "First observation of phase transformation of all four Fe_2O_3 phases (gamma --> epsilon --> beta --> alpha-phase).," *J. Am. Chem. Soc.*, vol. 131, no. 51, pp. 18299–18303, 2009.
- [7] M. Gich, J. Gazquez, a. Roig, a. Crespi, J. Fontcuberta, J. C. Idrobo, S. J. Pennycook, M. Varela, and V. Skumryev, "Epitaxial stabilization of ϵ - Fe_2O_3 (001) thin films on SrTiO_3 (111)," *Appl. Phys. Lett.*, vol. 96, no. 11, p. 112508, 2010.
- [8] S. H. Oh, J. H. Lee, R. H. Shin, Y. Shin, C. Meny, and W. Jo, "Room-temperature polarization switching and antiferromagnetic coupling in epitaxial

- (Ga,Fe)₂O₃/SrRuO₃ heterostructures,” *Appl. Phys. Lett.*, vol. 106, no. 14, p. 142902, 2015.
- [9] F. Bouree, J. L. Baudour, E. Elbadraoui, J. Musso, C. Laurent, and a. Rousset, “Crystal and magnetic structure of piezoelectric, ferrimagnetic and magnetoelectric aluminium iron oxide FeAlO₃ from neutron powder diffraction,” *Acta Crystallogr. Sect. B Struct. Sci.*, vol. 52, no. 2, pp. 217–222, Apr. 1996.
- [10] S. Sakurai, J. Jin, K. Hashimoto, and S. Ohkoshi, “Reorientation Phenomenon in a Magnetic Phase of ε-Fe₂O₃ Nanocrystal,” *J. Phys. Soc. Japan*, vol. 74, no. 7, pp. 1946–1949, Jul. 2005.
- [11] A. Namai, S. Sakurai, M. Nakajima, T. Suemoto, K. Matsumoto, M. Goto, S. Sasaki, and S. I. Ohkoshi, “Synthesis of an electromagnetic wave absorber for high-speed wireless communication,” *J. Am. Chem. Soc.*, vol. 131, no. 3, pp. 1170–1173, 2009.

Phase Equilibria Diagrams Online Database (NIST Standard Reference Database 31), The American Ceramics Society and the National Institute of Standards and Technology, 2015. Figure 3-1; www.nist.gov/srd/nist31.cfm.

Chapter 4

Sc₂O₃-Fe₂O₃ System

4.1 Introduction

In chapter 3, we prepared κ -Al₂O₃-type Al_xFe_{2-x}O₃ films and studied the ferroelectricity in Al_xFe_{2-x}O₃ film. Ferroelectric hysteresis loop of Al_xFe_{2-x}O₃ film could not be obtained at room temperature because of leakage currents. In chapter 4, we focused on Sc. Since Sc³⁺ cation is stable, Sc substitution prevents the leakage currents. Moreover, according to *ab initio* calculation by Konishi the activation energy of Sc₂O₃ for polarization switching is smaller than that of Al₂O₃ (see Appendix). Therefore, the ferroelectric hysteresis loop of κ -Al₂O₃-type Sc_xFe_{2-x}O₃ may be obtained at room temperature.

Until now, κ -Al₂O₃-type Sc_xFe_{2-x}O₃ have not been reported. When the ionic radius of Me^{3+} is that of Fe³⁺ (0.645 Å) and more, κ -Al₂O₃-type Me^{3+} FeO₃ compounds cannot be obtained by a conventional solid reaction (Figure 4-1)[1]. κ -Al₂O₃-type Me^{3+} FeO₃ compounds ($Me^{3+} = \text{Fe, Rh and In}$) is prepared by combining reverse micelle and sol-gel techniques[2]–[4]. The particle diameter is important key to stabilize κ -Al₂O₃-type Me FeO₃ compound[5]. In this chapter, we attempted to stabilize κ -Al₂O₃-type Sc_xFe_{2-x}O₃ by PLD and investigated the ferroelectricity and magnetism in κ -Al₂O₃-type Sc_xFe_{2-x}O₃.

4.2 Experiment

Sc_xFe_{2-x}O₃ films were grown on SrTiO₃(111) single-crystal substrates by PLD technique. A fourth-harmonic wave of a Nd: YAG laser ($\lambda = 266$ nm) was used. A repetition rate and a fluence of a Nd: YAG laser are 5Hz and 2.4, respectively. The target was prepared by mixing Sc₂O₃ and α -Fe₂O₃ powder and sintering at 1450°C for 14 hours in air. Chemical composition of targets are ScFeO₃, Sc_{0.5}Fe_{1.5}O₃ and Fe₂O₃. The

crystal structure of films were investigated by high-resolution X-ray diffraction (XRD) using a Rigaku Smart-Lab diffractometer. X-ray was monochromatized using a Ge(220) 2-bounce crystal and Cu $K\alpha$ radiation ($\lambda=1.5406 \text{ \AA}$) was used. The Reciprocal space mapping (RSM) was measured to estimate to lattice constants. High temperature XRD (HTXRD) was measured using a Rigaku Smart-Lab diffractometer with an Anton Paar hot stage. The detail of $\text{Sc}_x\text{Fe}_{2-x}\text{O}_3$ films were characterized by HAADF-STEM. HAADF-STEM image was carried out on the JEOL ARM-200F operated at 200kV. Sample for TEM was prepared by a focused ion beam (FIB) method. P-E hysteresis loop was measured by ferroelectric tester (Toyo Corporation, FCE) Pt as top electrode was deposited by the electric beam evaporation method. The field-cooled (FC) dc magnetization was measured in a Quantum Design MPMS. The FC magnetization was recorded at 500 Oe and 10-350 K.

4.3 Result and Discussion

4.3.1 Growth of $\text{Sc}_x\text{Fe}_{2-x}\text{O}_3$ Film

We prepared ScFeO_3 film at same deposited condition of AlFeO_3 , however $\kappa\text{-Al}_2\text{O}_3$ -type ScFeO_3 did not appear. As described at chapter 3, $\varepsilon\text{-Fe}_2\text{O}_3$ film on $\text{SrTiO}_3(111)$ was obtained only in a limited condition of the deposition. Following this, about 30nm $\text{Sc}_x\text{Fe}_{2-x}\text{O}_3$ films were deposited on $\text{SrTiO}_3(111)$ substrate under 100mTorr in O_2 . During the deposition, the substrate was kept at 600°C . A laser fluence of 0.96 J cm^{-2} was used. XRD 2θ - θ pattern of $\text{Sc}_x\text{Fe}_{2-x}\text{O}_3$ films were shown in Figure 4-2. As in the case of $\text{Al}_x\text{Fe}_{2-x}\text{O}_3$ films, four peaks without that of substrates were observed. These peaks were corresponded to $002l$ reflections of $\kappa\text{-Al}_2\text{O}_3$ -type structures. We have succeeded in stabilizing $\kappa\text{-Al}_2\text{O}_3$ -type $\text{Sc}_x\text{Fe}_{2-x}\text{O}_3$ on $\text{SrTiO}_3(111)$ substrate. The out of

plane orientation relationship is κ -Al₂O₃-type Sc_xFe_{2-x}O₃ (001) || SrTiO₃(111) without impurity phase. The thickness fringes were observed around *004* peaks, indicating that film surface is smooth. The full-width-at-half-maximum (FWHM) value of rocking curve was measured at *008* reflections. The FWHM value of Fe₂O₃, Sc_{0.5}Fe_{1.5}O₃ and ScFeO₃ were 0.081, 0.065 and 0.053°. These values are narrower than that of Al_xFe_{2-x}O₃ film, suggesting a well-crystallized and high quality film. In order to characterize in-plane relationship, phi scan was carried out around the ScFeO₃{201} and SrTiO₃{110} reflections as shown Figure 4-3. The scan at ScFeO₃{201} showed six-fold symmetry. This result consists with that of κ -Al₂O₃-type AlFeO₃ film on SrTiO₃(111) substrate. Therefore, the in-plane relationship between ScFeO₃ film and SrTiO₃ substrate can be described as ScFeO₃[100] || SrTiO₃[11-2], || SrTiO₃[1-21] and || SrTiO₃[-211], respectively (see Figure 3-4). RSM were measured around Sc_xFe_{2-x}O₃ *2010* and SrTiO₃ *313* reflections (Figure 4-4). It seems that there are no lattice strain in Sc_xFe_{2-x}O₃ film on SrTiO₃ substrate. RSM were also measured around Sc_xFe_{2-x}O₃ *507* reflection. The lattice constants were estimated from XRD results and summarized in figure 4-5(a)-(c). The **a**, **b** and **c** lattice constants increase with increasing Sc contents. Figure 4-6 shows the unite cell volume of Sc_xFe_{2-x}O₃ films. It is apparent that the unite cell volume of Sc_xFe_{2-x}O₃ films monotonically increase with increasing Sc content. This is consistent with the fact that ionic radius of Sc (0.745 Å (VI)) is larger than that of Fe (0.645 Å (VI)) and indicates that Sc₂O₃ is solid-soluted into a κ -Al₂O₃-type Fe₂O₃.

In order to investigate the thermal stability of Sc_xFe_{2-x}O₃ films, HTXRD was carried out. Figure 4-7(a) shows XRD 2θ - θ patterns around κ -Al₂O₃-type Sc_{0.5}Fe_{1.5}O₃ *004* and SrTiO₃ *111* in the temperature range 100-1000°C. The lattice constants of Sc_{0.5}Fe_{1.5}O₃ film and SrTiO₃ substrate is summarized in Figure 4-7 (b) as a function of temperature

on heating. From 100-800°C, the lattice constant of $\text{Sc}_{0.5}\text{Fe}_{1.5}\text{O}_3$ film monotonically increased. At 850°C, the peak position of $\text{Sc}_{0.5}\text{Fe}_{1.5}\text{O}_3$ film greatly shifted to a high angle, i.e. a phase transition. The high temperature phase could be corundum phase. Because $\kappa\text{-Al}_2\text{O}_3$ -type structure is polar, this phase transition may be ferroelectric phase transition. However, the phase transition was not observed on cooling. From these results, this phase transition is not ferroelectric phase transition but irreversible. This irreversible phase transition is observed in Al_2O_3 ($\kappa \rightarrow \alpha$ at 900-1000°C)[6]. Figure 4-8 (a)-(c) shows XRD 2θ - θ patterns around $\kappa\text{-Al}_2\text{O}_3$ -type Fe_2O_3 004 and SrTiO_3 111 in the temperature range 100-1000°C. In the case of $\kappa\text{-Al}_2\text{O}_3$ -type Fe_2O_3 film, the corundum phase appeared at 850°C, however the corundum phase coexists with $\kappa\text{-Al}_2\text{O}_3$ -type phase above 850°C. After cooling, the mixing phase is kept (Figure 4-8 (c)). Therefore, HTXRD results indicate that both $\kappa\text{-Al}_2\text{O}_3$ -type $\text{Sc}_{0.5}\text{Fe}_{1.5}\text{O}_3$ and Fe_2O_3 films are stable below 850°C, and ferroelectric phase transition was not observed in both these films.

4.3.2 Investigation of Interface by TEM

Crystal structure of ScFeO_3 film was also characterized by TEM. Figure 4-9 shows the HAADF-STEM image of ScFeO_3 film on $\text{SrTiO}_3(111)$ substrate in cross section view along $\text{SrTiO}_3[11-2]$. In the images, 100 nm grains were observed as in the case of AlFeO_3 film. Figure 4-10(a)-(c) illustrates the magnified HAADF-STEM image. In figure 4-10(a), the two or four atoms group are in each layer and these layers stack along the out of plane. The green and blue atoms pair correspond to tetrahedral and octahedral coordinate cation sites, respectively. The purple atoms correspond to octahedral site (Figure 4-10 (b)). These results clearly indicate that ScFeO_3 film on $\text{SrTiO}_3(111)$ substrate have $\kappa\text{-Al}_2\text{O}_3$ -type structure. Figure 4-10(c) displays a HAADF-

STEM image around interface. In the grain, in-plane domains with about 20 nm were observed. At interface, the bottom layer was observed. Thickness of bottom layer is not uniform and is 2-20 nm.

It is found that crystal structure of the bottom layer is different from that of AlFeO_3 and there are no stacking faults (Figure 4-11 (a)). $\kappa\text{-Al}_2\text{O}_3$ -type ScFeO_3 film was grown reflecting atomic arrangement from SrTiO_3 substrates. The crystal structure of bottom layer is similar to $\kappa\text{-Al}_2\text{O}_3$ -type structure and should be based on $\kappa\text{-Al}_2\text{O}_3$ -type structure. The white square is considered as unit cell of the bottom layer. The bottom layer consists of the bright two (green spheres) and dark four (orange and red spheres) atoms groups, and dark four atoms are arranged in an arch shape (center-up-up-center or center-down-down-center) (see Figure 4-11 (b)). The four atoms group are opposite to another one along out of plane, indicating that the bottom layer is nonpolar. In-plane position of these atoms groups in bottom layer are same as that in $\kappa\text{-Al}_2\text{O}_3$ -type structure. Considering the $\kappa\text{-Al}_2\text{O}_3$ -type structure, two atoms which are up or down position in dark four atoms group (red spheres) could be the tetrahedral cation sites, whereas the others could be the octahedral cation sites (Figure 4-11 (c)).

The HAADF-STEM measurement revealed that the bottom layer is observed in ScFeO_3 film and crystal structure of bottom layer is greatly different from that of bottom layer in AlFeO_3 film.

4.3.3 Dielectric Property

Top and bottom electrode was Pt metal and $\text{SrTiO}_3\text{:Nb}$ substrate, respectively. Figure 4-12(a) illustrates frequency dependence of the relative dielectric constant and the loss tangent in $\text{Sc}_{0.5}\text{Fe}_{1.5}\text{O}_3$ epitaxial film measure at room temperature. At low frequency,

the value of the relative dielectric constant is about 200 and the relative dielectric constant rapidly decreased above 1 kHz. This is the dielectric dispersion and the dielectric loss peak was observed. This dispersion is expressed by Debye model (Figure 4-12(b)). The permittivity of Debye type dispersion is given:

$$\varepsilon^*(\omega) = \varepsilon_\infty + \frac{\varepsilon_0 - \varepsilon_\infty}{1 + i\omega\tau}$$

where τ is the relaxation time, ε_0 and ε_∞ are the static and high-frequency permittivity, respectively, ω is angular frequency. The temperature dependence of the relative dielectric constant and loss tangent are shown in figure 4-13(a) and (b), respectively. The loss tangent peaks shift to low frequency with decreasing temperature and the dispersion disappear at 200 K. The temperature dependence of the relative dielectric constant and loss tangent are plotted for each frequency in figure 4-14(a) and (b), respectively. As be seen in figure 4-14(a), the relative dielectric constant shows a steplike increases, which shifts to high temperature with increasing frequency. In figure 4-14(b), the loss tangent peaks shift to high temperature with increasing the frequency. This dielectric dispersion is often observed in iron oxides[7], [8]. Therefore, this dielectric dispersion can be considered to be a typical hopping conduction of localized charge carries. The activation energy was estimated by an Arrhenius relation:

$$\tau = \tau_0 \exp\left(\frac{E_a}{k_B T}\right)$$

where E_a is the activation energy for relaxation, k_B is the Boltzmann constant and T is the absolute temperature. We plotted the estimated relaxation time as function of the inverse temperature (Figure 4-15). The estimated activation energy is 0.205 eV and this value is close to that of GaFeO₃ single crystal ($E_a = 0.233$ eV)[9]. The activation energy of the carrier hopping process between Fe²⁺ and Fe³⁺ in Y₃Fe₅O₁₂ and LuFe₂O₄ are 0.29

eV[7], [8]. Therefore, this dispersion is can be the contribution of the valence fluctuation of iron ions.

4.3.4 *P-E* hysteresis loop

The ferroelectricity in κ -Al₂O₃-type Sc_xFe_{2-x}O₃ films were investigated by electric polarization versus electric field (*P-E*) hysteresis loop. The electric field was applied along the out of plane, which is parallel to the direction of spontaneous polarization in κ -Al₂O₃-type Sc_xFe_{2-x}O₃. Top and bottom electrodes are Pt metal and SrTiO₃: Nb substrate, respectively. In order to prevent leakage currents, substrate temperature cooled for 1 hour in 100Torr O₂ after the deposition. The leakage current densities (*J*) of Sc_{0.5}Fe_{1.5}O₃ film was measured at room temperature (Figure 4-16). The leakage current densities of Sc_{0.5}Fe_{1.5}O₃ film is below 10⁻³ A/cm² at 4V. *P-E* hysteresis loop of Sc_xFe_{2-x}O₃ film was measured at room temperature. Figure 4-17 and 4-18 show *P-E* hysteresis loops of epitaxial ScFeO₃ and Sc_{0.5}Fe_{1.5}O₃ films at various frequency. The saturated ferroelectric hysteresis loop was observed in Sc_{0.5}Fe_{1.5}O₃ film. In contrast, *P-E* loop of ScFeO₃ film shows leaky behavior. The minor loop was observed above 50 kHz, because the coercive field become large at high frequency. In Sc_{0.5}Fe_{1.5}O₃ film, the hysteresis loop shows soft ferroelectric behavior at low frequency and hard ferroelectric behavior at high frequency. The ferroelectricity in Sc_{0.5}Fe_{1.5}O₃ film strongly depends on frequency.

In order to investigate the detail of ferroelectricity in Sc_{0.5}Fe_{1.5}O₃ film, we carried out some measurements. *P-E* hysteresis loop was measured at room temperature and the frequency of 1 kHz. As can be seen in Figure 4-19, Sc_{0.5}Fe_{1.5}O₃ film shows a strong switching loop characteristic of ferroelectric materials. The remnant polarization is

about $4 \mu\text{C}/\text{cm}^2$. This value is larger than that of $\text{Al}_{0.5}\text{Fe}_{1.5}\text{O}_3$ film. The reason for the smaller polarization compared with calculated value may be the influence of the bottom layer. The remnant polarization, maximum polarization and coercive field were plotted in Figure 4-20 and 4-21. The remnant polarization, maximum polarization and coercive field monotonically increased with increasing the applied voltage. The coercive field of $\text{Sc}_{0.5}\text{Fe}_{1.5}\text{O}_3$ film shows the saturated behavior at high voltage. We also measured P - E loop at various temperature and 1 kHz. The behavior of hysteresis loop change from soft to hard with decreasing temperature (Figure 4-22). Compared to the temperature dependence of dielectric properties (Figure 4-13 (a)) and hysteresis loops, it is found that the behavior of hysteresis loop change from soft to hard with freezing the dielectric dispersion. Therefore, the soft ferroelectric behavior might be infused by the dielectric dispersion at low frequency.

4.3.5 Magnetic property

Magnetic properties of κ - Al_2O_3 -type $\text{Sc}_x\text{Fe}_{2-x}\text{O}_3$ films were investigated by MPMS. The temperature dependence of magnetization in κ - Al_2O_3 -type $\text{Sc}_x\text{Fe}_{2-x}\text{O}_3$ films are shown in Figure 4-23(a), (b), (c). As can be seen in Figure 4-23 (a), magnetization of the κ - Al_2O_3 -type Fe_2O_3 film decreased below 157 K. This behavior is observed in κ - Al_2O_3 -type Fe_2O_3 (ε - Fe_2O_3) nanorods and corresponds to the phase transition from ferrimagnetism to incommensurate magnetic order ($T_p = 154$ K, where T_p is the phase transition temperature from ferrimagnetism to incommensurate magnetic order)[10]. The T_p value of the κ - Al_2O_3 -type Fe_2O_3 film is almost same as that of nanorods, consequently we also confirmed the κ - Al_2O_3 -type Fe_2O_3 film from the viewpoint of the magnetic property. The T_p value of κ - Al_2O_3 -type $\text{Sc}_{0.5}\text{Fe}_{1.5}\text{O}_3$ film is 189 K, which is

higher than that of κ -Al₂O₃-type Fe₂O₃ film (Figure 4-23(b)). This can be explained the site occupancy of Sc. The site occupancy of Me^{3+} in $Me^{3+}_xFe_{2-x}O_3$ is related to the ionic radius of Me^{3+} (r_{Me}). When $r_{Me} > r_{Fe}$, Me^{3+} dominantly occupies at octahedral site and the T_p value increases. When the ionic radius of $r_{Me} < r_{Fe}$, Me^{3+} dominantly occupies at tetrahedral site and the T_p value decrease[11]. This relationship is understand by the fact that the phase transition from ferrimagnetism to incommensurate magnetic order involves the change in the coordination of the tetrahedral site[10]. Since the ionic radius of Sc^{3+} is larger than that of Fe^{3+} , Sc^{3+} dominantly should occupies at octahedral site in κ -Al₂O₃-type $Sc_xFe_{2-x}O_3$, which suggests the expectation of increasing the T_p value with increasing Sc substitution. The experimental result in $Sc_{0.5}Fe_{1.5}O_3$ film consists with the expectation. In the case of $ScFeO_3$ film, the ferri-incomensurate magnetic phase transition disappeared (Figure 4-23 (c)). The reason may be that a certain amount of Sc occupies at tetrahedral site.

4.4 Summary

κ -Al₂O₃-type $Sc_xFe_{2-x}O_3$ films were epitaxially grown on SrTiO₃(111) substrates. XRD phi-scan and HAADF-STEM confirmed three in-plane domains with size of about 20nm. The lattice constants and unit cell volume of κ -Al₂O₃-type $Sc_xFe_{2-x}O_3$ films monotonically increase with increasing Sc contents. HAADF-STEM also revealed the bottom layer, which is completely different from that of AlFeO₃ film. The crystal structure of the bottom layer of $ScFeO_3$ film is similar to κ -Al₂O₃-type structure. The ferroelectric hysteresis loop was obtained at room temperature in $ScFeO_3$ film. The ferroelectric hysteresis loop show strongly frequency dependencies. From these results, Sc substitution in a κ -Al₂O₃-type Fe₂O₃ is effective to obtain ferroelectric hysteresis loop

at room temperature.

Figures

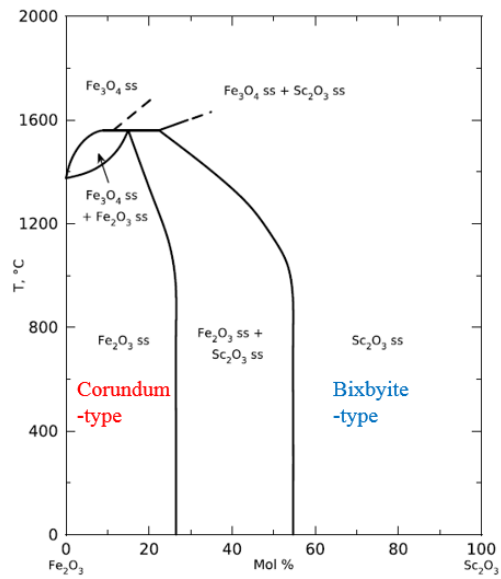


Figure 4-1 Sc₂O₃-Fe₂O₃ phase diagram, where ss is solid solution.

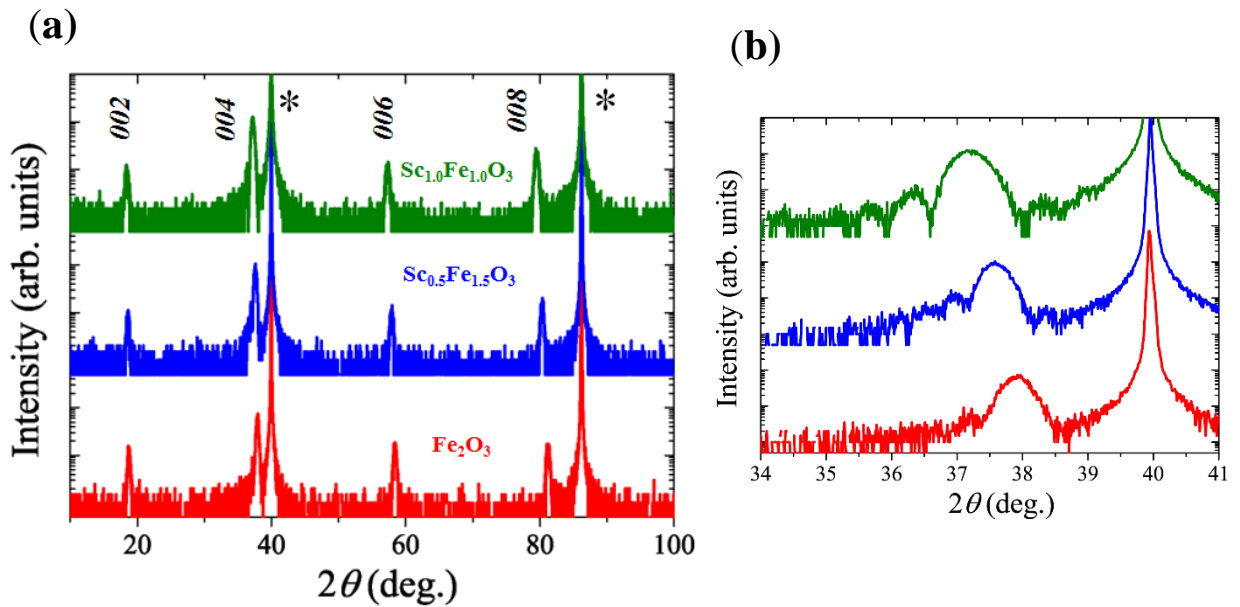


Figure 4-2 XRD θ - 2θ pattern of ScFeO₃, Sc_{0.5}Fe_{1.5}O₃ and Fe₂O₃ films with 2θ angle of 10-100° (a) and 34-41° (b). * correspond to the peaks of substrates.

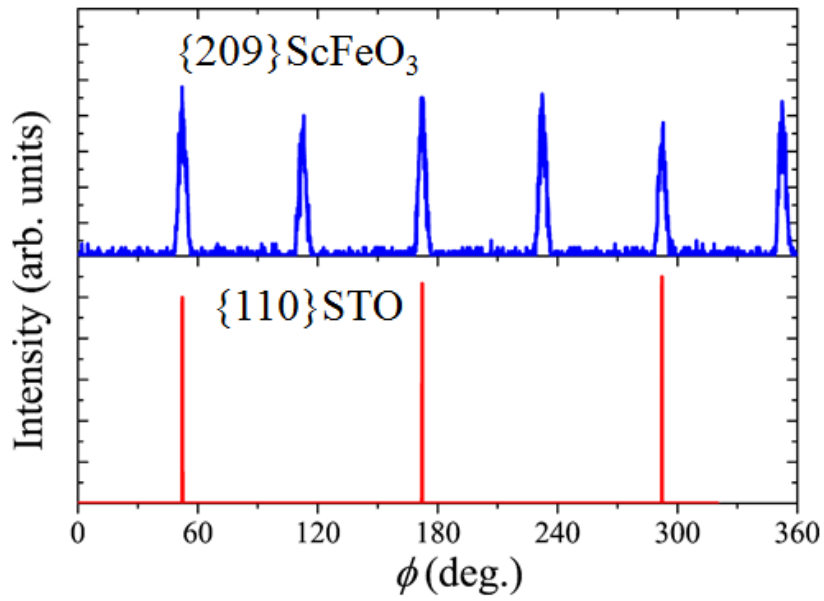


Figure 4-3 XRD ϕ -scan pattern of SrTiO₃ {110} and κ -Al₂O₃-type AlFeO₃ {209}.

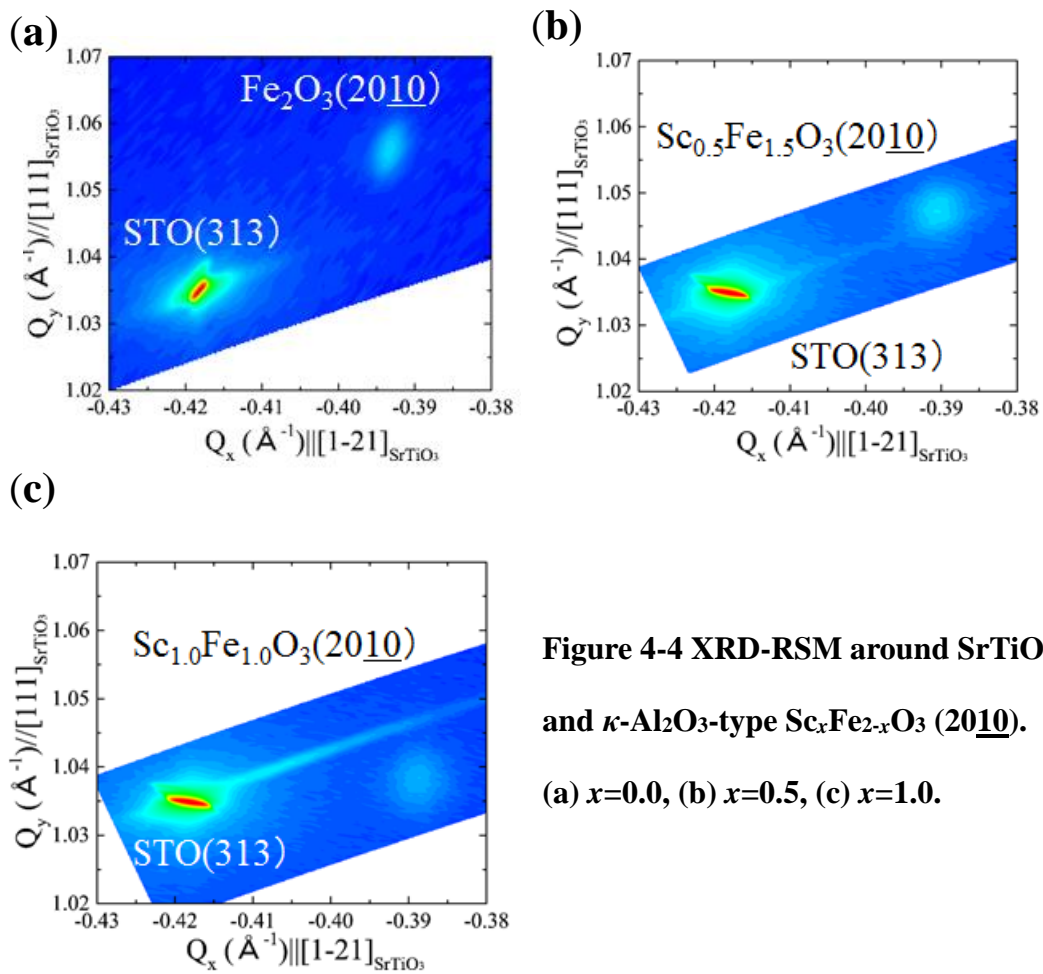


Figure 4-4 XRD-RSM around SrTiO₃(313)

and κ -Al₂O₃-type Sc_xFe_{2-x}O₃ (2010).

(a) $x=0.0$, (b) $x=0.5$, (c) $x=1.0$.

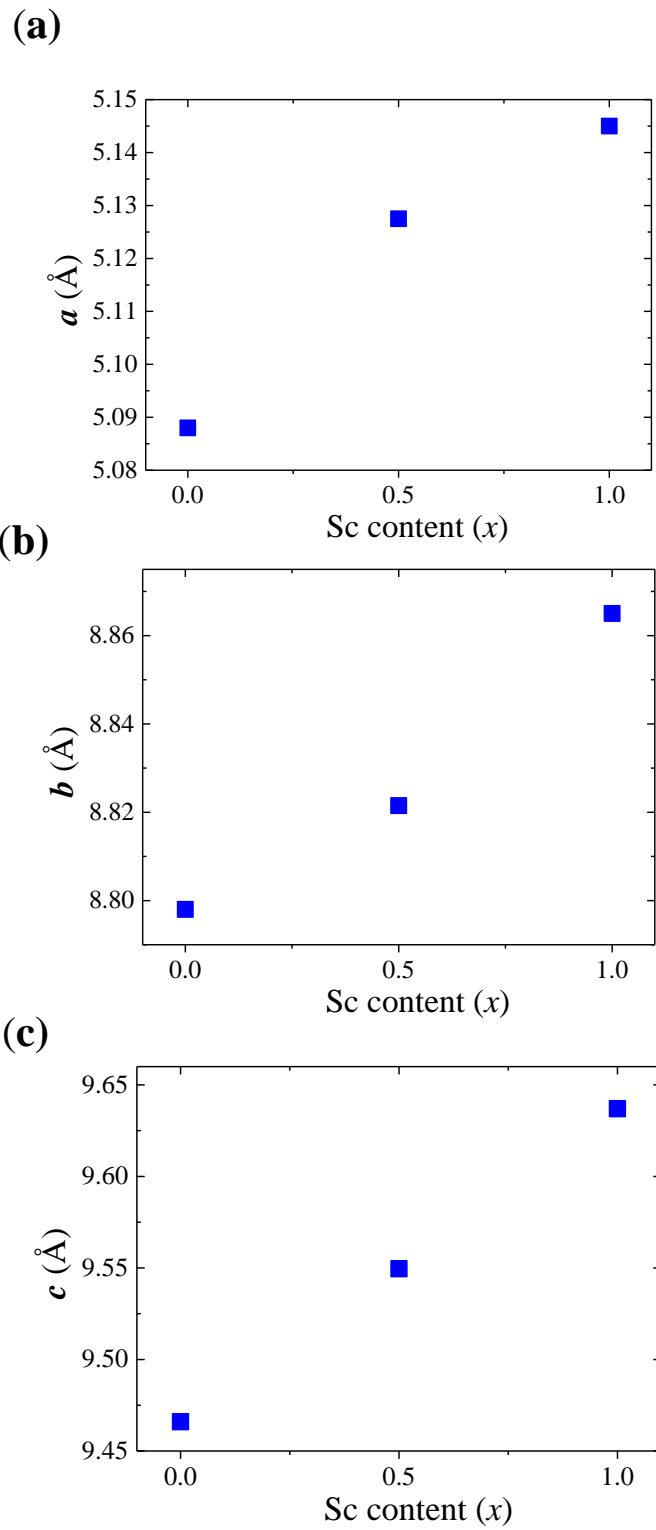


Figure 4-5 Lattice parameter of κ - Al_2O_3 -type $\text{Sc}_x\text{Fe}_{2-x}\text{O}_3$ films ($x = 0$ - 1.0).

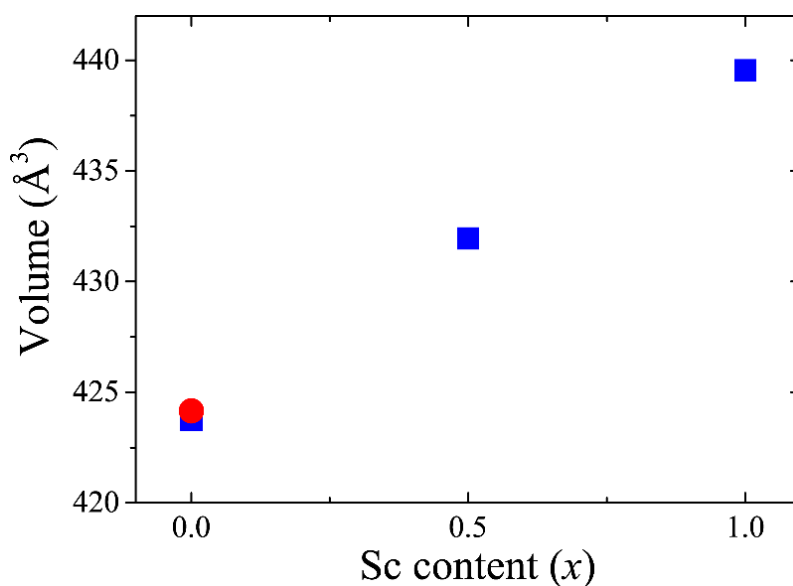


Figure 4-6 Unit cell volume of GaFeO₃-type Sc_xFe_{2-x}O₃ films (x = 0-1.0)

Blue square = Films, Red circle = ε-Fe₂O₃ nanorods.

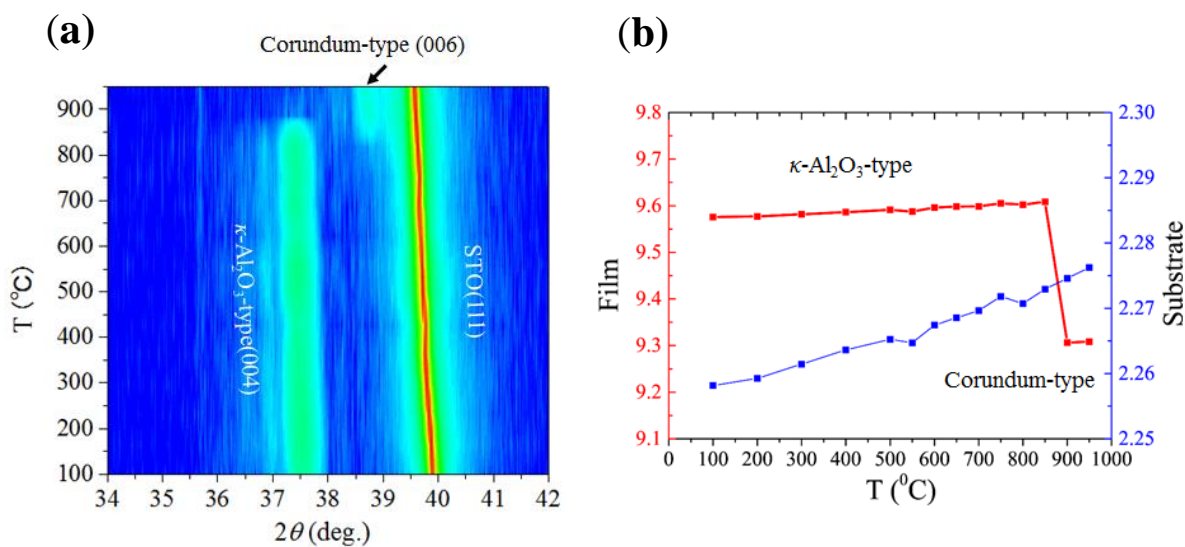


Figure 4-7 HTXRD pattern of κ -Al₂O₃-type Sc_{0.5}Fe_{1.5}O₃ films. Temperature dependence of θ - 2θ pattern (a) and lattice constants (b).

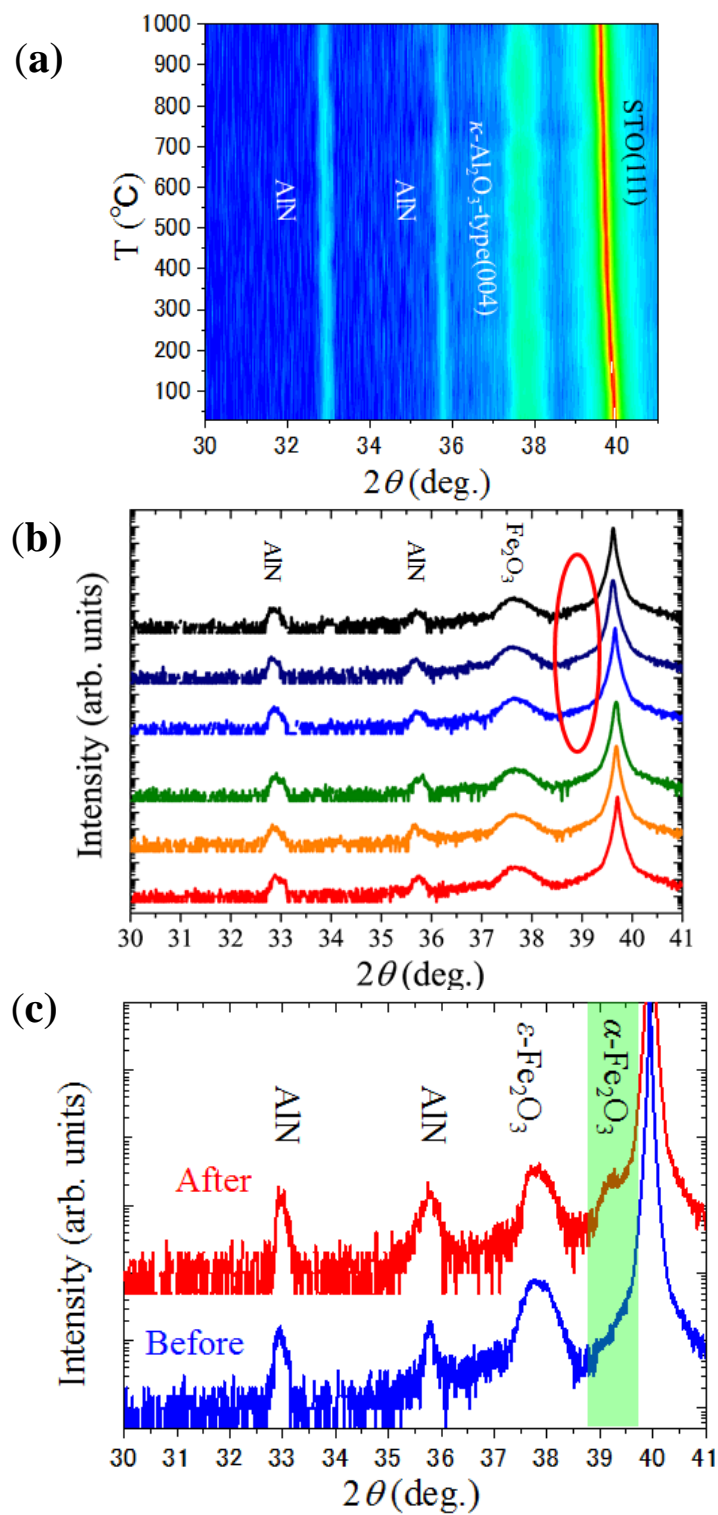


Figure 4-8 HTXRD pattern of κ - Al_2O_3 -type Fe_2O_3 films. Temperature dependence of θ - 2θ pattern at 100-1000 $^{\circ}\text{C}$ (a) and 700-1000 $^{\circ}\text{C}$ (b). XRD θ - 2θ pattern at room temperature before and after HTXRD measurements.

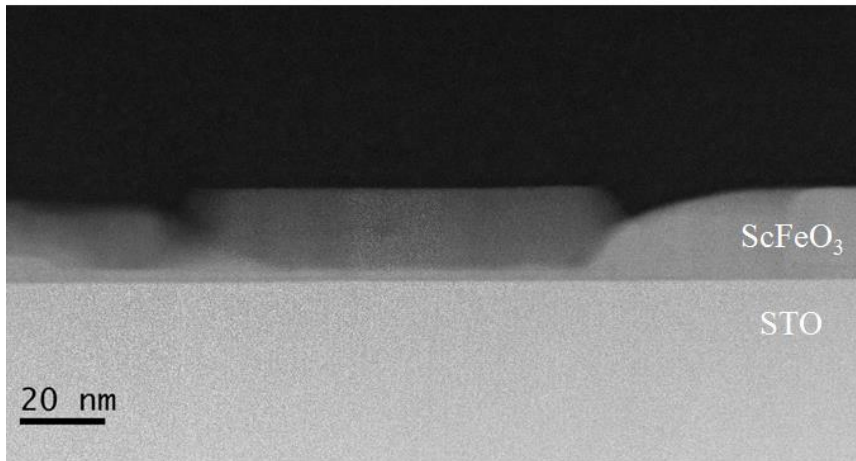


Figure 3-9 Cross-sectional HAADF image for the ScFeO₃ film.

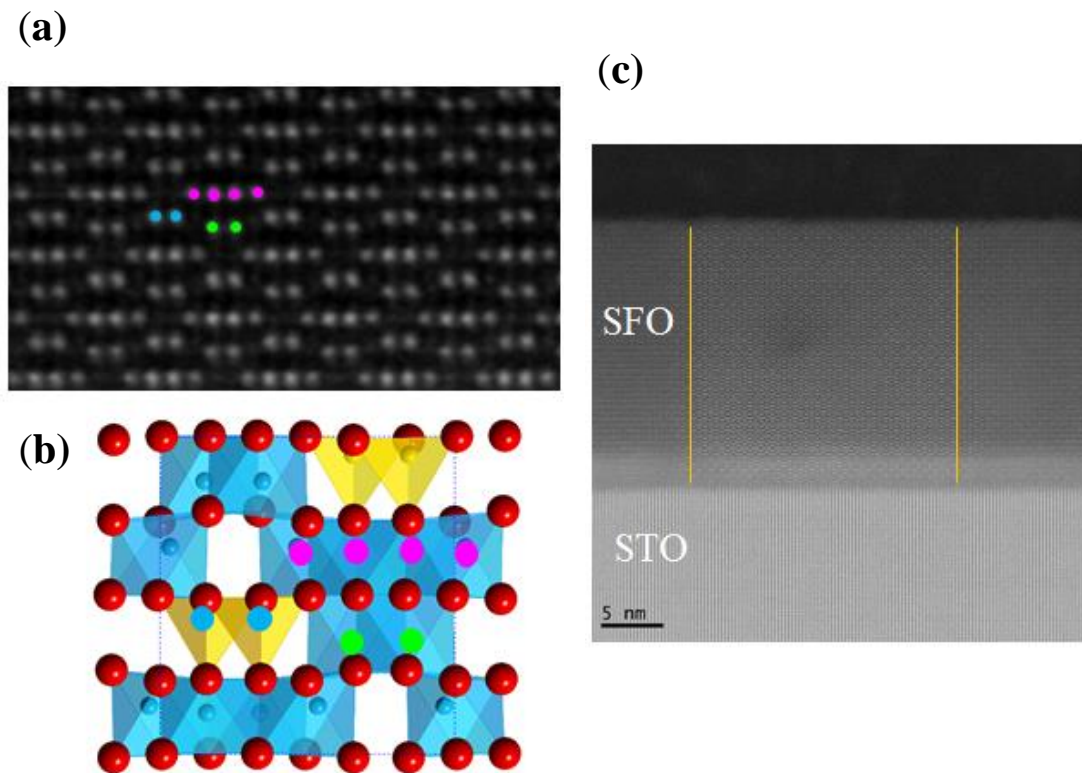
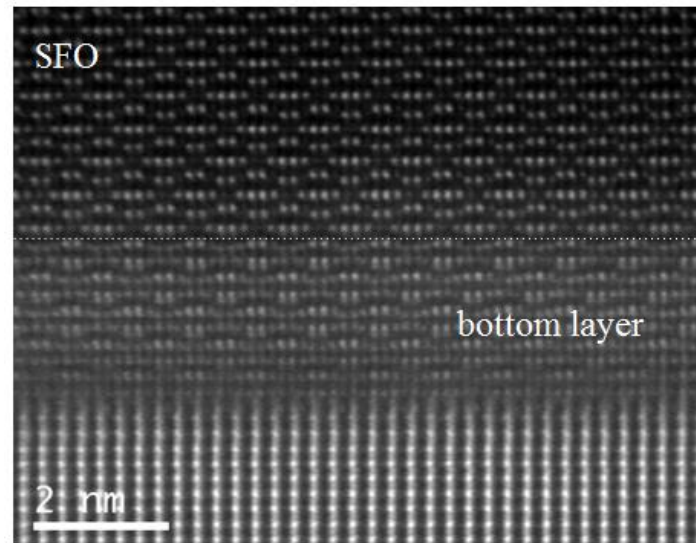
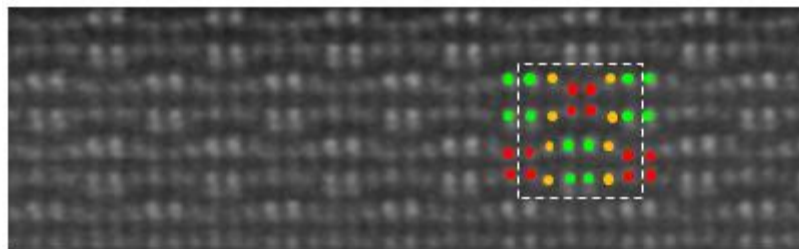


Figure 3-10 (a) Atomic-resolution HAADF image for the ScFeO₃ film. (b) Illustrates the atomic arrangement of cations in κ -Al₂O₃-type structure. (c) Cross-sectional HAADF image. Orange line corresponds to domain boundary.

(a)



(b)



(c)

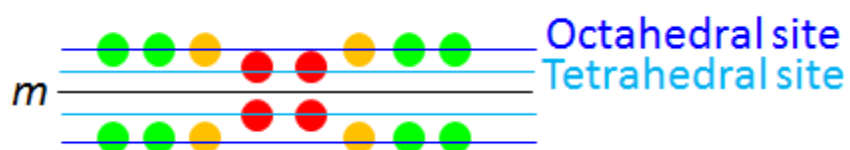


Figure 4-11 (a) Magnified HAADF image for the interface. (b) Atomic-resolution HAADF image for bottom layer. White line correspond to unite cell. (c) Illustrates the atomic arrangement of cations in bottom layer.

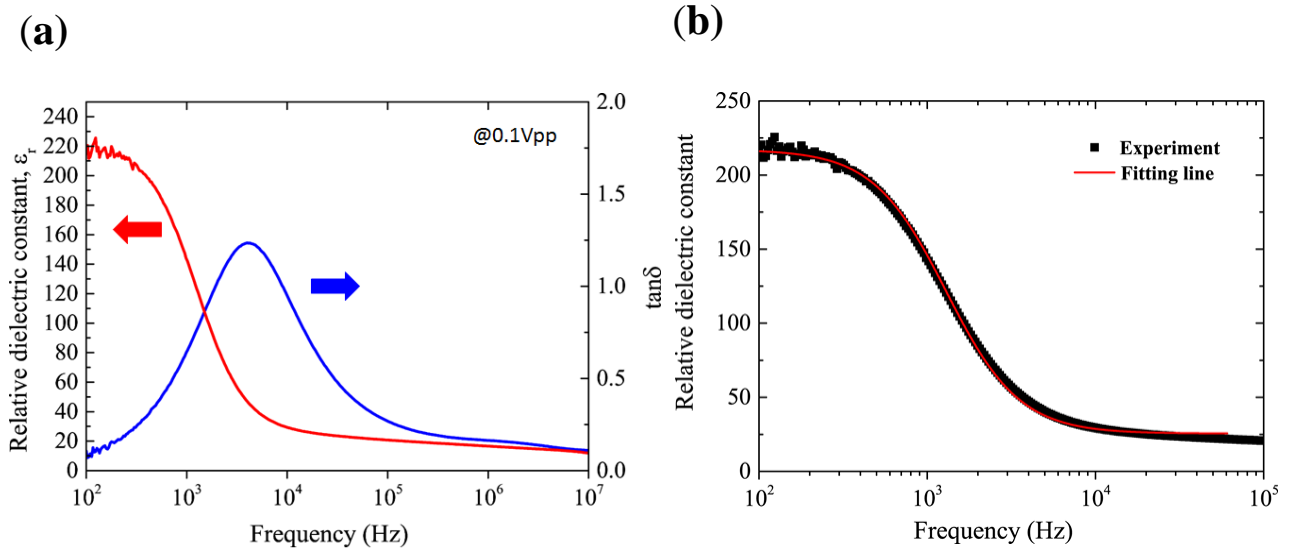


Figure 4-12 (a) Frequency dependence of relative dielectric constant and loss tangent in $\text{Sc}_{0.5}\text{Fe}_{1.5}\text{O}_3$ epitaxial film measured at room temperature. (b) Fitted relative dielectric constant. The solid red line corresponds to the fitting result.

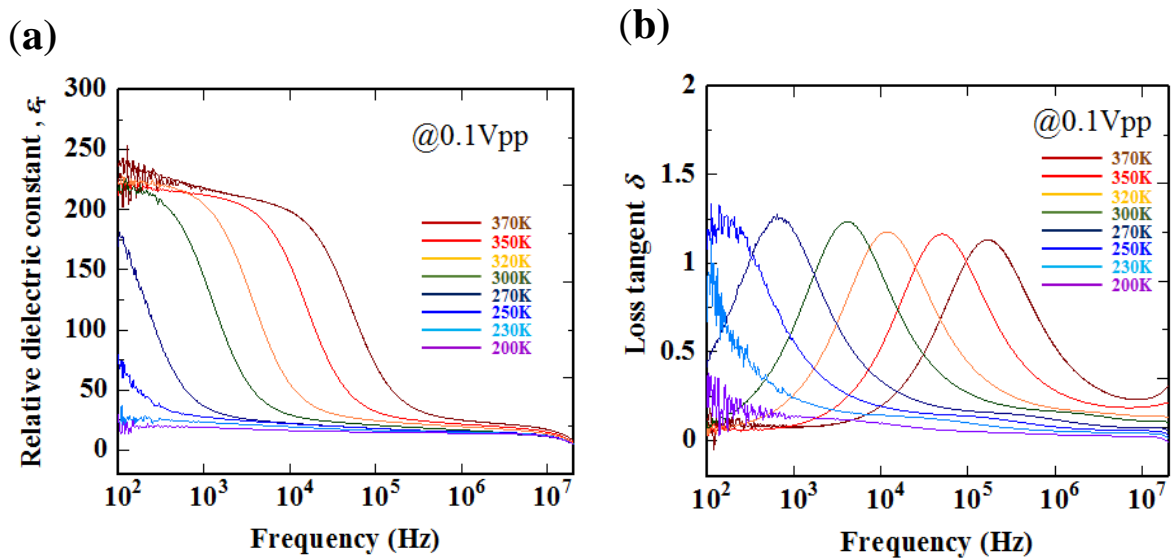


Figure 4-13 (a) Temperature dependence of relative dielectric constant for $\text{Sc}_{0.5}\text{Fe}_{1.5}\text{O}_3$ film (b) Temperature dependence of loss tangent for $\text{Sc}_{0.5}\text{Fe}_{1.5}\text{O}_3$ film

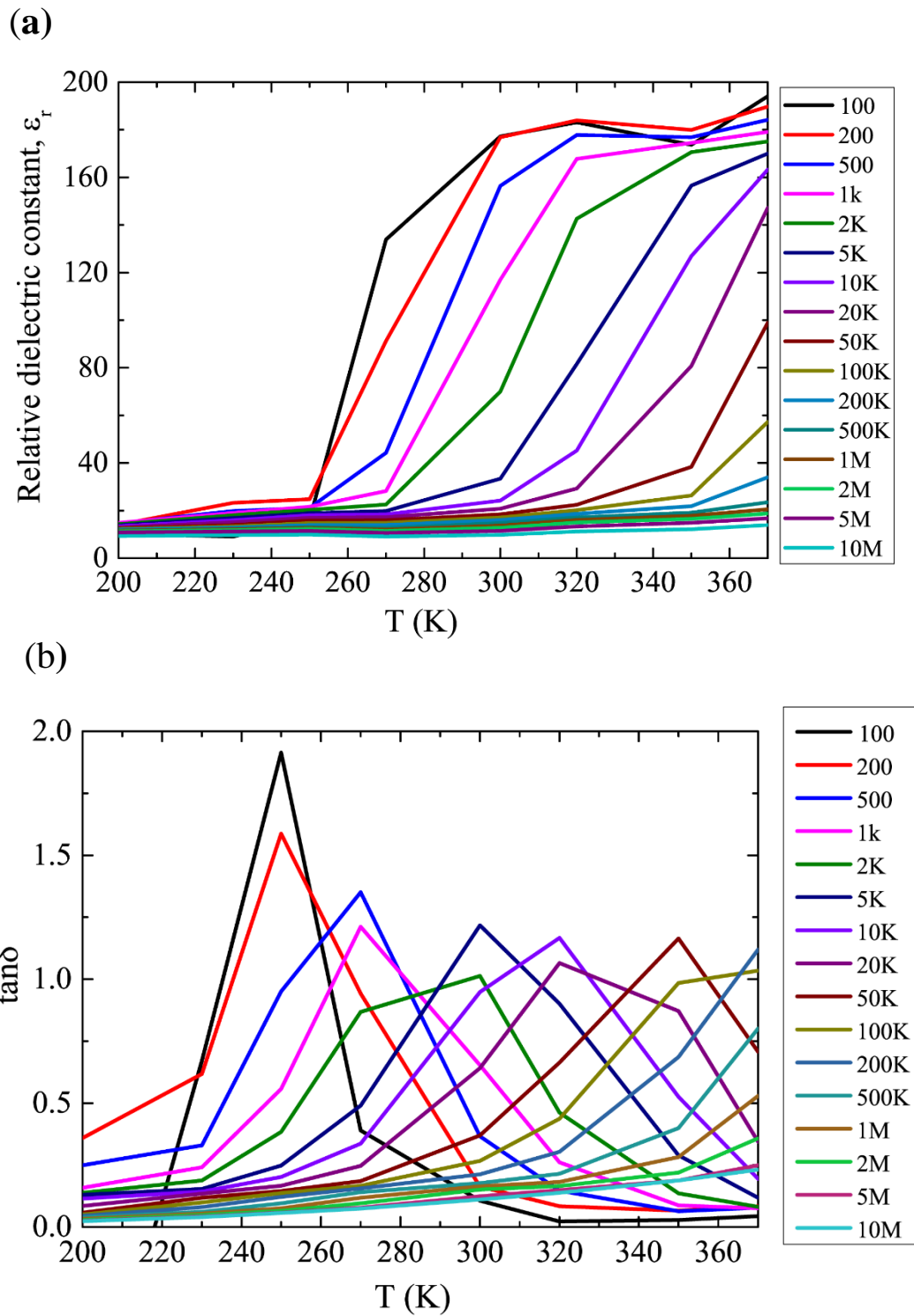


Figure 4-14 Temperature dependence of relative dielectric constant (a) and Temperature dependence of loss tangent (b) for $\text{Sc}_{0.5}\text{Fe}_{1.5}\text{O}_3$ film at frequencies $f = 100\text{-}10\text{M}$ Hz.

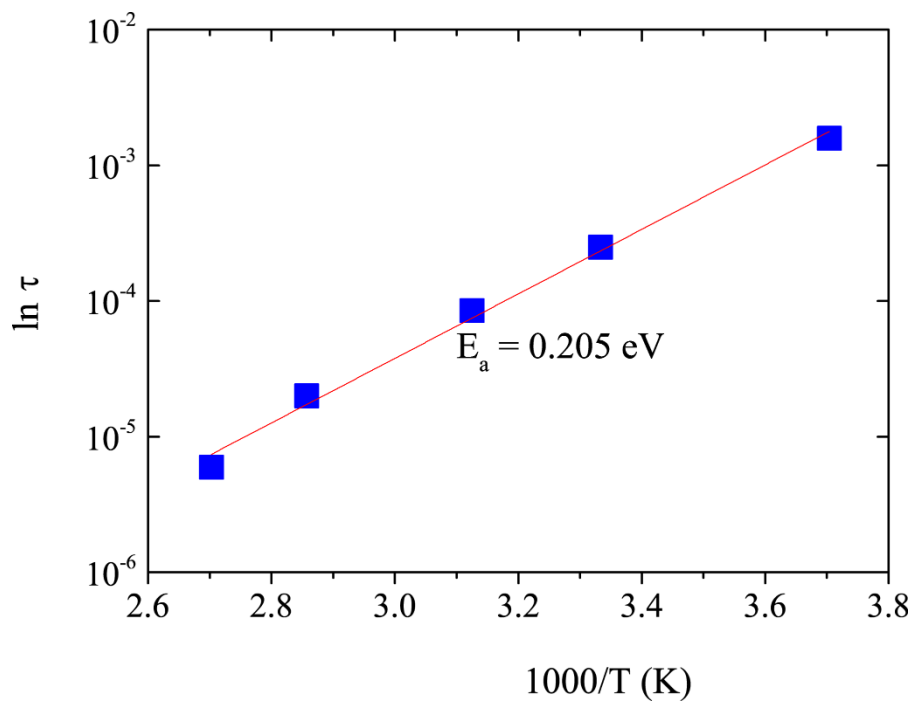


Figure 4-15 The log of the relaxation time τ vs $1000/T$. The square symbols are the experiment points and red solid line is the Arrhenius fits.

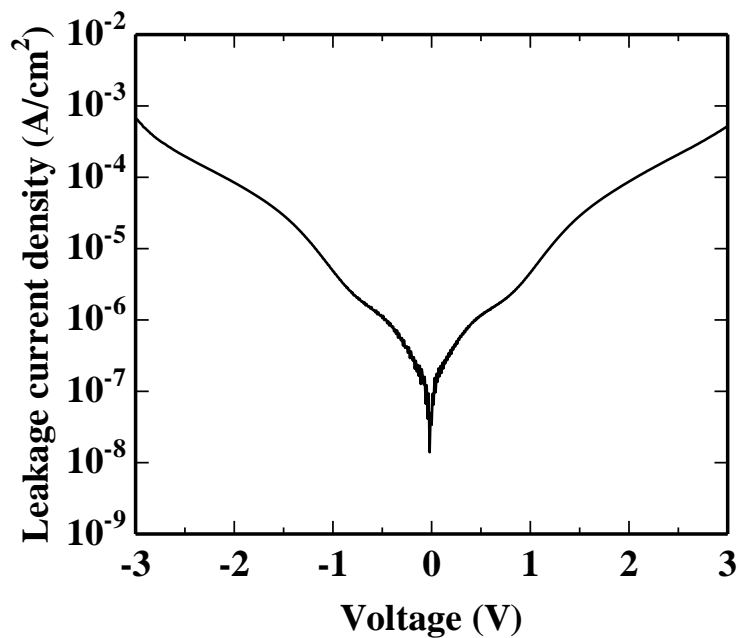


Figure 4-16 Leakage current density of $\text{Sc}_{0.5}\text{Fe}_{1.5}\text{O}_3$ film as functions of electric field.

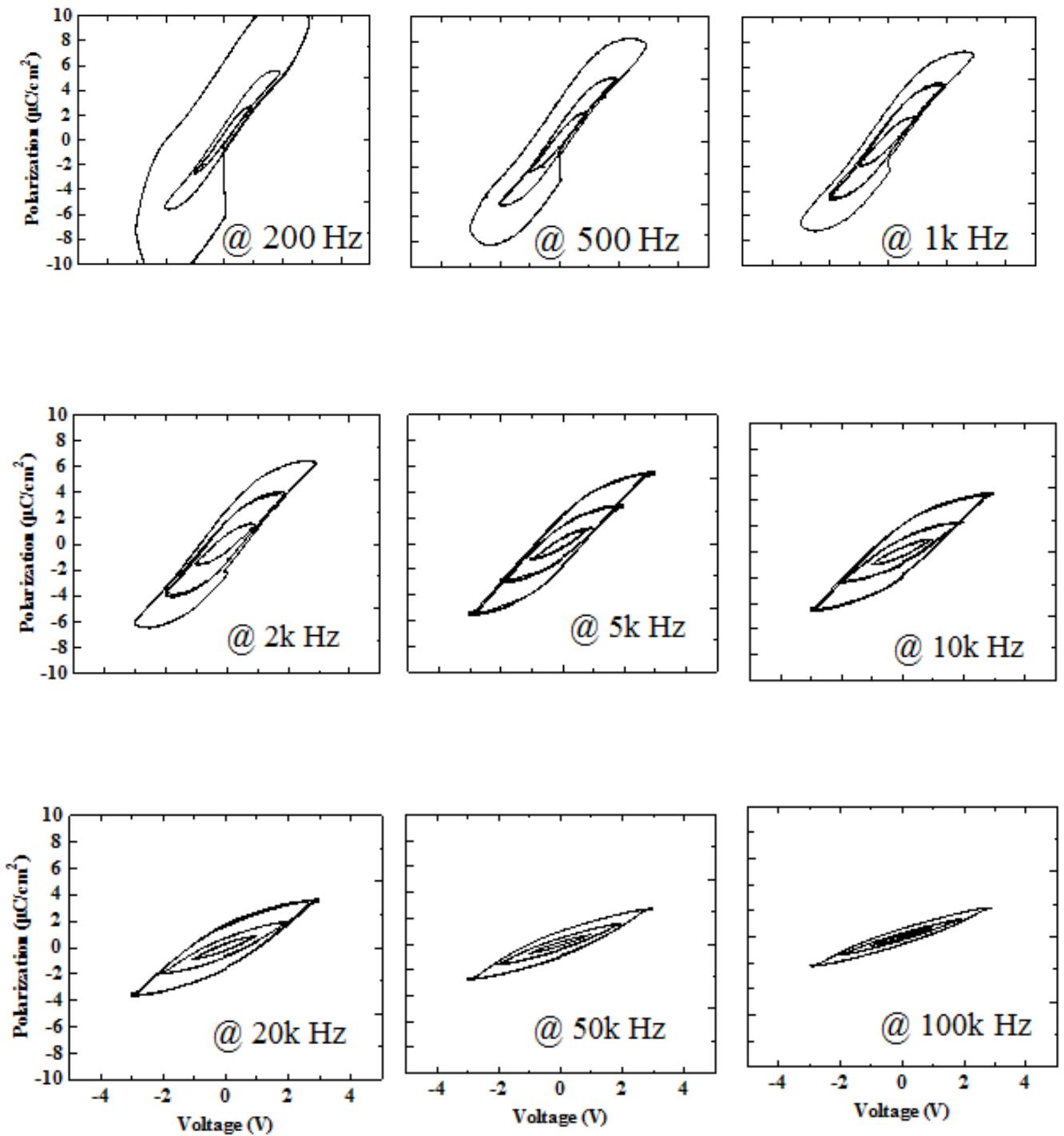


Figure 4-17 *P-E* hysteresis loops of ScFeO₃ film measured at 200-100kHz and room temperature.

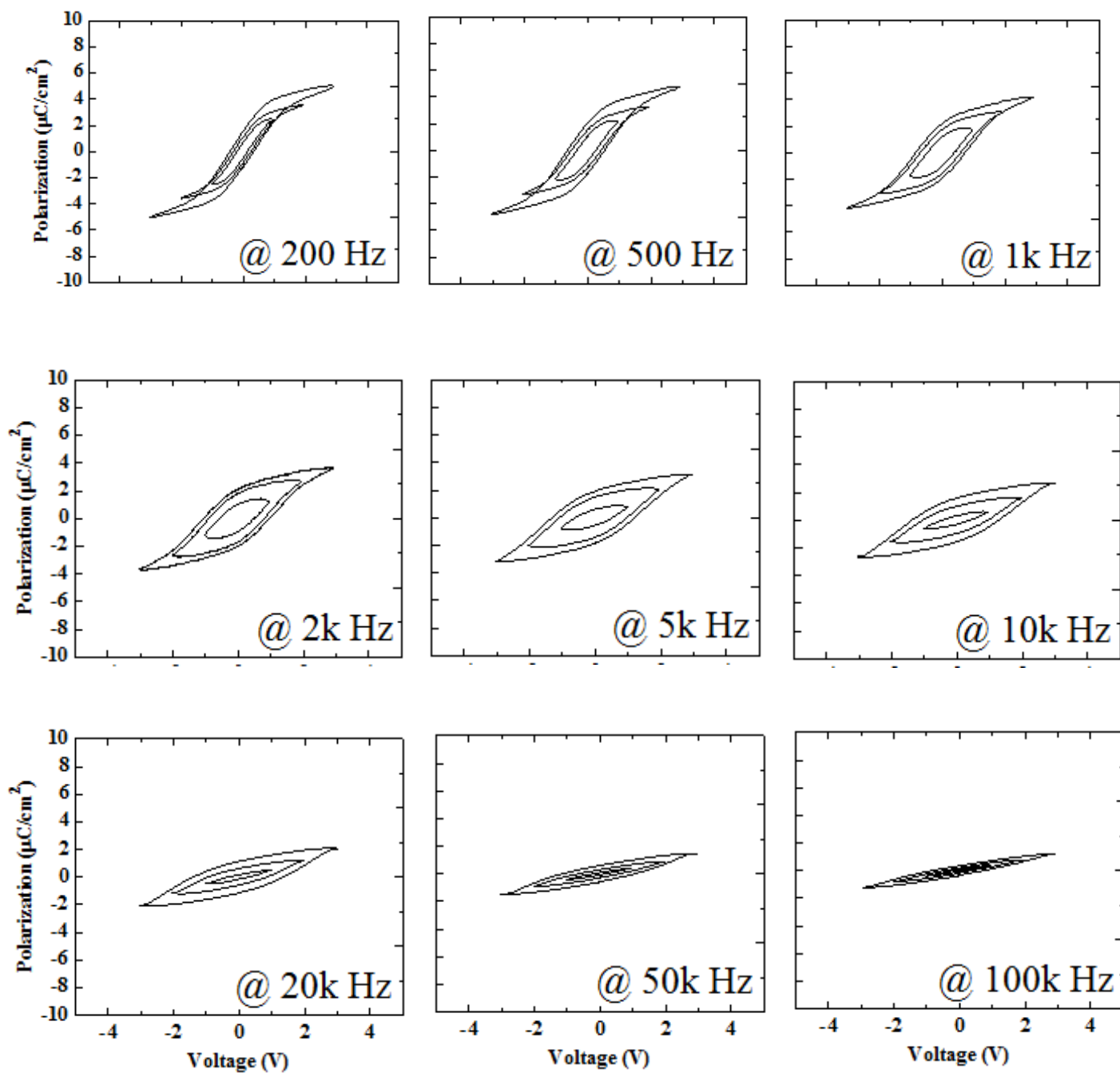


Figure 4-18 *P-E* hysteresis loops of $\text{Sc}_{0.5}\text{Fe}_{1.5}\text{O}_3$ film measured at 200-100kHz and room temperature.

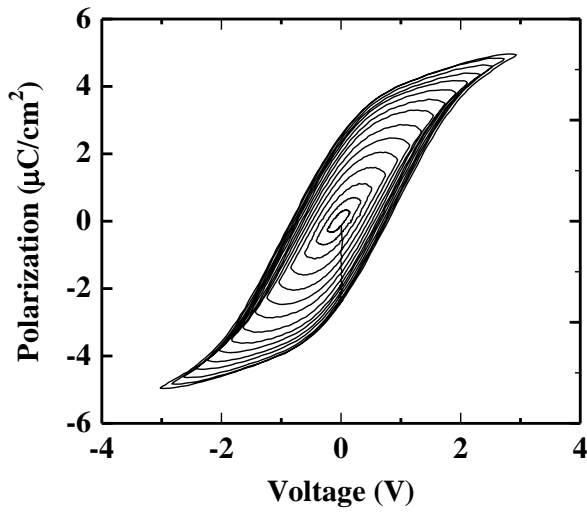


Figure 4-19 P - E hysteresis loops of $\text{Sc}_{0.5}\text{Fe}_{1.5}\text{O}_3$ film measured at 1 kHz and room temperature.

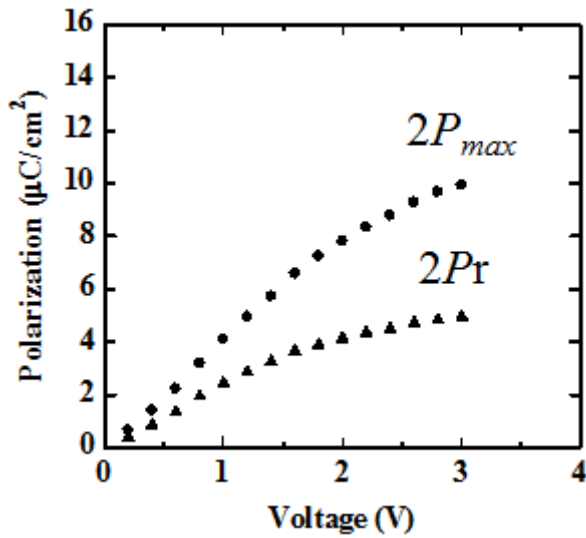


Figure 4-20 Remanent and maximum polarization of $\text{Sc}_{0.5}\text{Fe}_{1.5}\text{O}_3$ film measured at 1 kHz and room temperature.

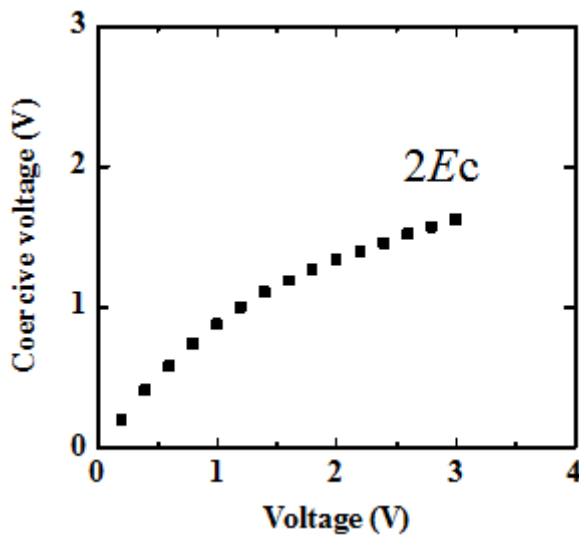


Figure 4-21 Coercive field of $\text{Sc}_{0.5}\text{Fe}_{1.5}\text{O}_3$ film measured at 1 kHz and room temperature.

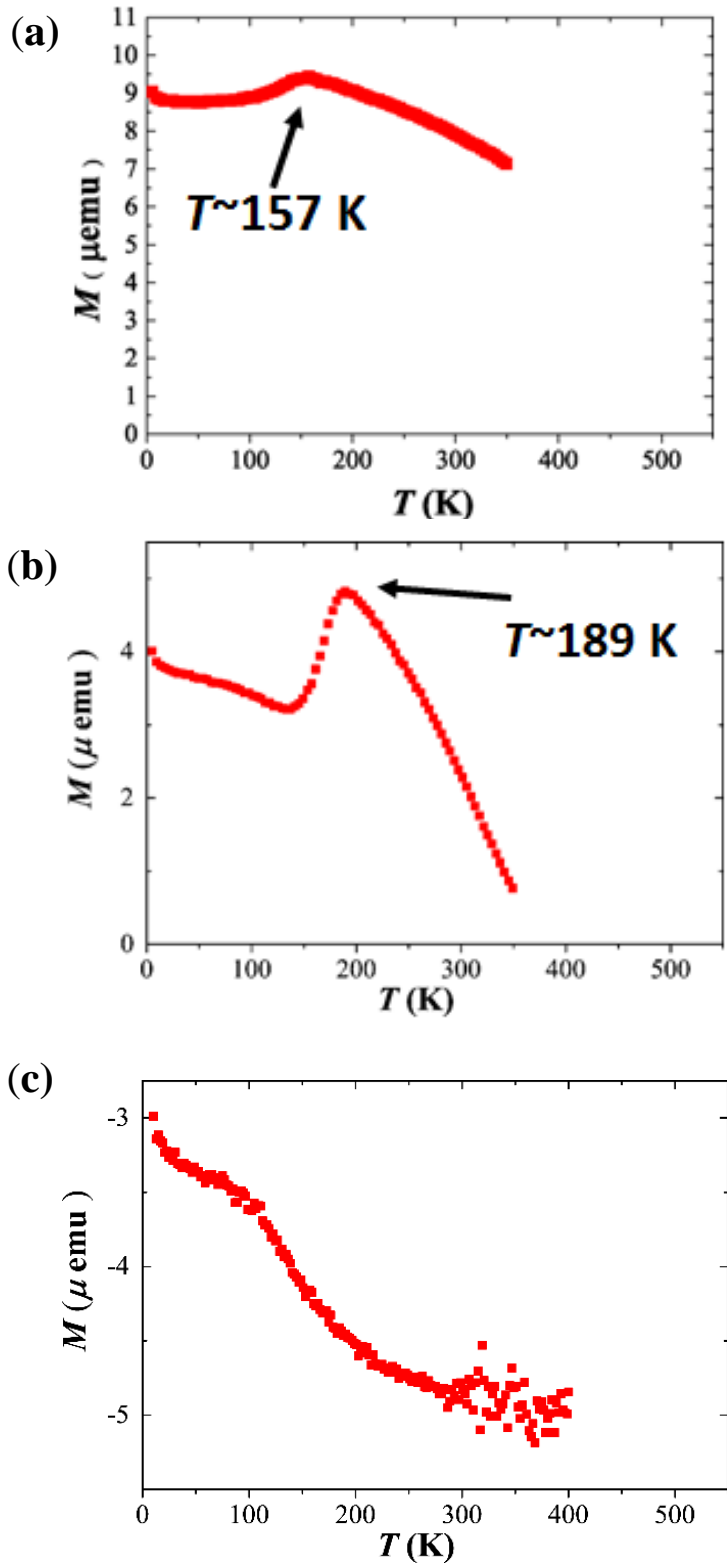


Figure 4-21 Temperature dependence of the field cooled magnetization measured at $H= 500\text{Oe}$ in Fe_2O_3 (a), $\text{Sc}_{0.5}\text{Fe}_{1.5}\text{O}_3$ (b) and ScFeO_3 (c).

Reference

- [1] J. Cassedanne and H. Forestier, “Sc₂O₃-Fe₂O₃ phase diagram.pdf,” *C. R. Hebd. Seances Acad. Sci.*, vol. 250, pp. 2898–2900, 1960.
- [2] S. Sakurai, J. Jin, K. Hashimoto, and S. Ohkoshi, “Reorientation Phenomenon in a Magnetic Phase of ϵ -Fe₂O₃ Nanocrystal,” *J. Phys. Soc. Japan*, vol. 74, pp. 1946–1949, 2005.
- [3] A. Namai, M. Yoshikiyo, S. Umeda, T. Yoshida, T. Miyazaki, M. Nakajima, K. Yamaguchi, T. Suemoto, and S. Ohkoshi, “The synthesis of rhodium substituted ϵ -iron oxide exhibiting super high frequency natural resonance,” *J. Mater. Chem. C*, vol. 1, p. 5200, 2013.
- [4] S. Sakurai, S. Kuroki, H. Tokoro, K. Hashimoto, and S. Ohkoshi, “Synthesis, Crystal Structure, and Magnetic Properties of ϵ -In_xFe_{2-x}O₃ Nanorod-Shaped Magnets,” *Adv. Funct. Mater.*, vol. 17, pp. 2278–2282, 2007.
- [5] S. Sakurai, A. Namai, K. Hashimoto, and S. Ohkoshi, “First observation of phase transformation of all four Fe₂O₃ phases ($\gamma \rightarrow \epsilon \rightarrow \beta \rightarrow \alpha$ -phase).,” *J. Am. Chem. Soc.*, vol. 131, pp. 18299–18303, 2009.
- [6] I. Levin and D. Brandon, “Metastable Alumina Polymorphs: Crystal Structures and Transition Sequences,” *J. Am. Ceram. Soc.*, vol. 81, pp. 1995–2012, 1998.
- [7] N. Ikeda, H. Ohsumi, K. Ohwada, K. Ishii, T. Inami, K. Kakurai, Y. Murakami, K. Yoshii, S. Mori, Y. Horibe, and H. Kitô, “Ferroelectricity from iron valence ordering in the charge-frustrated system LuFe₂O₄,” *Nature*, vol. 436, pp. 1136–1138, 2005.
- [8] Y. J. Wu, Y. Gao, and X. M. Chen, “Dielectric relaxations of yttrium iron garnet ceramics over a broad temperature range,” *Appl. Phys. Lett.*, vol. 91, p. 092912,

2007.

- [9] B. Srimathy, I. Bhaumik, S. Ganesamoorthy, R. Bhatt, a. K. Karnal, and J. Kumar, “On the Neel temperature and magnetic domain wall movements of $\text{Ga}_{2-x}\text{Fe}_x\text{O}_3$ single crystals grown by floating-zone technique,” *J. Alloys Compd.*, vol. 590, pp. 459–464, 2014.
- [10] M. Gich, C. Frontera, A. Roig, E. Taboada, E. Molins, H. R. Rechenberg, J. D. Ardisson, W. A. A. Macedo, C. Ritter, V. Hardy, J. Sort, V. Skumryev, and J. Nogués, “High- and Low-Temperature Crystal and Magnetic Structures of $\epsilon\text{-Fe}_2\text{O}_3$ and Their Correlation to Its Magnetic Properties,” *Chem. Mater.*, vol. 18, pp. 3889–3897, 2006.
- [11] S. Ohkoshi and H. Tokoro, “Hard Magnetic Ferrite: $\epsilon\text{-Fe}_2\text{O}_3$,” *Bull. Chem. Soc. Jpn.*, vol. 86, pp. 897–907, 2013.

Phase Equilibria Diagrams Online Database (NIST Standard Reference Database 31), The American Ceramics Society and the National Institute of Standards and Technology, 2015. Figure 4-1; www.nist.gov/srd/nist31.cfm.

Chapter 5

$\text{In}_2\text{O}_3\text{-Fe}_2\text{O}_3$ System

5.1 Introduction

In chapter 3 and 4, we prepared κ -Al₂O₃-type Al_xFe_{2-x}O₃ and Sc_xFe_{2-x}O₃ films and studied the ferroelectricity in these films. We obtained ferroelectric hysteresis loop of Sc_{0.5}Fe_{1.5}O₃ film at room temperature. In chapter 5, we focused on Indium. According to *ab initio* calculation by Konishi, the activation energy of In₂O₃ for polarization switching has almost same as that of Sc₂O₃ (see Appendix). κ -Al₂O₃-type In_xFe_{2-x}O₃ can not be obtained by the conventional solid reaction[1] (Figure 5-1). κ -Al₂O₃-type In_xFe_{2-x}O₃ (0 ≤ x ≤ 0.24) are prepared by combining reverse micelle and sol-gel techniques[2]. However, ferroelectricity of κ -Al₂O₃-type In_xFe_{2-x}O₃ have not been reported. In this chapter, we attempted to stabilize κ -Al₂O₃-type In_xFe_{2-x}O₃ by PLD and investigated the ferroelectricity in κ -Al₂O₃-type In_xFe_{2-x}O₃ films.

5.2 Experiment

In_xFe_{2-x}O₃ films were grown on SrTiO₃(111) single-crystal substrates by PLD technique. A fourth-harmonic wave of a Nd: YAG laser ($\lambda = 266$ nm) was used. A repetition rate and a fluence of a Nd: YAG laser are 5Hz and 2.4, respectively. The target was prepared by mixing In₂O₃ and α -Fe₂O₃ powder and sintering at 1350°C for 6 hours in air. Chemical composition of targets are InFeO₃, In_{0.5}Fe_{1.5}O₃, In_{0.25}Fe_{1.75}O₃ and Fe₂O₃. The crystal structure of films were investigated by high-resolution X-ray diffraction (XRD) using a Rigaku Smart-Lab diffractometer. X-ray was monochromatized using a Ge(220) 2-bounce crystal and Cu K α radiation ($\lambda = 1.5406$ Å) was used. The Reciprocal space mapping (RSM) was measured to estimate to lattice constants. P-E hysteresis loop was measured by ferroelectric tester (Toyo Corporation, FCE) Pt as top electrode was deposited by the electric beam evaporation method. The field-cooled (FC) dc

magnetization was measured in a Quantum Design MPMS. The FC magnetization was recorded at 500 Oe and 10-350 K.

5.3 Result and Discussion

5.3.1 Growth of $\text{In}_x\text{Fe}_{2-x}\text{O}_3$ Films

As described at chapter 3, $\epsilon\text{-Fe}_2\text{O}_3$ film on $\text{SrTiO}_3(111)$ was obtained only in a limited condition of the deposition. Following this results, $\text{In}_x\text{Fe}_{2-x}\text{O}_3$ film was deposited on $\text{SrTiO}_3(111)$ substrate at 600-800 °C under 100mTorr in O_2 . A laser fluence of 0.96 J cm^{-2} was used. XRD 2θ - θ pattern of $\text{In}_x\text{Fe}_{2-x}\text{O}_3$ film deposited on 600 °C were shown in Figure 5-2. XRD pattern of the $\text{In}_{0.25}\text{Fe}_{1.75}\text{O}_3$ film shows similar to that of Fe_2O_3 film (see Figure 2-11). As described in chapter 3, the XRD pattern of Fe_2O_3 film corresponds to $\kappa\text{-Al}_2\text{O}_3$ -type Fe_2O_3 epitaxial film. Therefore, $\kappa\text{-Al}_2\text{O}_3$ -type $\text{In}_{0.25}\text{Fe}_{1.75}\text{O}_3$ film was epitaxially grown on $\text{SrTiO}_3(111)$ substrate. We will discuss the more detail of $\kappa\text{-Al}_2\text{O}_3$ -type $\text{In}_{0.25}\text{Fe}_{1.75}\text{O}_3$ film later. By contrast with $\text{In}_{0.25}\text{Fe}_{1.75}\text{O}_3$ and Fe_2O_3 films, another diffraction pattern was observed in InFeO_3 film. The observed six peaks correspond to $002l$ diffractions of hexagonal structure. Nonpolar YAlO_3 -type ($P6_3/mmc$, $Z = 2$) and YMnO_3 -type polar ($P6_3cm$, $Z = 6$) structures have been reported in ABO_3 hexagonal structure. These phases can be distinguished by the existence of superlattice peaks associated with the structural reconstruction. In-plane X-ray measurement reveals that no superlattice peaks were observed, which indicated that the crystal structure of InFeO_3 film is of YAlO_3 -type. Thus, YAlO_3 -type InFeO_3 was epitaxially grown on $\text{SrTiO}_3(111)$ substrate. The $\text{In}_{0.5}\text{Fe}_{1.5}\text{O}_3$ film have multiphase which are $\kappa\text{-Al}_2\text{O}_3$ -type, YAlO_3 -type and bixbyite-type phases. Then $\text{In}_{0.25}\text{Fe}_{1.75}\text{O}_3$ film was deposited at 800 °C (Figure 5-3). The $\text{In}_{0.25}\text{Fe}_{1.75}\text{O}_3$ film deposited at 800 °C have multiphase which are $\kappa\text{-Al}_2\text{O}_3$ -type,

YAlO₃-type and bixbyite-type phases. These results were summarized in Figure 5-4. Therefore κ -Al₂O₃-type In_xFe_{2-x}O₃ film can be obtained at 600 °C on SrTiO₃(111) in the range of $x = 0-0.25$.

We discuss the more detail of κ -Al₂O₃-type In_{0.25}Fe_{1.75}O₃ film. Figure 5-5(a) illustrated the XRD pattern of κ -Al₂O₃-type In_{0.25}Fe_{1.75}O₃. Four peaks at $2\theta = 18.51^\circ$, 37.51° , 57.67° and 80.04° without that of substrates were observed. These peaks were corresponded to 002 , 004 , 006 and 008 reflections of κ -Al₂O₃-type structures. We have succeeded in stabilizing κ -Al₂O₃-type In_{0.25}Fe_{1.75}O₃ on SrTiO₃(111) substrate. The result indicates that κ -Al₂O₃-type In_{0.25}Fe_{1.75}O₃ was epitaxially grown on SrTiO₃(111) substrate with the out of plane orientation relationship of κ -Al₂O₃-type In_{0.25}Fe_{1.75}O₃ (001) || SrTiO₃(111) without impurity phase. As can be seen in Figure 5-5(b), the thickness fringes were observed around 004 peaks. The full-width-at-half-maximum (FWHM) value of rocking curve was measured at 008 reflections. The FWHM value of In_{0.25}Fe_{1.75}O₃ was 0.075° . These results suggest that In_{0.25}Fe_{1.75}O₃ is high quality. RSM were measured around In_{0.25}Fe_{1.75}O₃ 2010 and 507 reflections (Figure 5-6). It seems that there are no lattice strain in In_{0.25}Fe_{1.75}O₃ film on SrTiO₃ substrate. The lattice constants were estimated from XRD RSM. The a , b and c lattice constants of In_{0.25}Fe_{1.75}O₃ film are 5.156, 8.890 and 9.582 Å, respectively, while those of the Fe₂O₃ film are 5.088, 8.798 and 9.466 Å, respectively. The lattice constants of the In_{0.25}Fe_{1.75}O₃ film are larger than those of the Fe₂O₃ film, indicating that In₂O₃ forms a solid solution with κ -Al₂O₃-type Fe₂O₃. The result is consistent with the fact that the ionic radius of In³⁺ [0.800 Å (VI)] is larger than that of Fe³⁺ [0.645 Å (VI)]. Moreover, the lattice constants of In_{0.25}Fe_{1.75}O₃ film are almost same as that of In_{0.24}Fe_{1.76}O₃ nanorod ($a = 5.141$ Å, $b = 8.838$ Å and $c = 9.522$ Å)[2].

5.3.2 Dielectric and ferroelectric properties

Figure 5-7 illustrates frequency dependence of the relative dielectric constant and the loss tangent in $\text{In}_{0.25}\text{Fe}_{1.75}\text{O}_3$ epitaxial film measure at room temperature. As in the case of $\text{Sc}_{0.5}\text{Fe}_{1.5}\text{O}_3$ film, the dielectric dispersion and the dielectric loss peak was observed at about 10 kHz. The relative dielectric constant of about 220 at 100 Hz rapidly decreased above 1 kHz. This dispersion is may be the contribution of the valence fluctuation of iron ions.

P - E hysteresis loop of $\text{In}_{0.25}\text{Fe}_{1.75}\text{O}_3$ epitaxial film measured at room temperature and frequency of 1 kHz is shown in Figure 5-8. The saturated ferroelectric hysteresis loop was observed in $\text{In}_{0.25}\text{Fe}_{1.75}\text{O}_3$ film. The remnant polarization is about $2 \mu\text{C}/\text{cm}^2$. Figure 5-9 (a) and (b) show remanent polarization, maximum polarization and coercive voltage as functions of the applied maximum voltage. These values monotonically increased with increasing applied voltage, and shows saturated behavior. From these results, we confirmed the ferroelectricity in $\text{In}_{0.25}\text{Fe}_{1.75}\text{O}_3$ film.

5.3.3 Magnetic property

Figure 5-10 shows the in-plane magnetic hysteresis curves of the κ - Al_2O_3 -type $\text{In}_{0.25}\text{Fe}_{1.75}\text{O}_3$ film at 300 K, where the diamagnetic contribution from the substrate is subtracted. The observed saturation magnetization is $0.24 \mu_{\text{B}}/\text{Fe}$, which is close to that of $\text{In}_{0.24}\text{Fe}_{1.76}\text{O}_3$ nanorods ($0.28 \mu_{\text{B}}/\text{Fe}$). Figure 5-11 (a) and (b) display temperature dependence of the field cooled magnetization measured at $H=500\text{Oe}$ in Fe_2O_3 and $\text{In}_{0.25}\text{Fe}_{1.75}\text{O}_3$ films. We discussed the detail of magnetization in κ - Al_2O_3 -type Fe_2O_3 film at chapter 4. The magnetization of $\text{In}_{0.25}\text{Fe}_{1.75}\text{O}_3$ rapidly decreased below 205 K. This behavior is same as κ - Al_2O_3 -type Fe_2O_3 film and it corresponds to the phase transition

temperature from ferrimagnetism to incommensurate magnetic order. According to the report of $\text{In}_{0.25}\text{Fe}_{1.75}\text{O}_3$ nanorods by S. Sakurai, the phase transition temperature (T_p) is 206 K. The T_p value of $\text{In}_{0.25}\text{Fe}_{1.75}\text{O}_3$ film is close to that of $\text{In}_{0.25}\text{Fe}_{1.75}\text{O}_3$ nanorods[2].

5.4 Summary

In this chapter, we prepared $\text{In}_x\text{Fe}_{2-x}\text{O}_3$ films on $\text{SrTiO}_3(111)$ substrate. GaFeO_3 -type epitaxial films were obtained in Fe_2O_3 and $\text{In}_{0.25}\text{Fe}_{1.75}\text{O}_3$ compositions. Single phase YAlO_3 -type InFeO_3 film was also obtained. The dielectric property of $\text{In}_{0.25}\text{Fe}_{1.75}\text{O}_3$ film shows the dielectric dispersion around 10kHz. We succeeded in obtaining ferroelectric P - E hysteresis loop of $\text{In}_{0.25}\text{Fe}_{1.75}\text{O}_3$ film with a remnant polarization of $2.0 \mu\text{Ccm}^{-2}$ at room temperature. Considering the result of $\text{Sc}_{0.5}\text{Fe}_{1.5}\text{O}_3$ film, substitution of Me^{3+} which have a larger ionic radius than Fe^{3+} in a $\kappa\text{-Al}_2\text{O}_3$ -type Fe_2O_3 effective to obtain ferroelectric hysteresis loop at room temperature. This tendency consistent with the result of first principle calculation.

Figures

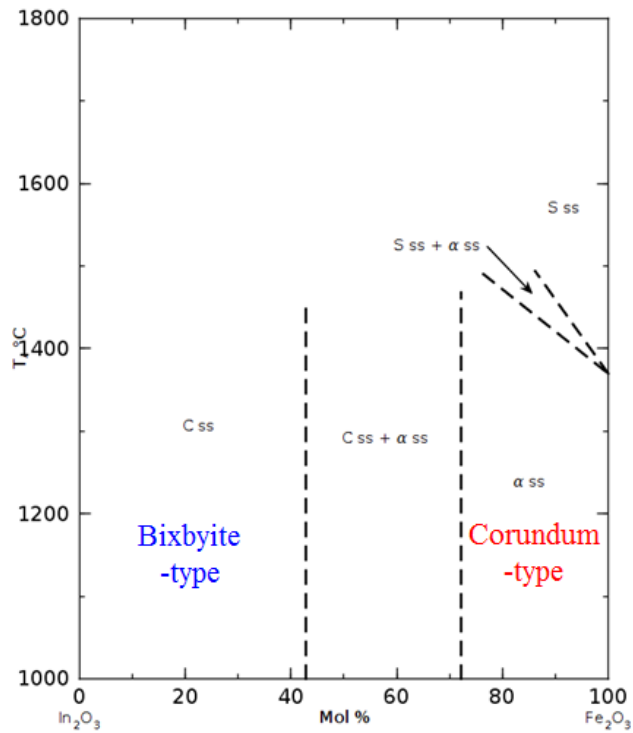


Figure 5-1 $\text{In}_2\text{O}_3\text{-Fe}_2\text{O}_3$ phase diagram, where ss is solid solution.

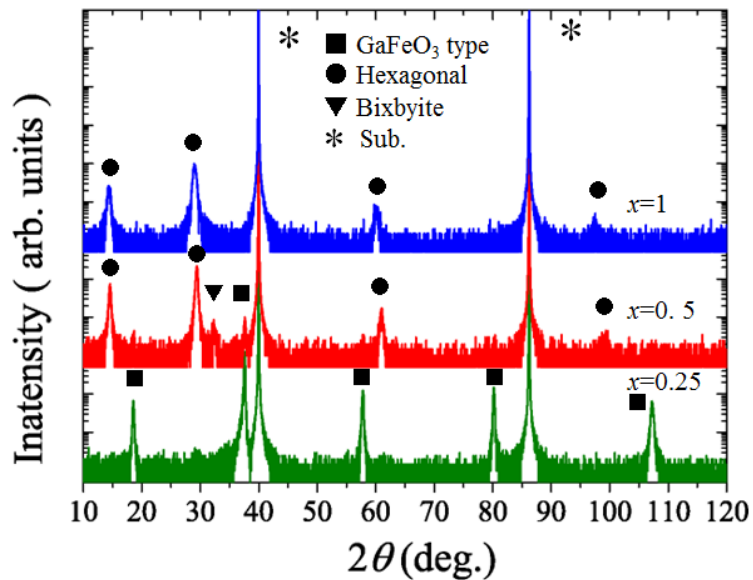


Figure 5-2 XRD θ - 2θ pattern of InFeO_3 , $\text{In}_{0.5}\text{Fe}_{1.5}\text{O}_3$ and $\text{In}_{0.25}\text{Fe}_{1.75}\text{O}_3$ films deposited at 600°C with 2θ angle of $10\text{-}120^{\circ}$. * correspond to the peaks of substrates.

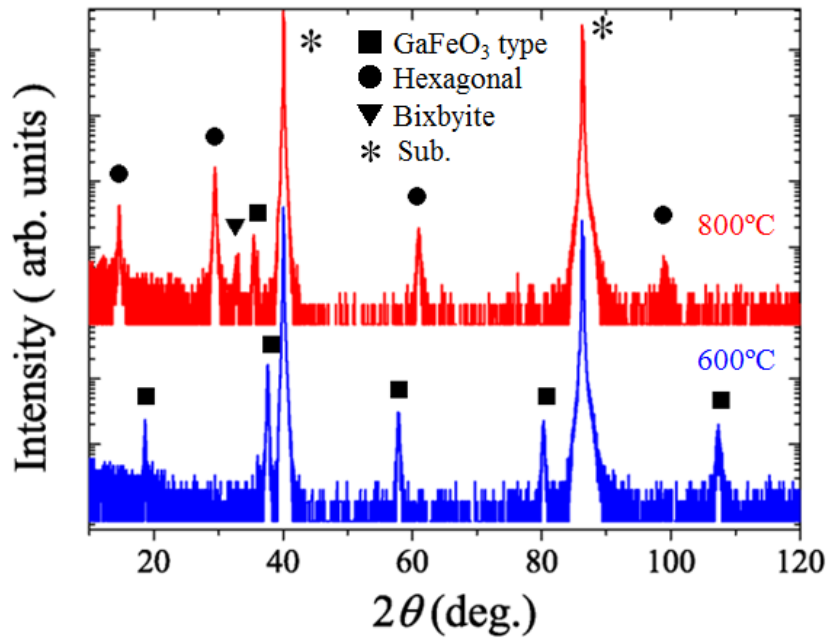


Figure 5-3 XRD θ - 2θ pattern of $\text{In}_{0.25}\text{Fe}_{1.75}\text{O}_3$ films deposited at 600 and 800°C with 2θ angle of 10-120°. * correspond to the peaks of substrates.

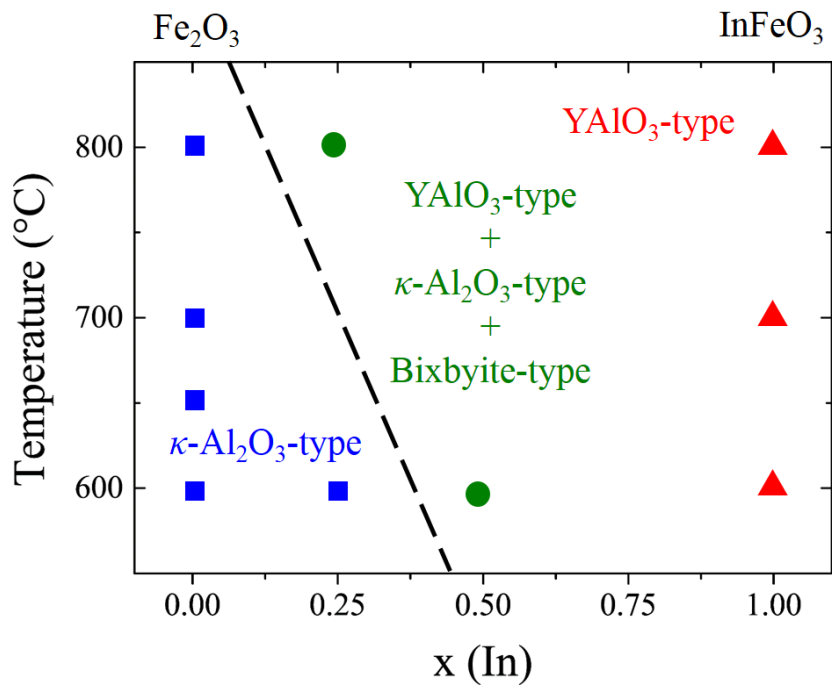


Figure 5-4 Phase diagram of $\text{In}_x\text{Fe}_{2-x}\text{O}_3$ films deposited on $\text{SrTiO}_3(111)$ substrates.

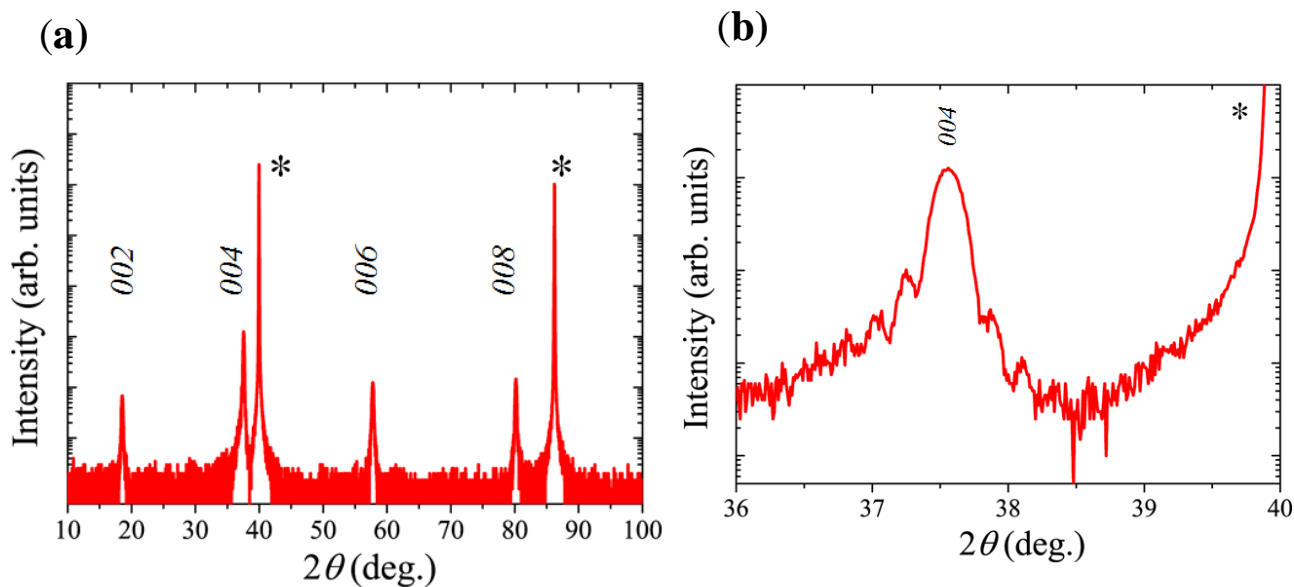


Figure 5-5 XRD θ - 2θ pattern of $\text{In}_{0.25}\text{Fe}_{1.75}\text{O}_3$ films with 2θ angle of 10 - 100° (a) and 36 - 40° (b). * correspond to the peaks of substrates.

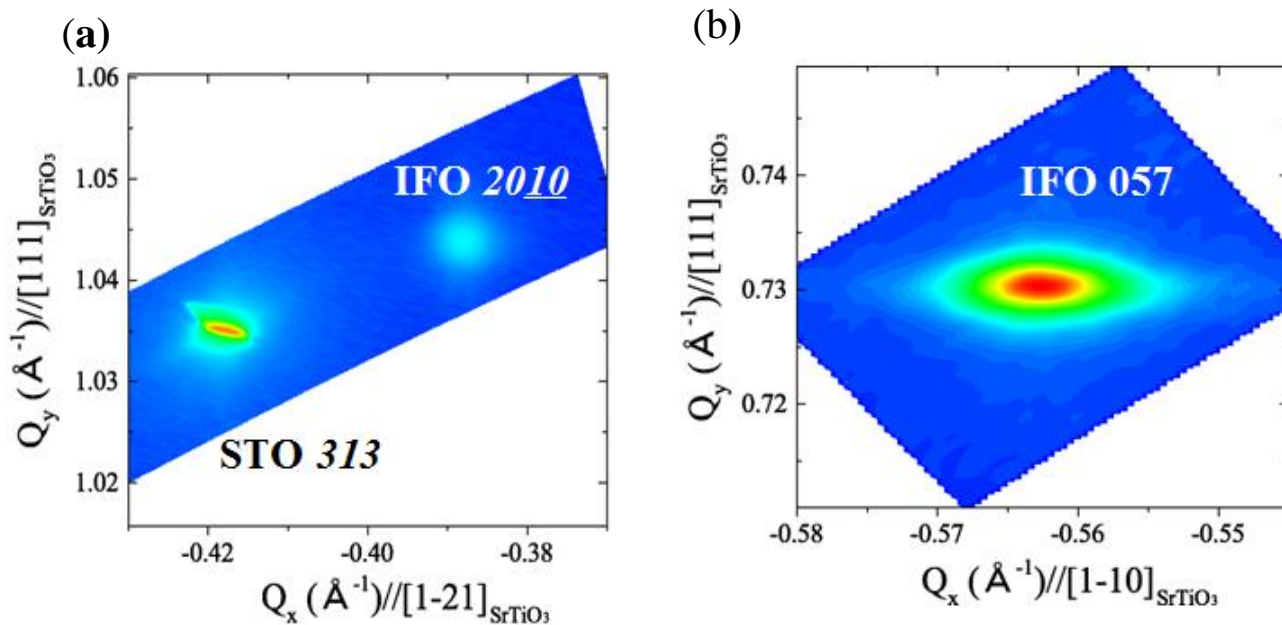


Figure 5-6 XRD-RSM around κ - Al_2O_3 -type $\text{Sc}_x\text{Fe}_{2-x}\text{O}_3$ $20\bar{1}0$ and 057 diffractions.

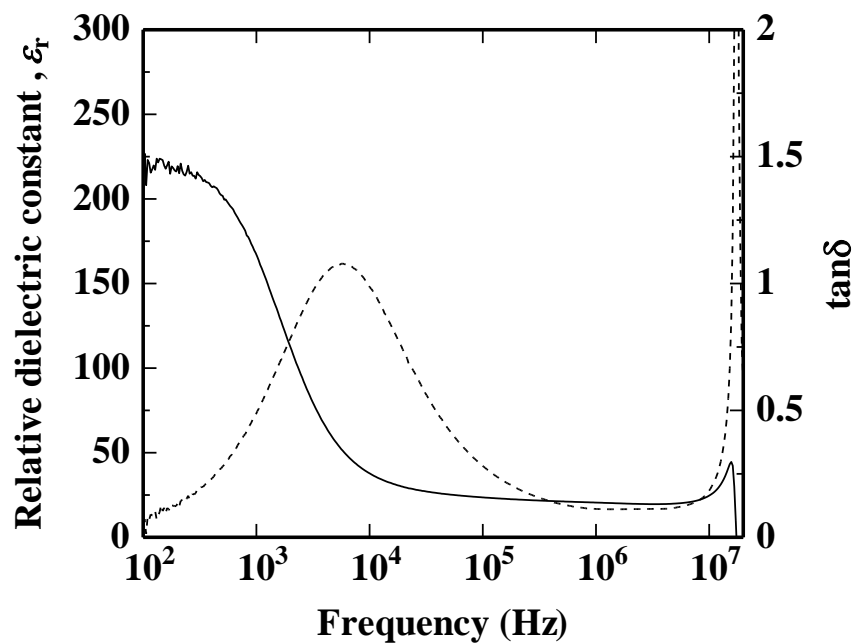


Figure 5-7 Frequency dependence of relative dielectric constant and loss tangent in $\text{In}_{0.25}\text{Fe}_{1.75}\text{O}_3$ epitaxial film measured at room temperature.

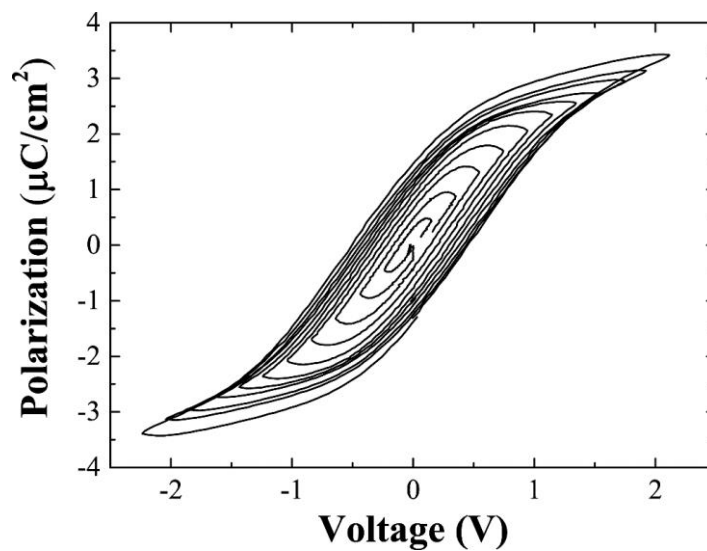


Figure 5-8 P - E hysteresis loops of $\text{In}_{0.25}\text{Fe}_{1.75}\text{O}_3$ film measured at 1 kHz and room temperature.

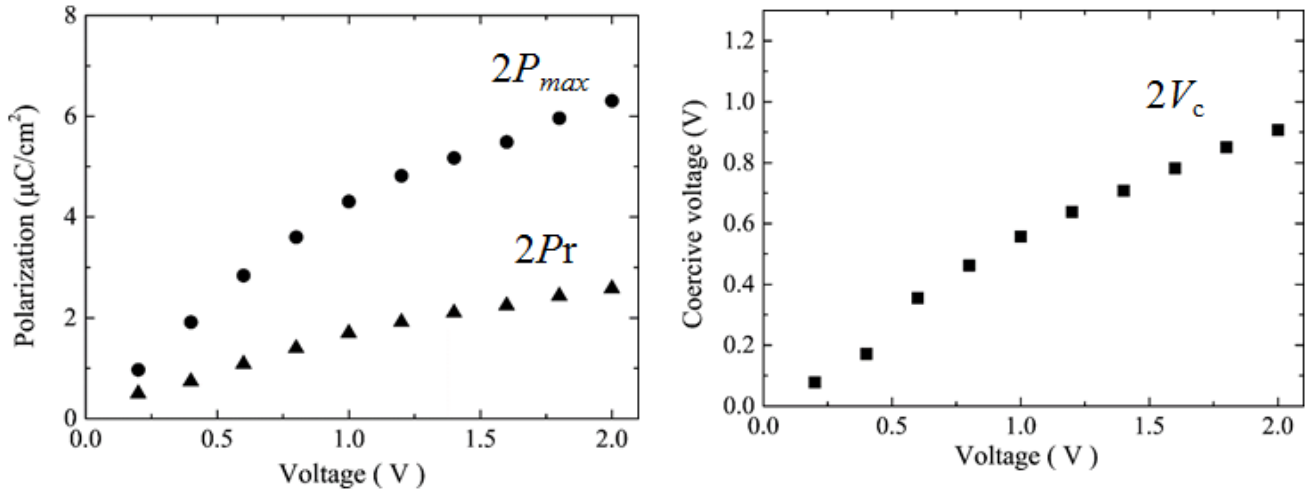


Figure 5-9 Remanent polarization, maximum polarization and coercive voltage of $\text{In}_{0.25}\text{Fe}_{1.75}\text{O}_3$ film measured at 1 kHz and room temperature.

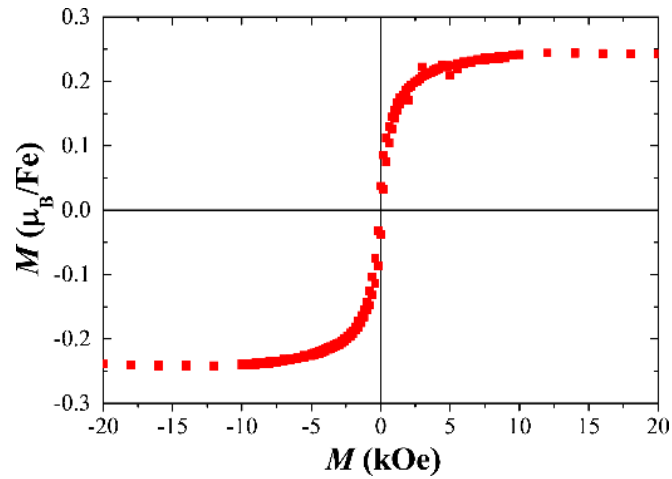


Figure 5-10 In-plane magnetic hysteresis loops after subtraction of the diamagnetic contribution from the substrate at 300 K. Magnetic field is applied along SrTiO_3 [111].

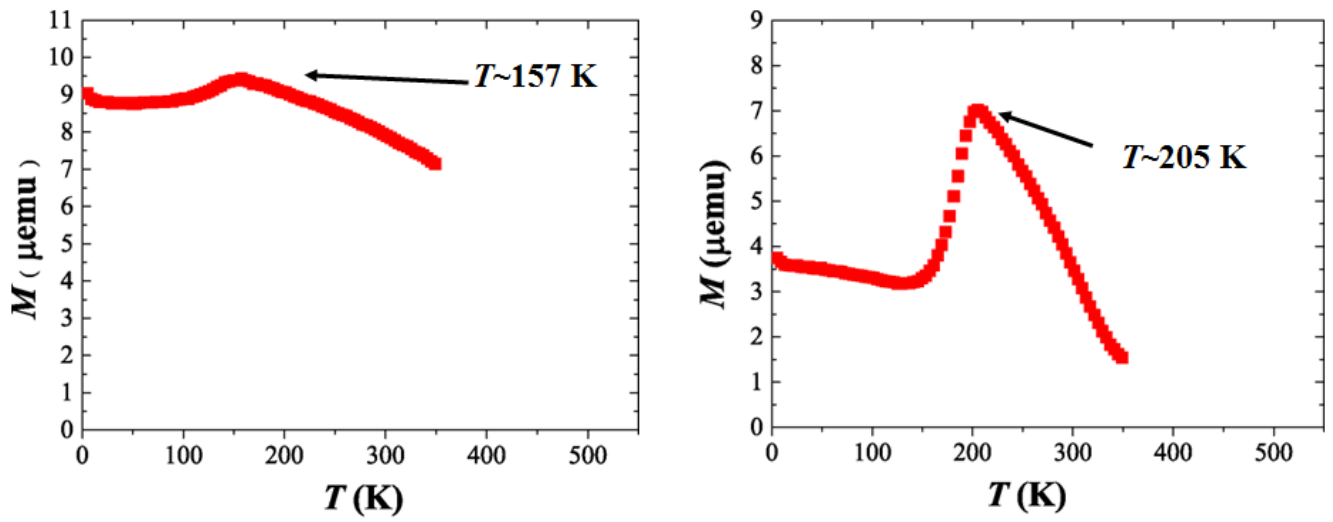


Figure 5-11 Temperature dependence of the field cooled magnetization measured at $H = 500\text{Oe}$ in (a) Fe_2O_3 and (b) $\text{In}_{0.25}\text{Fe}_{1.75}\text{O}_3$.

Reference

- [1] S. J. Schneider, R. S. Roth, and J. L. Waring, "Solid state reactions involving oxides of trivalent cations," *J. Res. Natl. Bur. Stand. Sect. A Phys. Chem.*, vol. 65A, no. 4, p. 345, 1961.
- [2] S. Sakurai, S. Kuroki, H. Tokoro, K. Hashimoto, and S. Ohkoshi, "Synthesis, Crystal Structure, and Magnetic Properties of ϵ - $\text{In}_x\text{Fe}_{2-x}\text{O}_3$ Nanorod-Shaped Magnets," *Adv. Funct. Mater.*, vol. 17, no. 14, pp. 2278–2282, Sep. 2007.

Phase Equilibria Diagrams Online Database (NIST Standard Reference Database 31),
The American Ceramics Society and the National Institute of Standards and
Technology, 2015. Figure 5-1; www.nist.gov/srd/nist31.cfm.

Chapter 6

Conclusion

6.1. Conclusions

I have attempted to prepare metastable κ -Al₂O₃-type compounds by PLD technique. κ -Al₂O₃-type $Me_xFe_{2-x}O_3$ ($Me = Al, Sc$ and In) were investigated. In κ -Al₂O₃-type $Al_xFe_{2-x}O_3$, $Sc_xFe_{2-x}O_3$ and $In_xFe_{2-x}O_3$ films, the ferroelectric hysteresis loop is observed. Especially, we have succeeded in obtaining ferroelectric hysteresis loop of $Sc_{0.5}Fe_{1.5}O_3$ and $In_{0.25}Fe_{1.75}O_3$ films at room temperature. The substitution of Me^{+3} with larger ionic radii than that of Fe in a κ -Al₂O₃-type Fe_2O_3 is effective to obtain ferroelectric hysteresis loop at room temperature, implying reduction of activation energy for polarization switching. This consistent with the first principle calculation results calculated by Konishi. I also have demonstrated to control crystal structures of film through selection of substrates.

Main result are summarized as follows.

In chapter 2, five crystal structures; corundum, bixbyite, spinel, κ -Al₂O₃ and YMnO₃-type, were stabilized in film form. Except for bixbyite-type ScFeO₃, spinel-, YMnO₃-, corundum-, and κ -Al₂O₃-type ScFeO₃ were prepared for the first time. Therefore, this study suggested that the epitaxial thin film technique could be one of the tool for exploitation of new functional materials.

In chapter 3, metastable κ -Al₂O₃-type $Al_xFe_{2-x}O_3$ ($x = 0-1.8$) thin films were epitaxially grown on SrTiO₃ (111) substrates using PLD method. Three in-plane domains rotated 120° each other is confirmed by XRD phi-scan. HAADF-STEM image revealed the pillar structure with a width of about 10nm, which correspond to three in-plane domains. The bottom layer was also revealed by HAADF-STEM

image. The bottom layer shows completely different form κ -Al₂O₃-type structure. The ferroelectricity in κ -Al₂O₃-type Al_xFe_{2-x}O₃ films was characterized by PFM and *P-E* loop measurements. Al_{0.5}Fe_{1.5}O₃ film showed square-shaped ferroelectric hysteresis loop at 80K. The remnant polarization is about 2 $\mu\text{C}/\text{cm}^2$, and the value is smaller than the calculated value of spontaneous polarization (about 25 $\mu\text{C}/\text{cm}^2$). The reason might be attributed to the nonpolar bottom layer.

In chapter 4, κ -Al₂O₃-type Sc_xFe_{2-x}O₃ films were epitaxially grown on SrTiO₃(111) substrates. XRD phi-scan and HAADF-STEM revealed that three in-plane domains with size of about 20nm. HAADF-STEM also revealed the bottom layer, which is completely different from that of AlFeO₃ film. The crystal structure of the bottom layer in ScFeO₃ film is similar to κ -Al₂O₃-type structure. The ferroelectric hysteresis loop was obtained at room temperature in Sc_{0.5}Fe_{1.5}O₃ film. The ferroelectric hysteresis loop show strongly frequency dependencies. From these results, Sc substitution in a κ -Al₂O₃-type Fe₂O₃ is effective to obtain ferroelectric hysteresis loop at room temperature.

In chapter 5, In_xFe_{2-x}O₃ films deposited on SrTiO₃(111) substrate. κ -Al₂O₃-type epitaxial films were obtained in Fe₂O₃ and In_{0.25}Fe_{1.75}O₃ compositions. Single phase YAlO₃-type InFeO₃ film was also obtained. The ferroelectric *P-E* hysteresis loop of In_{0.25}Fe_{1.75}O₃ film was observed at room temperature. Considering the result of Sc_{0.5}Fe_{1.5}O₃ film, substitution of Me^{3+} which have a larger ionic radius than Fe³⁺ in a κ -Al₂O₃-type Fe₂O₃ effective to obtain ferroelectric hysteresis loop at room temperature.

In this study, I have performed challenging stabilization of metastable phase and confirmed that epitaxial film technique is efficient way to explore functional materials. This technique makes the evaluation of physical properties possible in materials which is unstable in bulk. I believe that the results in this study become a model of exploration for functional materials by film technique, and a lot of new compounds and crystal structure are found by film technique.

I also investigated the ferroelectricity in κ -Al₂O₃-type structure which don't require d⁰-ness cations or cations with lone-pair. First principles calculation revealed that polarization switching in κ -Al₂O₃-type structure is caused by sharing of the closed-packing oxygen layers. In κ -Al₂O₃-type structure, anions play important role for polarization switching. In order to design new ferroelectric materials, we need to consider not only cations but also anions. Phase control technique in film form allows us to control anion's structure. I believe that film technique help to design new ferroelectric materials.

Appendix

Polarization Switching of κ -Al₂O₃ type structure

The first principal calculations were performed by A. Konishi in Japan Fine Ceramics Center (JFCC).

***Ab initio* Calculation**

First-principles calculations were performed by the projector-augmented wave (PAW) method within the GGA+U formalism and the framework of density functional theory (DFT) as implemented in the VASP code. The exchange-correlation interactions were treated by the generalized gradient approximation (GGA-PBE). The on-site Coulomb repulsion was treated at the GGA+*U* level. The Hubbard effective $U_{\text{eff}} = 4.0$ eV only for the Fe-3d electrons was adopted. For the PAW potentials, 3d 4s for Fe and 2s 2p for O were explicitly treated as valence electrons. The plane wave expansion up to 600 eV was adapted. The *k*-point mesh for Brillouin zone sampling of primitive cells, which was based on the Monkhorst-Pack scheme, was $4 \times 2 \times 2$ for the 40-atom unit cell. The lattice constants and internal atomic coordinates were considered fully optimized once the residual Hellmann-Feynman (HF) forces were less than 5.0×10^{-4} eV/Å. The activation energy for this switching was determined using the nudged elastic band (NEB) method. The polarization values were determined by Berry's phase method implemented in the ABINIT code.

Results

Figure A-1 shows the calculated lattice constants and spontaneous polarization of Al_2O_3 , Ga_2O_3 , In_2O_3 , Fe_2O_3 and Sc_2O_3 . The spontaneous polarization (P_s) was calculated using the Berry phase approach. P_s values of these compounds are more than $20 \mu\text{C}/\text{cm}^2$. In the case of κ - Al_2O_3 -type structure, we need to decide the centrosymmetric structure because the ferroelectric phase transition of κ - Al_2O_3 -type structure have not been reported. In this study, we assumed the centrosymmetric structure with *Pbcn* (Figure A-

2). The activation energy for polarization switching are 0.08~0.15 eV/f.u.(Figure A-3). The value of κ -Al₂O₃ is larger than that of the others. These activation energy are fairly small compared to the previous reported result ($Pna2_1 \rightarrow Pnna \rightarrow Pna2_1$). In our model, the polarization switching is induced by sharing of the close-packed oxygen layers, leading to a recombination of cations from 6(4) to 4(6) coordination. This mechanism illustrate in Figure A-4. Sharing occurs in layer with tetrahedral and octahedral site. During polarization switching, atoms mainly move along a-axis. The coordination of each cation sites are summarized in Figure A-5. The coordination change at site A and B, while site C and D keep 6 coordination. Figure A-6 shows the polarization switching viewing from c-axis. The change of coordination of 6(4) to 4(6) at site A and site B can be seen.

Figures

	Calculation			Error			Ps[C/m ²]
	a[Å]	b[Å]	c[Å]	a[%]	b[%]	c[%]	
Al ₂ O ₃	4.885	8.396	9.026	(0.82%)	(0.75%)	(0.77%)	-0.26
Ga ₂ O ₃	5.116	8.795	9.409				-0.22
In ₂ O ₃	5.678	9.641	10.281				-0.21
Fe ₂ O ₃	5.128	8.859	9.571	(0.81%)	(0.93%)	(1.08%)	-0.20
Sc ₂ O ₃	5.436	9.264	10.031				-0.22

Figure A-1 Calculated lattice constants and spontaneous polarization of Al₂O₃, Ga₂O₃, In₂O₃, Fe₂O₃ and Sc₂O₃

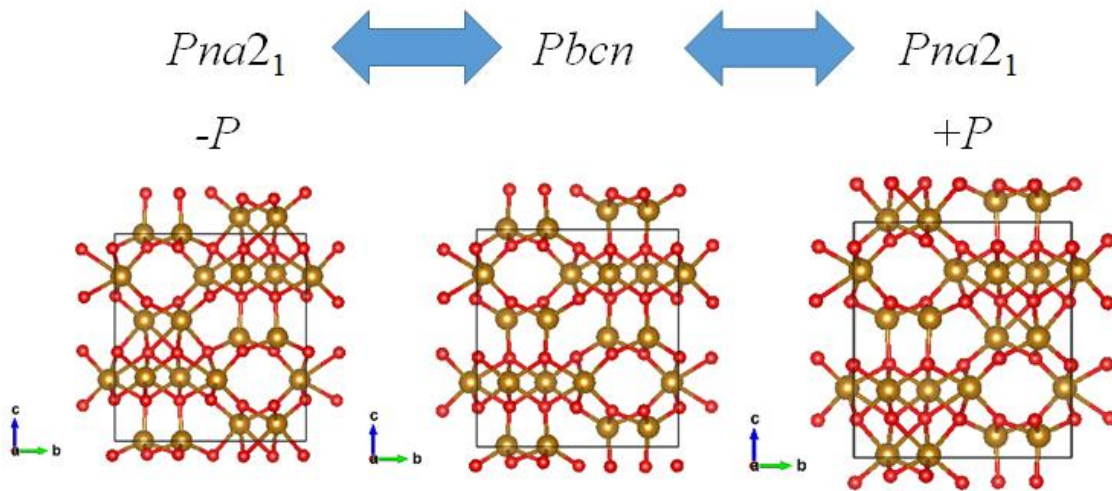


Figure A-2 Polarization switching through centrosymmetric structure of *Pbcn*.

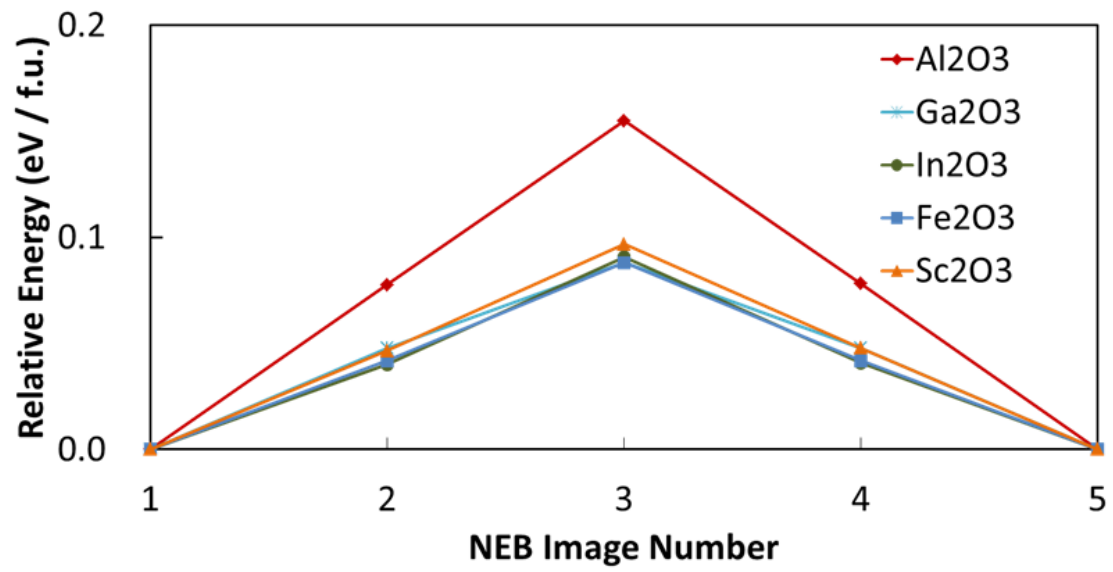


Figure A-3 Relative energy during polarization switching.

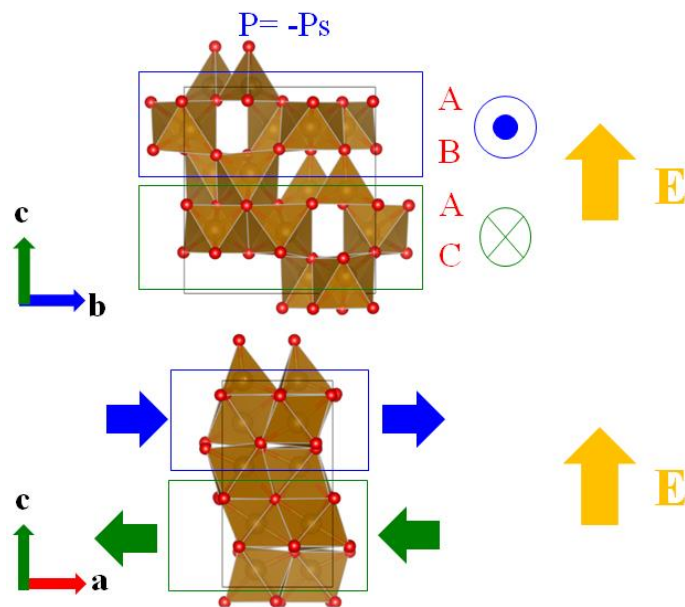
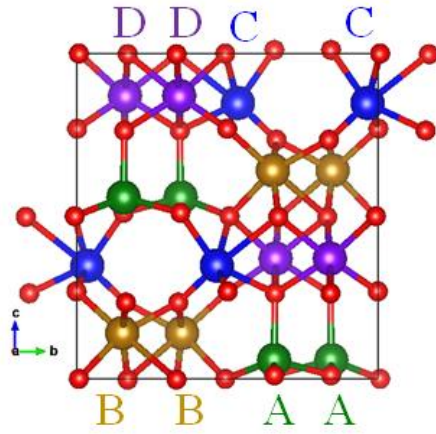


Figure A-4 Schematic illustration of polarization switching



	$Pna2_1$ (+P)		$Pbcn$		$Pna2_1$ (-P)
Site A	4	4	4	5	6
Site B	6	5	4	4	4
Site C	6	6	6	6	6
Site D	6	6	6	6	6

Figure A-4 Coordination change at cation sites during polarization switching.

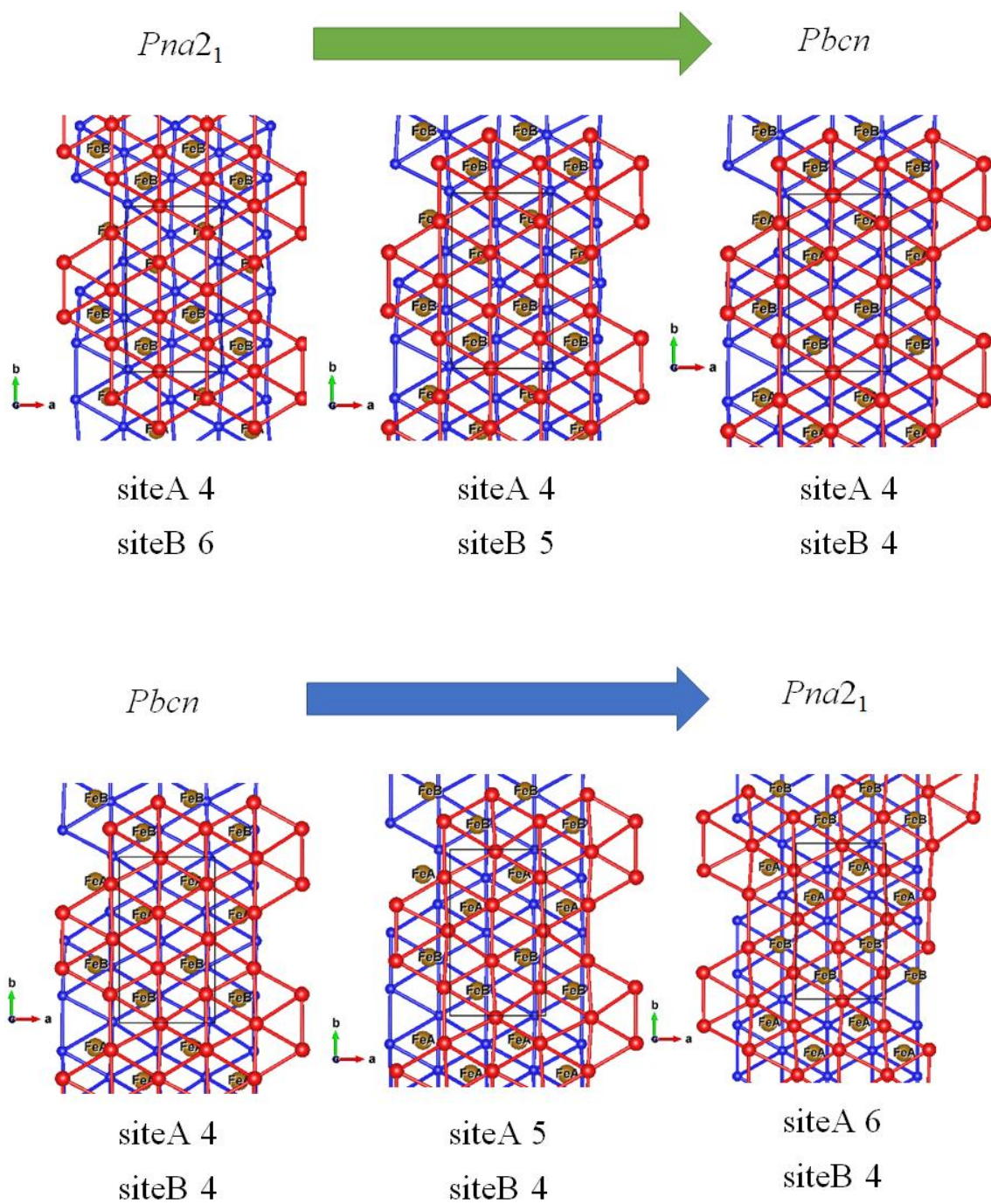


Figure A-6 The polarization switching viewing from c-axis.

Acknowledgement

I would like to express the deepest appreciate to supervisor, Professor Mitsuru Itoh, who gave me an impassioned guidance and invaluable discussion.

I am grateful to Professor Tomoyasu Taniyama for his fruitful suggestions, valuable advices, and helpful discussions.

I would like to express my gratitude to the former Assistant Professor Hiroki Taniguchi and Assistant Professor Shintaro Yasui for helpful advices and stimulating discussions.

I am deeply grateful to Dr. Hiroki Moriwake and Ms. Ayako Konishi (Japan Fine Ceramics Center) for first principles calculations.

I would like to show my greatest appreciation to Dr. Takao Shimizu for valuable advices and discussions.

I would like to thank all my colleagues in Itoh-Taniyama group.

I would like to acknowledge Professor Masaki Azuma, Professor Hiroshi Funakubo, Professor Hidenori Hiramatsu, and Professor Tomofumi Susaki for fruitful discussion about my thesis.

Finally, I would like to express my grateful thanks to my family for their

understanding, support, and encouragement.